From the holdings of the Department of Special Collections , Princeton University Library, Princeton, NJ

These documents are either in the public domain, or can only be used for educational and research purposes (Fair use) as per U.S. Copyright law (text below). By accessing this file, all users agree that their use falls in the public domain or within fair use as defined by the copyrightlaw. We do not charge any permission or usage fees for the publication of images of material inour collections, including those provided by Princeton University Library, via our website, catalog, or directly from staff.For more information regarding copyright, credit, and citation please review the information onthe Copyright, Credit and Citation Guidelines page of our website.
https://library.princeton.edu/special-collections/policies/copyright-credit-and-citation-guidelines. If you have any questions, including how to order higher-quality images from the collection, contact Special Collections Public Services via our Ask Us! Form. https://library.princeton.edu/special-collections/ask-us

Doctoral Dissertations, 2011-2026 Atmospheric and Oceanic Sciences

2015

Understanding the dependence of tropical high cloud amount and radiative flux on sea surface temperatures

Radley, Claire

Princeton, NJ : Princeton University

http://arks.princeton.edu/ark:/88435/dsp01q524jq99x

U.S. Copyright law: The copyright law of the United States (Title 17, §108, United States Code) governs the making of photocopies or other reproductions of copyrighted material. Under certain conditions specified in the law, libraries and archives are authorized to furnish a photocopy or other reproduction. One of these specified conditions is that the photocopy or reproduction is not to be used for any purpose other than private study, scholarship, or research. If a user makes a request for, or later uses, a photocopy or reproduction for purposes in excess of fair use that user may be liable for copyright infringement. This institution reserves the right to refuse to accept a copying order if, in its judgment, fulfillment of the order would involve a violation of copyright law. https://www.copyright.gov/title17/title17.pdf

Understanding the dependence of tropical high cloud amount and radiative flux on sea surface temperatures

Claire E. Radley

A Dissertation
Presented to the Faculty
of Princeton University
in Candidacy for the Degree
of Doctor of Philosophy

Recommended for Acceptance
by the Program in
Atmospheric and Oceanic Sciences
Adviser: Assistant Professor Fueglistaler

January 2015

© Copyright by Claire E. Radley, 2015.

All rights reserved.

Abstract

We use observations and four GFDL AGCMs to analyze the relation between variations in spatial patterns and area-averaged quantities in the top-of-atmosphere radiative fluxes, cloud amount and precipitation related to El Niño over the period 1979-2008. We find that model-to-observation biases in the base state translate into corresponding biases in anomalies in response to El Niño. The pattern and amplitude of model biases in reflected shortwave (SW) and outgoing longwave radiation (OLR) follows expectations based on their biases in cloud amount: models with a positive cloud amount bias, compared to observations, have too strong local responses to El Niño in cloud amount, SW, OLR and precipitation. Tropical average OLR increases in response to El Niño in observations and models (correlation coefficients (r) with Niño 3.4 Index in range 0.4 to 0.6). Weaker correlations are found for SW (r: -0.6 to 0), cloud amount (r: -0.2 to +0.1) and precipitation (r: -0.2 to 0).

Tropical high clouds are closely coupled to deep convection, but local cloud amount and convective mass flux are non-linearly related. We use the GFDL-AM2 model forced with idealized SST perturbations to study the sensitivity of high clouds to the large-scale distribution of convection. Increasing/decreasing the SST contrast between convective and non-convective regions decreases/increases the tropical deep convective area, and warming of convective areas decreases the tropical average convective mass flux ($\langle m_c \rangle$). In all experiments, fractional high cloud amount changes are less than fractional changes in $\langle m_c \rangle$. High cloud amount is half as sensitive as expected from the climatological average cloud amount, as a function of convective mass flux, due to strong compensation from non-convective high clouds. The latter results from changes in relative humidity related to the change in $\langle m_c \rangle$. This effect renders high cloud amount remarkably robust to perturbations, though radiative effects of convective and non-convective clouds will differ.

Finally, we analyze tropospheric temperature trends in 19 atmosphere-only models and show the spread is due, at least in part, to difference in precipitation-weighted SST ($P{\cdot}SST$) trends (r=+0.99). We confirm vertical amplification of surface warming by a factor of 2.4±0.1 at the 300mb level, relative to $P \cdot SST$.

Acknowledgements

It goes without saying that earning a PhD would not have been possible without the support and encouragement of my adviser, committee, friends and family.

Over the years, my adviser Stephan Fueglistaler has provided invaluable direction and insight, and has always pushed me to dig deeper in my analysis. Despite his hectic schedule he always made time to meet with me and I'm grateful to him for keeping me on track. Leo Donner was also critical to my research. Not only does he have an intricate understanding of climate models, but is an amazing teacher and brilliant scientist. The task of running the climate models, however, was not trivial and I'm thankful to Yi Ming for his help. All three scientists have been a tremendous asset in my PhD, continuously pushing me to look at the big picture and implications of my work.

The past five years have not been easy and I'm extremely grateful to my parents for all their support. They have always encouraged me to pursue my dreams and I would not have made it through my PhD without their frequent phone calls and visits. I look forward to living closer to home and spending more time with them, my brother and sister. I also wish to thank my wonderful boyfriend Will, whom I met whilst at Princeton. He has been the best support system anyone could ask for, with never-ending patience, understanding and love. Our dog, Bruno, has been the perfect company for writing this thesis as it's truly impossible to be stressed while in his presence.

I want to thank the entire AOS program, particularly Anna Valerio, who has been a wonderful friend over the years and is an amazing asset to the department. There are many AOS students who have added to my experience here at Princeton, both academically and socially, but I want to give particular thanks to Andrew Ballinger, Amanda O'Rourke, Sam Potter and Joe Majkut. Finally, I want to thank Fulbright

NZ, who made it possible for me to come to the United States and have generously sponsored me over the course of my PhD.

To my parents.

Contents

Abstract iii

Acknowledgements v

List of Tables xi

List of Figures xiii

1 Introduction **1**

1.1 Motivation 1

1.2 Outline of Thesis 10

2 Cloud and radiative balance changes in response to ENSO in observations and models **14**

2.1 Introduction 14

2.2 Data 15

2.3 Results 18

2.3.1 Tropically averaged time series 18

2.3.2 Tropically/globally averaged linear regression 21

2.3.3 Differences between ERBE and CERES observations 24

2.3.4 Base state regional results 30

2.3.5 Regional TOA radiation anomalies 35

2.3.6 Scaling of anomalies with the base state 38

2.4 Summary and Conclusions 42

3 The role of large-scale convective organization for tropical high cloud properties 45

3.1 Introduction . . . 45

3.2 Experimental Setup . . . 46

3.2.1 General Circulation Model . . . 46

3.2.2 SST perturbations . . . 47

3.2.3 Convective mass flux and high cloud amount . . . 49

3.3 Results . . . 52

3.3.1 Convective mass fluxes . . . 54

3.3.2 Convective area and surface temperature gradients . . . 55

3.3.3 High cloud amount . . . 61

3.3.4 Compensation in non-convective regions . . . 62

3.4 Additional Results . . . 65

3.4.1 Precipitation Anomalies . . . 65

3.4.2 Liquid and Ice Water Paths . . . 68

3.4.3 Low Clouds . . . 71

3.4.4 Implications for TOA Radiation Budget . . . 74

3.5 Conclusions . . . 76

4 The importance of convective SSTs on tropospheric temperature 78

4.1 Introduction . . . 78

4.2 Experimental Setup . . . 80

4.2.1 Data . . . 80

4.2.2 Analysis . . . 83

4.3 Trend Results: 1984-2008 . . . 84

4.4 Time series results: 1979-2008 . . . 88

4.5 Conclusions . . . 91

5 Critical Discussion **96**

Bibliography **102**

List of Tables

2.1 Climatological mean of tropical OLR, LWCRF, SW and SWCRF (Wm^{-2}) for the January 1985-December 1989 period. 25

2.2 Climatological mean of tropical OLR, SWCRF, SW and SWCRF (Wm^{-2}) for the January 2001-December 2007 period. 25

2.3 Tropical average cloud base state amount and anomalies (%) during El Niño events for the January 2001-December 2007 period. 33

2.4 Tropical average OLR, LWCRF, SW and SWCRF (Wm^{-2}) anomalies during El Niño events for the January 2001-December 2007 period. . 39

2.5 Climatological mean precipitation (mm/day) for the January 2001-December 2007 period. 42

3.1 Summary of the setup (left) and results (right) of the 8 perturbation experiments. Tropical SST perturbations are shown for the 4 regions: precipitation, P > 8 mm/day, $8 \geq P > 6$ mm/day, $6 \geq P >$ 4mm/day and 4 mm/day $\geq P$. Also shown are the tropical mean anomalies in surface temperature T_s (K), convective area A_c(%), convective mass flux m_c (%), and the 4 decomposition terms of the high cloud amount anomalies: $f'_{uni} \cdot C$ (%), $f' \cdot C$ (%), $f \cdot C'$ (%) and $f' \cdot C'$ (%). See text for further details. 50

4.1 Trends in T_S, SST, P·SST and 300hPa T_a calculated over the period 1984-2008, in units of K/decade, for the individual ensemble members of 19 AMIP models. 92

4.2 Trends in T_S, SST, P·SST and 300hPa T_a calculated over the period 1984-2008, in units of K/decade, for the ensemble means of 13 AMIP models. The numbering of the models is consistent with that introduced in table 4.1. 93

4.3 Correlation of the difference in atmospheric temperature with the difference in SST between 2 models. Differences are calculated from ensemble mean time series, and the mean correlation coefficient across all ensembles is +0.19. 94

4.4 Correlation of the difference in atmospheric temperature with the difference in $P \cdot SST$ between 2 models. Differences are calculated from ensemble mean time series, and the mean correlation coefficient across all ensembles is +0.68. 95

List of Figures

1.1 The global annual mean energy budget of Earth for the approximate period 2000-2010. All fluxes are in W/m^2. Solar fluxes are in yellow and infrared fluxes in pink. The four flux quantities in purple shaded boxes represent the principal components of the atmospheric energy balance. Taken from Stephens et al. (2012). 2

1.2 Diverse cloud regimes reflect diverse meteorology. **(a)** A visible-wavelength geostationary satellite image shows (from top to bottom) expanses and long arcs of cloud associated with extratropical cyclones, subtropical coastal stratocumulus near Baja California breaking up into shallow cumulus clouds in the central Pacific and mesoscale convective systems outlining the Pacific Intertropical Convergence Zone (ITCZ). **(b)** A schematic section along the dashed line from the orange star to the orange circle in (a), through a typical warm front of an extratropical cyclone. It shows (from right to left) multiple layers of upper-tropospheric ice (cirrus) and mid-tropospheric water (altostratus) cloud in the upper-tropospheric outflow from the frontal zone, an extensive region of nimbostratus associated with frontal uplift and turbulence-driven boundary layer cloud in the warm sector. **(c)** A schematic section along the dashed line from the red star to the red circle in (a). It shows (from right to left) typical low-latitude cloud mixtures, shallow stratocumulus trapped under a strong subsidence inversion above the cool waters of the oceanic upwelling zone near the coast and shallow cumulus over warmer waters further offshore transitioning to precipitating cumulonimbus cloud systems with extensive cirrus anvils associated with rising air motions in the ITCZ. Taken from Boucher et al. (2013). 4

1.3 Cloud feedback parameters as predicted by GCMs for responses to CO_2 increases including rapid adjustments. Total feedback shown at left, with centre light-shaded section showing components attributable to clouds in specific height ranges, and right dark-shaded panel those attributable to specific cloud property changes where available. The net feedback parameters are broken down in their longwave (LW) and shortwave (SW) components. Type attribution reported for CMIP3 does not conform exactly to the definition used in the Cloud Feedback Model Intercomparison Project (CFMIP) but is shown for comparison, with their 'mixed' category assigned to middle cloud. Taken from Boucher et al. (2013). 7

1.4 Climatological mean high cloud amount (%) in GFDL AM2 for the period 1979-2008. 8

1.5 Mean high cloud amount distribution in historical run (black line) and with sea surface temperatures increased by 0.5K (red line). 9

1.6 Mean change in GFDL AM2 high cloud amount (%) when sea surface temperatures are increased by 0.5K. Tropical mean change in high cloud amount is +0.2%. 9

1.7 PDF of high cloud amount (%) changes in GFDL AM2, when sea surface temperatures are increased by 0.5K. 10

2.1 Idealized schematic showing atmospheric and oceanic conditions of the tropical Pacific region and their interactions during normal conditions and El Niño conditions. a) Mean climate conditions in the tropic Pacific, indicating SSTs, surface wind stress and associated Walker circulation, and the mean position of convection. b) Typical conditions during an El Niño event. SSTs are anomalously warm in the east; convection moves into the central Pacific; the trade winds weaken in the east and the Walker circulation is disrupted. Figure taken from Collins et al. (2010). 16

2.2 The seasonal cycle for tropically averaged a) OLR (Wm^{-2}), b) SW (Wm^{-2}) and c) Total Cloud Amount (%), is shown for observations and models. Values are calculated over the full length of each dataset. 19

2.3 The time series of tropically averaged anomalies are shown for a) OLR (Wm^{-2}), b) SW (Wm^{-2}) and c) Total Cloud Amount (%). The Niño 3.4 index (°C) is shown in d). Periods affected by volcanic eruptions are shaded in grey, and El Niño periods are shaded in red. 20

2.4 Correlation coefficient for a) tropically and b) globally averaged OLR and SW when linearly regressed against the Niño 3.4 index. The larger markers indicate significance at the 95% level. 23

2.5 a) Mean CERES OLR minus mean ERBE OLR (with $4.5Wm^{-2}$ offset removed), b) Mean CERES SW minus mean ERBE SW (with -1.5 Wm^{-2} offset removed). Also shown is the difference in ISCCP mean c) Total and d) high cloud amount (%) for the CERES minus ERBE period. Only full year periods are used. 28

2.6 Composite of CERES a) OLR and b) SW anomalies (Wm^{-2}) during three El Niño events from 2001-2007. Anomalies are defined as the difference from the CERES EBAF 2001-2007 climatological mean. . 29

2.7 Climatological mean OLR (Wm^{-2}) in models minus CERES observations for a) AM3, b) AM2, c) HiRAM - c180 and d) HiRAM - c360. . 31
2.8 Climatological mean SW (Wm^{-2}) in models minus CERES observations for a) AM3, b) AM2, c) HiRAM - c180 and d) HiRAM - c360. . 32
2.9 Climatological mean of high cloud amount (%) for ISCCP and AM3 with ISCCP simulator. The values are meridionally averaged from 30 °S-30 °N and plotted as a function of longitude for 3 different optical depth categories - thin, medium and thick. Dashed lines are total high cloud amounts from AM3, AM2, HiRAM-c180 and HiRAM - c360. . 34
2.10 Same as figure 2.9 but for mid-level clouds. 35
2.11 Same as figure 2.9 but for low-level clouds. 36
2.12 Probability distribution for a) OLR and b) SW anomalies (Wm^{-2}) for CERES, AM2, AM3, HiRAM c180 and c360 during 2001-2007 El Niño events. 38
2.13 PDF of a) raw and b) scaled high cloud anomaly (%) during 2001-2007 El Niño events for ISCCP, AM3 with and without simulator, AM2, HiRAM - c180, and HiRAM - c360. Scaling factors are taken from the biases in base state high cloud amounts in table 2.3. 40

3.1 Climatological mean surface temperature changes (K) for experiments a) A, b) B, c) C, and d) D, as outlined in table 3.1. Positive values indicate an increase in temperature from the control run. 47
3.2 Same as figure 3.1 but for experiments a) E, b) F, c) G and d) U. . . 48
3.3 (a) Joint distribution density and mean, C(m_c) (solid red line), of the high cloud amount for the control calculation, as a function of 500hPa convective mass flux m_c, b) convective mass flux distribution f(m_c) for the control calculation. See text for further details. 51

3.4 Total high cloud amount anomaly (black) for experiments a) A, b) B, c) C and d) D, integrated as m_c decreases such that the y-intercept gives the tropical mean high cloud anomaly. Also shown is $f'_{uni} \cdot C$ (green), which indicates the predicted high cloud anomaly that would result from a spatially uniform change in m_c, and the decomposition of the three contributors to high cloud amount anomaly: $f' \cdot C$ (blue dashed), $f \cdot C'$ (red dashed) and $f' \cdot C'$ (purple dashed). See text for further details. 53

3.5 Same as figure 3.4 but for experiments a) E, b) F, c) G, and d) U. . . 54

3.6 High cloud amount changes for each perturbation experiment as function of change in (a) tropical average surface temperature, (b) convective area fraction, and (c) tropical average convective mass flux. (d) $f' \cdot C$ against the model average high cloud change. (e) $f' \cdot C$ against the expectation for a uniform fractional change in convective mass flux. (f) The change in the relation between convective mass flux and cloud amount, $f \cdot C'$, against $f' \cdot C$. Colors in (d,e,f) as for terms in figure 3.4 and 3.5. Correlation coefficients, r, and linear regression slopes, b, are given for quantitative arguments. 55

3.7 Convective area change (%) for each perturbation experiment as a function of change in a) tropical average T_s anomaly (K) (correlation coefficient r=-0.61) and b) zonal T_s gradient anomaly (K) (r=-0.99). . 56

3.8 Experiment A changes for a) surface temperature (K), b) evaporation ($kg/m^2/s$), c) specific humidity (kg/kg) and d) moist static entropy at 900mb ($J/kg/K$). Solid black contour line indicates where the temperature difference between experiment A and the control run is zero. 57

3.9 Experiment A changes for a) convergence at 900mb (s^{-1}) b) $-1\times$Omega at 500mb (pa/s), c) convective mass flux ($kg/m^2/s$). Solid black contour line indicates where the temperature difference between experiment A and the control run is zero. 58

3.10 PDF of experiment A changes within the convective region (i.e. where precipitation exceeds 6mm/day), for a) surface temperature (K) b) evaporation ($kg/m^2/s$), c) specific humidity (kg/kg), d) moist static entropy at 900mb ($J/kg/K$), e) convective mass flux at 500mb ($kg/m^2/s$), and f) $-1\times$Omega (pa/s). Also shown is the probability of the anomaly to be positive (i.e. the fractional area that has a positive anomaly). 59

3.11 Control run values for a) m_c ($kg/m^2/s$), b) omega (hPa/s), c) cloud fraction, d) temperature (K), e) specific humidity (kg/kg), and f) relative humidity (%) averaged over the region ($255-290^\circ E$, $20-30^\circ S$). 63

3.12 Experiment A changes for a) m_c, b) omega, c) cloud fraction, d) temperature, e) specific humidity, and f) relative humidity averaged over the region ($255-290^\circ E$, $20-30^\circ S$). Changes are given as a percentage change in the base state values (see figure 3.11). 64

3.13 Same as figure 3.12 but for experiment G. 65

3.14 Total precipitation changes (%) for each perturbation experiment as a function of change in (a) tropical average surface temperature (correlation coefficient, r=+0.95), (b) convective area fraction (r=-0.42) and (c) tropical average convective mass flux (r=-0.56). 66

3.15 Convective precipitation changes (%) for each perturbation experiment as a function of change in (a) tropical average surface temperature (correlation coefficient, r=-0.28), (b) convective area fraction (r=+0.90) and (c) tropical average convective mass flux (r=+0.86). 66

3.16 Stratiform precipitation changes (%) for each perturbation experiment as a function of change in (a) tropical average surface temperature (correlation coefficient, r=+0.61), (b) convective area fraction (r=-0.95) and (c) tropical average convective mass flux (r=-0.97). 67

3.17 Changes in the percent of total rainfall that is defined as 'convective', as a function of change in a) tropical average surface temperature (correlation coefficient, r=-0.69), (b) convective area fraction (r=+0.99) and (c) tropical average convective mass flux (r=+1.00). Positive values indicate an increase in the percent of rainfall that is convective, relative to the base state percentage of 82%. 67

3.18 Joint distribution density for a) IWP (g/m^2) and b) LWP (g/m^2) against m_c (kg/m^2/s). 69

3.19 Ice water path changes (g/m^2) for each perturbation experiment as a function of change in (a) tropical average surface temperature (correlation coefficient, r=+0.69), (b) convective area fraction (r=-0.97) and (c) tropical average convective mass flux (r=-0.99). 70

3.20 Liquid water path changes (g/m^2) for each perturbation experiment as a function of change in (a) tropical average surface temperature (correlation coefficient, r=+0.71), (b) convective area fraction (r=-0.96) and (c) tropical average convective mass flux (r=-0.99). 70

3.21 Low cloud amount changes (g/m^2) for each perturbation experiment as a function of change in (a) tropical average surface temperature (correlation coefficient, r=+0.49), (b) convective area fraction (r=-0.97) and (c) tropical average convective mass flux (r=-0.96). 71

3.22 Vertical temperature profile changes (K) for each perturbation experiment. 72

3.23 Vertical equivalent potential temperature profile changes (K) for each perturbation experiment. 72
3.24 Joint distribution density of low cloud amount (%) against the difference in equivalent potential temperature between 700mb and 925mb (K). 73
3.25 Low cloud amount change (%) as a function of the change in the difference in equivalent potential temperature between 700mb and 925mb (K). 74
3.26 Experiment A changes for a) OLR (W/m^2) and b) reflected SW (W/m^2). Positive values indicate an increase relative to the control run. 75
3.27 OLR changes (W/m^2) for each perturbation experiment as a function of change in (a) tropical average surface temperature (correlation coefficient, r=+0.77), (b) convective area fraction (r=-0.96) and (c) tropical average convective mass flux (r=-0.99). 75
3.28 Absorbed SW changes (W/m^2) for each perturbation experiment as a function of change in (a) tropical average surface temperature (correlation coefficient, r=-0.64, (b) convective area fraction (r=+0.99) and (c) tropical average convective mass flux (r=+0.99). 76
3.29 Net radiation changes (W/m^2) for each perturbation experiment as a function of change in (a) tropical average surface temperature (correlation coefficient, r=-0.70), (b) convective area fraction (r=+0.98) and (c) tropical average convective mass flux (r=+1.00). 76

4.1 300mb tropospheric temperature changes as a function of changes in a) sea surface temperature (K) and b) precipitation-weighted sea surface temperature (K), for the eight perturbation experiments detailed in Chapter 3. 80

4.2 GFDL HiRAM-c180 minus a) HadISST and b) Hurrell monthly mean surface temperature (K) for January 1990. 81

4.3 GFDL HiRAM-c180 minus interpolated a) HadISST and b) Hurrell monthly mean surface temperature (K) for January 1990. The interpolated fields are calculated using equation 4.1. 83

4.4 Scatter plot of 300mb atmospheric temperature (T_a) trend against a) SST trend and b) P·SST trend. All trends are calculated over the period 1984-2008 and have units of K/decade. Black markers indicate values from individual ensemble members, whilst red markers indicate the ensemble means. The correlation coefficients (r) are given for both individual ensemble members (black text) and ensemble means (red text). 85

4.5 Scatter plot of scaling factors, $F_S = T_a/SST$ and $F_P = T_a/(P \cdot SST)$, for the individual ensemble members of 19 AMIP models. Ensemble means are indicated by bold symbols and the dashed line represents the 1:1 relationship. 86

4.6 Scaling factors, $F_S = T_a/SST$ and $F_P = T_a/(P \cdot SST)$, and linear regression slopes, m(SST) and m($P \cdot SST$), for the 19 AMIP models. Ensemble means are indicated by bold symbols. 87

4.7 Decomposition of T_a trend into $F_P^{j\prime} \cdot \overline{P \cdot SST}$ (K/dec) and $\overline{F_P} \cdot (P \cdot SST)'$ (K/dec) for 13 ensemble means. See text for further details. 88

4.8 Plot of SST and $P \cdot SST$ scaling factors as a function of their corresponding linear regression slope. Ensemble means are indicated by bold markers, and the dashed line indicates the 1:1 relationship between scaling factor and slope. 89

4.9 Correlation coefficient of the 1979-2008 T_a time series with SST and $P \cdot SST$. Ensemble means are indicated by bold markers. 90

Chapter 1

Introduction

1.1 Motivation

Earth's atmosphere is primarily composed of gases, such as water vapor and carbon dioxide, but it also consists of liquid and solid matter in the form of particles. Despite their small mass, particles have a large impact on radiative transfer within the atmosphere, which in turns impacts both climate and weather. Clouds, which are composed of either liquid water or ice particles, are a large modulator of the Earth's radiative energy budget. Specifically, clouds affect the top-of-atmosphere (TOA) budget in two ways: (1) By reflecting incoming solar or shortwave (SW) radiation, and (2) by trapping outgoing long wave (LW) radiation emitted from either the Earth's surface or atmosphere. These two mechanisms have opposing affects on the climate system, as reflecting SW radiation cools the planet and trapping LW radiation warms. Whilst the first satellite observations of the Earth's TOA radiative energy budget took place in the 1960's, it wasn't until the Earth Radiation Budget Experiment (ERBE) measurements in the 1980's that the radiative effects of clouds were able to be reasonably accurately quantified. These measurements have since been confirmed by the Clouds and the Earth's Radiant Energy System (CERES). The results of these

satellite measurements tell us that the albedo effect of clouds enhances the reflected SW radiation by $47.5 \pm 3W/m^2$, and reduces the outgoing LW flux relative to clear skies by $26.4 \pm 4W/m^2$ (as shown in figure 1.1). This gives a net loss of radiation from Earth by clouds of $21.1 \pm 5W/m^2$ (Stephens et al., 2012).

The magnitude of the positive LW cloud radiative forcing (LWCRF) is determine by the temperature difference between the surface and cloud top, with a larger difference resulting in a larger LWCRF. (NB: LWCRF is defined as the all-sky minus clear sky outgoing LW flux). The magnitude of the negative SW cloud radiative forcing (SWCRF), however, is simply a measure of how reflective a cloud appears from space, which depends on water path, size and shape of particles. For any given cloud, the total cloud radiative forcing (CRF) is the sum of both LWCRF and SWCRF, which typically results in large negative values for low clouds and near zero values for high clouds. This arises because low clouds are bright, and therefore have a large SWCRF, but have very little LWCRF due to their low altitude. High clouds on the other hand have a large positive LWCRF that balances the negative SWCRF (Kiehl, 1994).

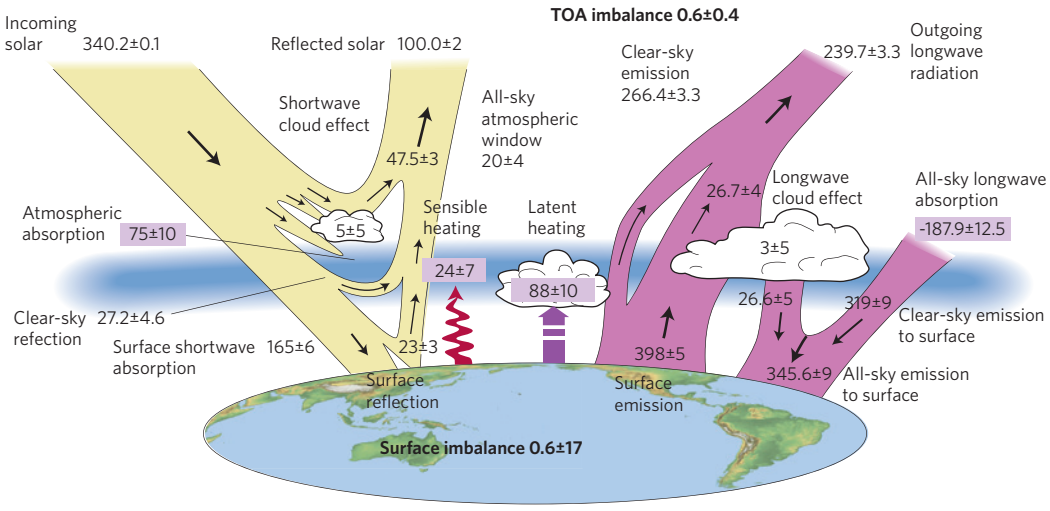


Figure 1.1: The global annual mean energy budget of Earth for the approximate period 2000-2010. All fluxes are in W/m^2. Solar fluxes are in yellow and infrared fluxes in pink. The four flux quantities in purple shaded boxes represent the principal components of the atmospheric energy balance. Taken from Stephens et al. (2012).

Clouds cover roughly two thirds of the globe and are formed when an air parcel either cools or the specific humidity increases enough such that it is sufficiently supersaturated, and either the condensation or freezing nuclei are activated. Clouds can be divided into various types or regimes, which are primarily determined by larger-scale circulations. Cumulonimbus clouds, for example, which are primarily found in the tropical regions, occur where there is upward tropospheric air motion. Shallow stratocumulus, on the other hand, is found in regions below strong subsidence such as over the cool waters off the Californian coast (see figure 1.2). As summarized in figure 1.2, mid-latitude cloud formation differs to that of the tropics, however the focus of this thesis is tropical processes so we will not discuss this further. In order to distinguish between various cloud types, we categorize clouds into three categories as defined by ISCCP (Rossow and Schiffer, 1991): high-, mid-, and low-level clouds. High-level clouds are above 440hPa, mid-level are between 440-680hPa, and low-level clouds are below 680hPa.

In the tropics, the large-scale circulation is a superposition of the upward convective mass flux and the radiatively driven subsidence (Held and Soden, 2006). Convective mass flux is largest in regions of high sea surface temperature (SST), such as the western equatorial Pacific, and drives the production of convective precipitation and high cloud amount through the condensation of water vapor. This process also warms the troposphere via latent heat release, and provides a mechanism for surface temperatures to affect atmospheric temperatures. Given that the free tropospheric temperature is dynamically constrained to be nearly zonally uniform in the tropics (Bretherton and Sobel, 2002), and that the surface is only weakly able to communicate with the free-troposphere in non-convective regions, the tropical mean tropospheric temperature must be determined by the convective regions (Sobel et al., 2002). Any future changes in tropical convection, which may arise from climate change, will therefore affect the cloud, precipitation and tropospheric temperature fields.

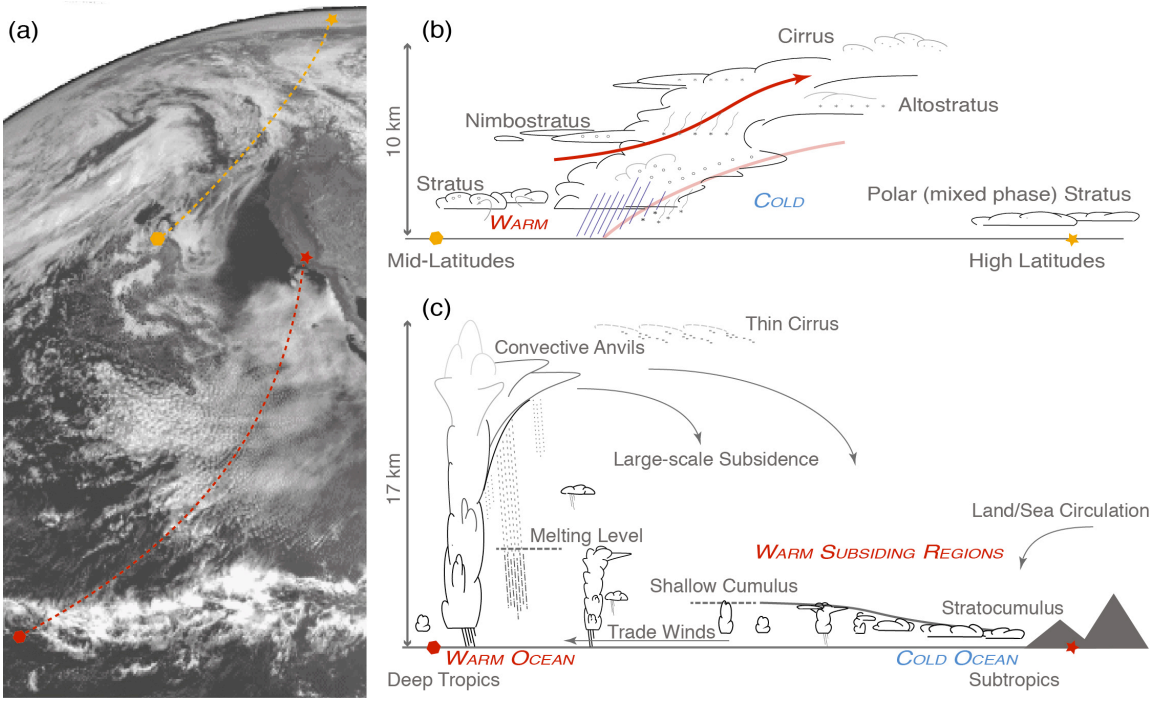


Figure 1.2: Diverse cloud regimes reflect diverse meteorology. **(a)** A visible-wavelength geostationary satellite image shows (from top to bottom) expanses and long arcs of cloud associated with extratropical cyclones, subtropical coastal stratocumulus near Baja California breaking up into shallow cumulus clouds in the central Pacific and mesoscale convective systems outlining the Pacific Intertropical Convergence Zone (ITCZ). **(b)** A schematic section along the dashed line from the orange star to the orange circle in (a), through a typical warm front of an extratropical cyclone. It shows (from right to left) multiple layers of upper-tropospheric ice (cirrus) and mid-tropospheric water (altostratus) cloud in the upper-tropospheric outflow from the frontal zone, an extensive region of nimbostratus associated with frontal uplift and turbulence-driven boundary layer cloud in the warm sector. **(c)** A schematic section along the dashed line from the red star to the red circle in (a). It shows (from right to left) typical low-latitude cloud mixtures, shallow stratocumulus trapped under a strong subsidence inversion above the cool waters of the oceanic upwelling zone near the coast and shallow cumulus over warmer waters further offshore transitioning to precipitating cumulonimbus cloud systems with extensive cirrus anvils associated with rising air motions in the ITCZ. Taken from Boucher et al. (2013).

In a warming climate, the water vapor mixing ratio near the surface has been shown to increase at roughly 7%/K. The hydrological cycle, however, only increases at 2%/K (Held and Soden, 2006) as evaporation, and consequentially precipitation, are energetically constrained at the surface. As shown in figure 1.1, the available latent heating is $88 \pm 10 W/m^2$, which will only increase slightly ($\sim 1 W/m^2$) if CO_2 con-

centrations doubled, thus limiting the rate of increase in evaporation/precipitation. Held and Soden (2006) consider a parcel of air rising from the surface to the free troposphere, with a sufficiently large boundary layer mixing ratio that it then condenses and precipitates. They simplify this process to P=Mq, where P is the precipitation, M is the mass exchanged per unit time, and q is a typical boundary layer mixing ratio. Since q scales with Clausius-Clapeyron but P increases more slowly, M must decrease rapidly (though less rapidly than the Clausius-Clapeyron rate). Therefore, as the surface warms, the atmosphere must exhibit a decrease in convective mass flux.

This reduced upward convective mass flux implies a reduction in the compensating radiatively induced subsidence in the tropics. An alternative argument is made by Knutson and Manabe (1995), who consider that in regions with no deep convection, the radiative cooling Q balances the adiabatic warming associated with the subsidence: $Q = \omega \partial\theta/\partial p$, where θ is the potential temperature and ω is the vertical pressure (p) velocity. The dry stability in the tropics increases as the temperature and the low-level moisture increase, following Clausius-Clapeyron scaling. Since the $Q \approx P$ the radiative cooling of the troposphere does not increase as rapidly as the increase in stability and the subsidence weakens.

It is important to note that a reduction in the mass exchange in the tropics does not necessarily mean there is a proportional reduction in the strength of the mean tropical circulation. In an idealized horizontally homogeneous radiative-convective equilibrium model, the above argument still holds and one would expect a decrease in the convective mass flux as temperatures increased. If one thinks of the mean circulation as the superposition of the upward convective mass flux and the radiatively driven subsidence, a simple redistribution of the former can change the strength of the circulation independently of the subsidence.

Given the close relationship between (1) surface temperature and convective mass flux, and (2) convective mass flux and high cloud amount, one would expect changes

in surface temperature to affect high cloud amount. A perturbation in cloud properties (i.e. cloud feedback) will in turn affect the radiative energy budget, by changing the magnitude of either the reflected SW radiation or the trapped LW radiation. Cloud feedbacks, however, have long been the largest source of uncertainty in climate change predictions (Bony et al., 2006). This is due in part to the fact that cloud formation processes span in scale from the micrometer, for cloud microphysics, to thousands of kilometers. It is not possible to resolve all the necessary processes on todays computers, therefore GCM's must use various parameterizations. These include the parameterization of turbulence, cumulus convection, microphysical processes, radiative transfer and the resulting cloud amount.

Given the large number of parameterizations it is difficult to be certain of a models ability to predict future climate without substantial validation. Ideally, one would validate a model against long term observational records (> 100 years), however we only have 2-3 decades of reliable observations and they are dominated by internal variability. Satellite observations, which give us full global coverage, have the additional problem of calibration, which further complicates our ability to accurately evaluate the models capabilities.

A summary of cloud feedback parameters, as predicted by GCMs for responses to CO_2 are shown in figure 1.3. It is clear that whilst models agree the feedback is positive, there is a large spread in magnitude of 0.2-1.4 $W/m^2/C$. Despite the validation issues there are some robust cloud feedback features that appear consistent across multiple GCMs (Boucher et al., 2013). These are:

1. High clouds rise in altitude and therefore exert a stronger greenhouse effect, which gives a positive feedback of roughly $0.5W/m^2/K$ (Zelinka and Hartmann, 2010). This is due in large part by the tendency for tropical high clouds to rise in such a way as to remain at nearly constant temperature as the climate warms (Hartmann and Larson, 2002).

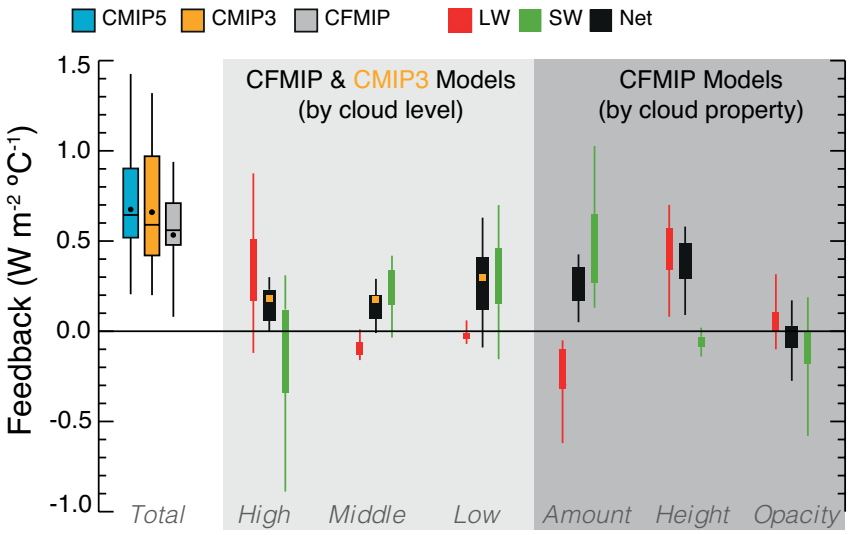


Figure 1.3: Cloud feedback parameters as predicted by GCMs for responses to CO_2 increases including rapid adjustments. Total feedback shown at left, with centre light-shaded section showing components attributable to clouds in specific height ranges, and right dark-shaded panel those attributable to specific cloud property changes where available. The net feedback parameters are broken down in their longwave (LW) and shortwave (SW) components. Type attribution reported for CMIP3 does not conform exactly to the definition used in the Cloud Feedback Model Intercomparison Project (CFMIP) but is shown for comparison, with their 'mixed' category assigned to middle cloud. Taken from Boucher et al. (2013).

2. Mid- and high-level cloud cover tends to decrease in a warmer climate giving a feedback of roughly $0.2W/m^2/K$, but this has yet to be confirmed observationally (Trenberth and Fasullo, 2009; Zelinka and Hartmann, 2010). This loss of cloud amount adds a positive SW and negative LW feedback to the model average, which causes the average net positive feedback to appear to come from the SW part of the spectrum.

3. Observations and most models suggest storm tracks shift poleward in a warmer climate, which causes further positive feedback via a shift of cloud cover to latitudes that receive less sunshine (Bender et al., 2012; Sherwood et al., 2010; Wetherald and Manabe, 1980)

It is worth noting that low cloud feedbacks are responsible for much of the inter-model spread in total cloud feedback (Boucher et al., 2013). Whilst most GCMs do predict that low cloud amount decreases, with low cloud feedback values of -0.09 to $+0.63 W/m^2/K$, there is currently no well-accepted theoretical basis for this feedback.

Whilst much attention has been paid to low clouds and the altitude of high clouds, relatively little attention has been paid to high cloud *amount*. In this thesis we study the factors that control tropical high cloud amount and its relation to SSTs and deep convection.

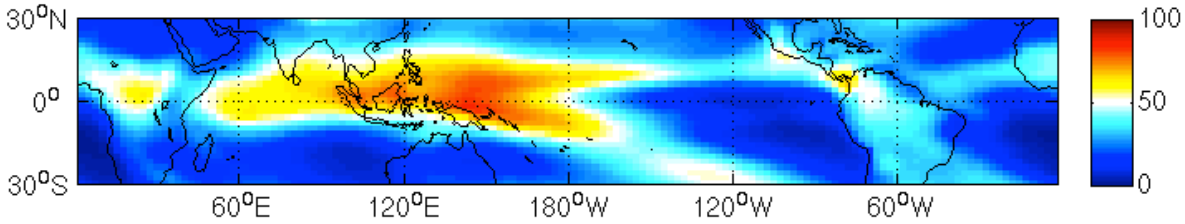


Figure 1.4: Climatological mean high cloud amount (%) in GFDL AM2 for the period 1979-2008.

The climatological mean high cloud amount is shown in figure 1.4. This field was calculated by the GFDL AM2 model, which was run from 1979-2008 with historical SSTs. As expected, high cloud amount is non-uniform across the tropics. There is substantially more high cloud amount in regions of warm SSTs (e.g. Western Pacific), which are associated with upward tropospheric air motion, than in the regions of cooler SSTs and subsidence (e.g. Eastern Pacific). Due to this non-uniformity, we find it useful to plot the high cloud amount *distribution*. The solid black line in figure 1.5 represents the historical high cloud amount distribution shown in figure 1.4. The red line represents the distribution when a perturbation is applied to the SST input and is discussed further later.

A perturbation about this historical base state can be studied by considering an increase in SSTs of +0.5K. Whilst the increase in SSTs is applied uniformly across the tropics, the high cloud amount response is extremely non-uniform. As shown in figure

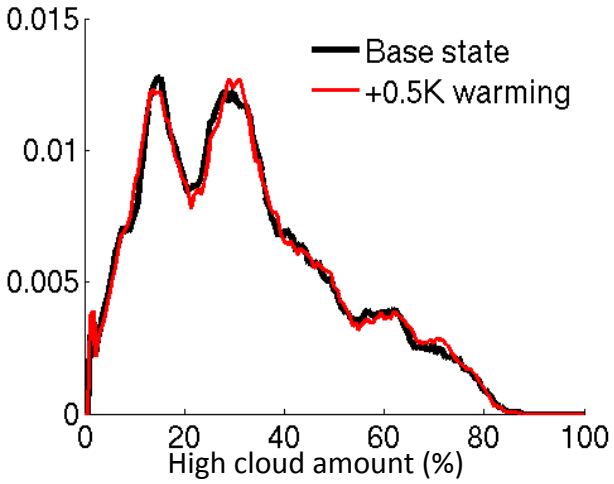


Figure 1.5: Mean high cloud amount distribution in historical run (black line) and with sea surface temperatures increased by 0.5K (red line).

1.6, there are regions of both positive and negative high cloud amount changes. In the 30-year time mean (i.e. 1979-2008) the regional anomalies are up to 10% (see PDF of high cloud changes in figure 1.7), however monthly anomalies can be significantly larger.

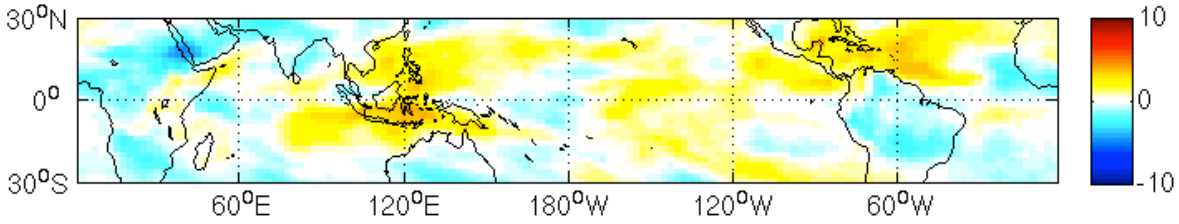


Figure 1.6: Mean change in GFDL AM2 high cloud amount (%) when sea surface temperatures are increased by 0.5K. Tropical mean change in high cloud amount is +0.2%.

Given such large regional changes, one might expect a change in the distribution of high cloud amount. Figure 1.5, however, shows that when an increase in SSTs of 0.5K is applied, the high cloud amount distribution is essentially unchanged. Furthermore, the tropical mean change in high cloud amount is only +0.2%, which indicates there is a large amount of compensation/cancellation occurring between the positive and negative anomalies.

Whilst this experiment is only one example of how Earth's climate might be perturbed, it raises several interesting questions that will be addressed in this thesis. For example, why is the high cloud amount PDF insensitive to perturbations in SST? And, why do local high cloud amount anomalies largely cancel in the tropical mean? Is this always the case when we perturb the system, and do we see this at all in nature? In the following section we outline our approach to this problem and the tools of analysis we employed.

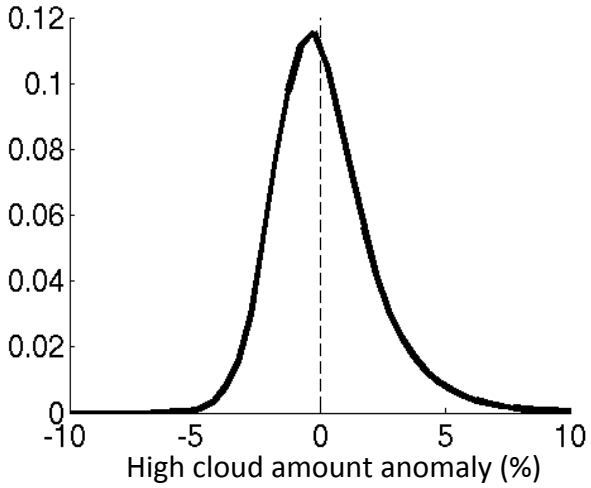


Figure 1.7: PDF of high cloud amount (%) changes in GFDL AM2, when sea surface temperatures are increased by 0.5K.

1.2 Outline of Thesis

As introduced above, the primary objective of this thesis is to understand the dependence of tropical (30 °S-30 °N) high cloud amount, radiative flux, precipitation, and tropospheric temperature on both sea surface temperatures (SSTs) and convective mass flux. This study is approached in three ways:

1. Use of observations and four GFDL atmosphere-only models to analyze the relation between SSTs, cloud amount, TOA radiative fluxes, and precipitation

during El Niño Southern Oscillation (ENSO) events over the period 1979-2008. The short time scale and large amplitude of ENSO makes it an ideal natural forcing to focus on as we have observations of multiple events, which can be used to compare the observations and models with greater certainty than given by trend analysis over the observational period. This analysis is provided in Chapter 2 and is an expansion of Radley et al. (2014).

2. Use of a single GFDL atmosphere-only model (AM2), forced with idealized SSTs, to study the sensitivity of high clouds, TOA radiative fluxes and precipitation to the large-scale convective organization. Eight SST perturbation experiments are performed, with each being run for 30 years, and the analysis is provided in Chapter 3. This chapter is an expansion of the work detailed in Radley and Fueglistaler (2014).

3. Use of 19 atmosphere-only models to analyze the relationship between free-tropospheric temperature and SSTs, particularly in convective regions where the surface is able to communicate with the troposphere via convective adjustment. This chapter builds upon the work of Flannaghan et al. (2014), and uses models from the Couple Model Intercomparison Project (CMIP5), as whilst all models are forced with historically observed SSTs, there is a large degree of spread in tropospheric temperature trends. The results are presented in Chapter 4.

Sea surface temperatures and convective distributions are emerging properties of the coupled ocean-atmosphere system, however atmosphere-only models have prescribed SSTS and are therefore not required to be energetically balanced. Whilst this is unphysical, it provides a valuable tool for understanding atmospheric processes, as the prescribed forcing from SSTs allows us to compare model output with observations for a specific ENSO event. The use of atmosphere-only models is also critical if we want to perturb the system in a way the doesn't currently occur in nature.

The analysis is Chapter 2 uses a combination of tropical mean values, regional maps and probability distribution functions (PDFs) to compare the models against observations. Whilst the focus is ultimately on how high clouds, radiation and precipitation change during an ENSO event, we also include an analysis on the climatological mean state of the variables. Regional maps and PDF's are used as information is often lost when the tropical mean is taken. For example, regions of anomalously high albedo can cancel regions of anomalously small albedo. If one was to look at the tropical mean value it might well agree with the observations, however the spatial distribution could be incorrect, which would have implications for both regional climate and the large-scale circulation. The underlying information in regional maps and PDF's are essentially the same, though PDF's are easier to compare quantitatively as multiple distributions can be plotted on the same figure.

Chapter 3 makes use of both standard and joint PDFs, which are particularly beneficial when analyzing a non-linear relationship between two variables (e.g. climatological mean high cloud amount and convective mass flux). Our analysis of high cloud anomalies also involves a decomposition into the three contributing terms, which provides a great deal of insight into the various physical mechanisms driving the cloud changes.

Our analysis method in Chapter 4 consists primarily of ordinary least squares regression, as we are interested in tropospheric temperature and SST trends over the period 1984-2008. This period was chosen so as to avoid noted problems in observed SST data before 1984 (Flannaghan et al., 2014). Attention is also paid to the interannual variability in the 30 year timeseries from 1979-2008, whereby the timeseries of annual tropospheric temperature is linearly regressed against the timeseries of annual sea surface temperatures.

Chapter 5 concludes the thesis with a summary of this body of work and our principal conclusions. We also discuss unresolved questions and issues, and suggest possible directions of future work.

Chapter 2

Cloud and radiative balance changes in response to ENSO in observations and models

2.1 Introduction

Cloud feedbacks are known to be one of the largest sources of uncertainty in climate change predictions. A comparison of GCMs indicates that the cloud feedback amplifies the Earth's global mean temperature response to forcing by 10-50%, depending on the GCM (Bony et al., 2006). This spread in cloud feedback is not a new issue, it is a long-standing problem that is crucial in our ability to make climate change projections (Boucher et al., 2013; Stephens, 2005).

Reliable detection of climate change signals in the observational record is problematic. Hence, in this work we focus on natural variability, in particular the El Niño Southern Oscillation (ENSO) as the ENSO pattern involves large changes in cloud distribution, precipitation, reflected shortwave (SW) and outgoing longwave radiation (OLR). ENSO is the dominant form of inter-annual variability in the tropics,

occurring on a timescale of 2-7 years. The short timescale and large amplitude of the signal makes it an ideal natural forcing to focus on as we have observations of multiple events, which can be used to study the observations and models with greater certainty than given by trend analysis over the observational period.

The warm phase of this phenomenon, El Niño, is associated with large sea surface temperature (SST) increases of up to 2 °C in the eastern equatorial Pacific. Tropically averaged SSTs rise by as much as 0.5 °C during a large El Niño event, thus providing a significant forcing on the atmosphere, which responds in a complex number of ways (see figure 2.1). The primary atmospheric changes associated with an El Niño event include a weakening of the Walker circulation and an eastward shift of the western Pacific deep convection zone (Collins et al., 2010).

In this chapter we examine the relationship between radiation, cloud distribution, precipitation and ENSO by examining a variety of observational datasets and model outputs. The models used are the Geophysical Fluid Dynamics Laboratory's (GFDLs) atmosphere-only models, AM2 (used in CMIP3), the latest generation AM3, and the High Resolution Atmosphere Model (HiRAM) in two different horizontal resolutions, c180 and the higher resolution c360. AM3 and HiRAM have both been submitted to CMIP5.

2.2 Data

The time period of the model runs is 1979-2008 and all models are forced with SSTs from the HadISST dataset (Rayner et al., 2003). AM2 has a resolution of 2°latitude×2.5°longitude, with 24 vertical levels, and uses the relaxed Arakawa-Schubert convection scheme (GFDL GAMDT, 2004). AM3 (described in depth by Donner et al. (2011)) uses a cubed sphere implementation of the finite-volume dynamical core. It has the same horizontal resolution as AM2 but with 48 vertical levels,

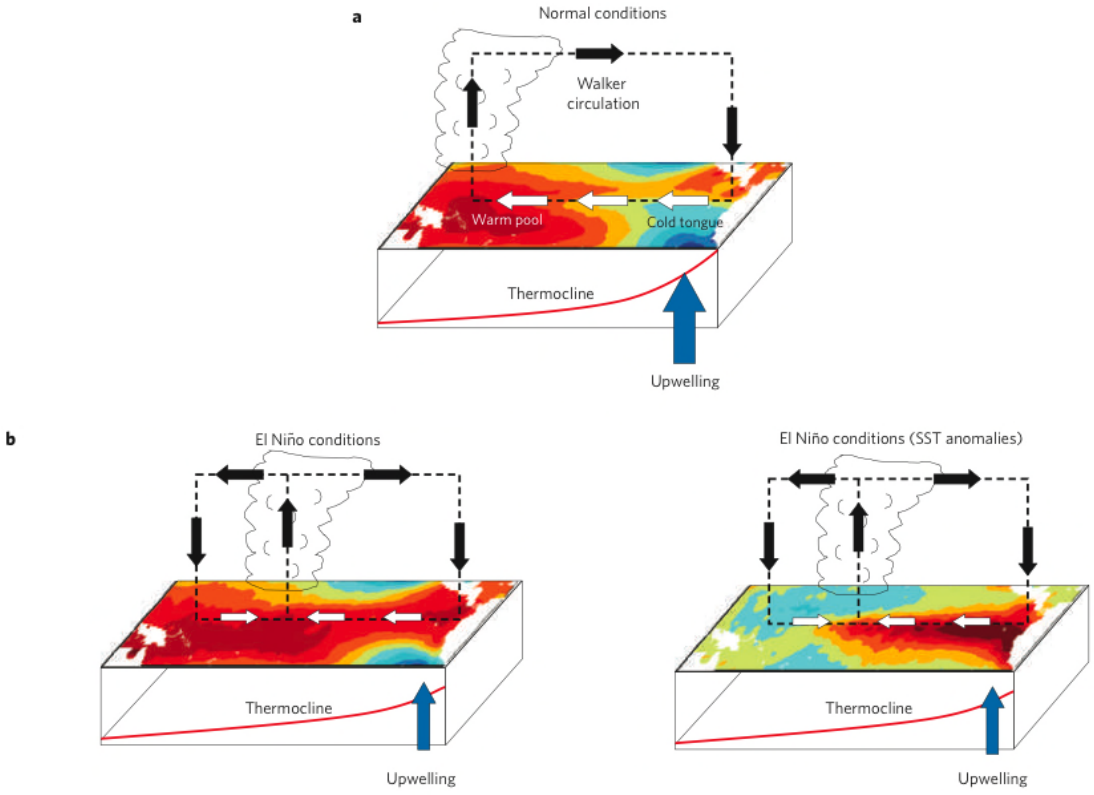


Figure 2.1: Idealized schematic showing atmospheric and oceanic conditions of the tropical Pacific region and their interactions during normal conditions and El Niño conditions. a) Mean climate conditions in the tropic Pacific, indicating SSTs, surface wind stress and associated Walker circulation, and the mean position of convection. b) Typical conditions during an El Niño event. SSTs are anomalously warm in the east; convection moves into the central Pacific; the trade winds weaken in the east and the Walker circulation is disrupted. Figure taken from Collins et al. (2010).

and uses Donner deep convection (Donner, 1993; Donner et al., 2001) and Bretherton shallow convection parameterizations (Bretherton et al., 2004). It includes mesoscale updrafts and downdrafts, which leads to more detrainment in the mid-troposphere than seen in AM2. The AM3 cloud microphysics are also substantially different as they include aerosol activation and cumulus scale vertical velocities.

HiRAM c180 and c360 have greater horizontal resolutions, with 180 and 360 latitudinal grid points between the equator and pole, respectively. This corresponds to a resolution of about 0.5° and 0.25°. HiRAM (described in Zhao et al. (2009)) also uses a cubed sphere, has 32 vertical levels and convection based on Bretherton's

shallow convection parameterization. The prognostic cloud fraction scheme used in AM2/AM3 has been replaced by a simpler diagnostic scheme assuming a sub-grid scale distribution of total water.

Observations of the top-of-atmosphere (TOA) radiation budget were provided by the Earth Radiation Budget Experiment (ERBE)(Harrison et al., 1990) and the Clouds and Earth's Radiation Energy System (CERES)(Loeb et al., 2009). Global ERBE S-4G data are available from February 1985 to May 1989, whilst tropical (i.e. 30 °S-30 °N) ERBE S-4G data are available for the longer period of November 1984 to February 1990. We have used the Energy Balanced and Filled (EBAF) version Ed2.6 of CERES, which accounts for uncertainties in absolute calibration of the measurements and the slight imbalance in net TOA flux of the current climate, using independent observations of changes in ocean heat content. This data covers the period March 2000 to December 2010.

Data from the International Satellite Cloud Climatology Project (ISCCP) was used for the cloud amounts (Rossow and Schiffer, 1991). ISCCP D2 data is available from July 1983 - June 2008. Following ISCCP, the cloud types are broken into 3 different layers based on their height. Low refers to clouds below 680hPa, mid to clouds in the range 680-440hPa, and high clouds are above 440hPa. The anomaly is calculated as the absolute increase or decrease, i.e. an increase from 40% to 60% in cloud amount would be shown as an anomaly of 20%.

In addition to the model outputs of cloud amount, AM3 was also run with an ISCCP simulator (Webb et al., 2001), and the output from this is more directly comparable to the ISCCP data provided. The main advantage of the simulator is the exclusion of optically thin clouds, which ISCCP cannot detect, as well as low/mid level clouds that are obstructed by overlying cloud decks. For the remainder of this chapter the AM3 output with the ISCCP simulator applied will be notated as AM3(sim) and

the pure model output simply as AM3. The other models, unfortunately, do not include an ISCCP simulator product.

Rainfall data were provided by the Global Precipitation Climatology Project (GPCP), NOAA/OAR/ESRL PSD, Boulder, Colorado, USA. These data are available online at their website http://www.esrl.noaa.gov/psd/ and described in Adler and Huffman (2003).

2.3 Results

2.3.1 Tropically averaged time series

Figure 2.2 shows the tropical mean seasonal cycle for OLR, reflected SW and total cloud amount, for both observations and models. The absolute values of the model radiation and cloud amounts are offset from observations by various degrees. In the OLR and SW case, the models are in closer agreement with ERBE observations (dashed red line) than CERES (solid red line), as ERBE observations were used in the development of these models. There are also notable differences in the total cloud amount in figure 2.2c, with AM3 having more, and the remaining models having less than ISCCP.

Figure 2.3 shows the tropically averaged OLR, SW and total cloud amount anomalies, plotted as a function of time. The anomalies are calculated with respect to the climatological averages, and a 5 month running mean is applied. Overall, there is reasonable agreement between the models and observations for OLR and SW (i.e. ERBE and CERES for their respective periods), with the largest differences for OLR over the ERBE period.

Wielicki et al. (2002) report a systematic underestimation of model variability on multi-year timescales, a result primarily based on comparison against ERBE non-scanner data in the 1990's. Comparison against the post-2000 period of CERES

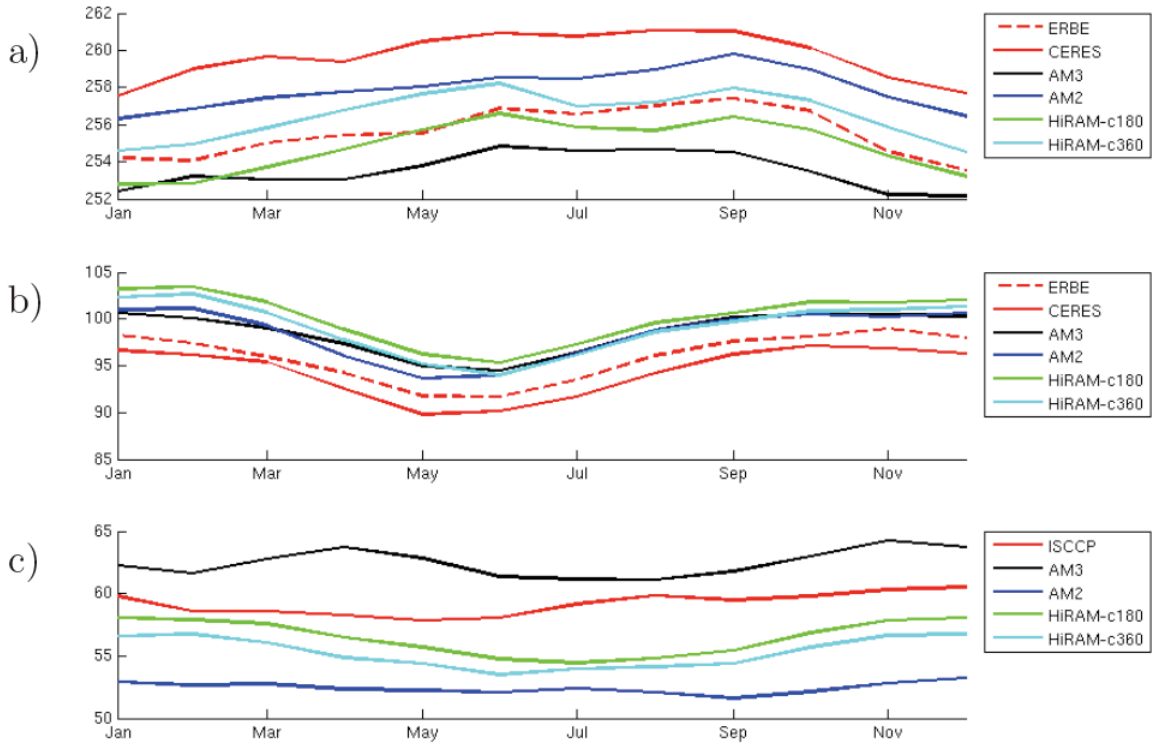


Figure 2.2: The seasonal cycle for tropically averaged a) OLR (Wm^{-2}), b) SW (Wm^{-2}) and c) Total Cloud Amount (%), is shown for observations and models. Values are calculated over the full length of each dataset.

data does not show such a disagreement. Of particular relevance here is the large discrepancy reported by Wielicki et al. (2002) for the 1997/1998 El Niño. For that particular El Niño period, Wielicki et al. (2002) show ERBE non-scanner data to have a maximum OLR anomaly of roughly $8\mathrm{Wm}^{-2}$ (i.e. about 4 to 8 times larger than the responses to the weaker El Niños observed by CERES). The models shown in their paper have a maximum OLR anomaly around $2\mathrm{Wm}^{-2}$ for this event, similar to the those of the model calculations shown here in figure 2.3. Recently, Loeb et al. (2012) published ERBE non-scanner OLR anomalies for the 1997/98 El Niño of about $5\mathrm{Wm}^{-2}$, the reduction being presumably a result of calibration adjustments. Hence, at this point it is not clear to what extent this mismatch is due to model errors and observational uncertainty.

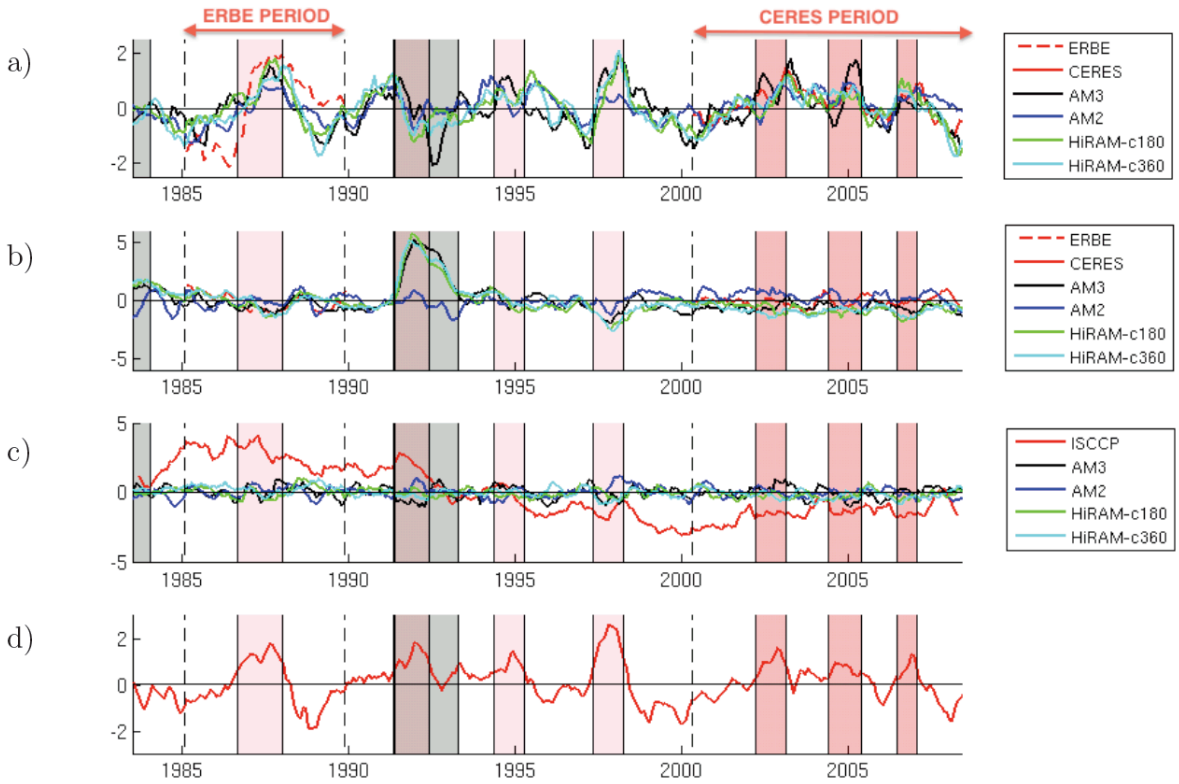


Figure 2.3: The time series of tropically averaged anomalies are shown for a) OLR (Wm^{-2}), b) SW (Wm^{-2}) and c) Total Cloud Amount (%). The Niño 3.4 index (°C) is shown in d). Periods affected by volcanic eruptions are shaded in grey, and El Niño periods are shaded in red.

In the post-2000 period examined in this chapter, however, there is good agreement between models and CERES observations.

The two areas shaded in grey indicate a 2 year period after El Chichon and Mt Pinatubo erupted. As seen in figure 2.3b, the eruptions significantly affect the SW and are therefore left out of the linear regression in section 2.3.2. AM2 is the only model that does not have a strong SW response, as volcanoes were not included in this particular run. Given that we remove these time periods from our results and focus primarily on the ERBE and CERES periods, which are free from eruptions, we believe AM2's lack of eruptive volcanoes won't be problematic.

The light red shaded periods in Figure 2.3 indicate the El Niño periods (based on the Niño 3.4 index criterion (Trenberth, 1997)), with the darker shading indicating

the three events during the CERES period that will be used for much of the analyses to follow.

The cloud anomaly time series (figure 2.3c), shows a long term trend in ISCCP that is absent in the models. This trend is an artifact of the satellite viewing geometry (Evan et al., 2007), and will be discussed further in section 2.3.3.

2.3.2 Tropically/globally averaged linear regression

In this section we analyze the relationship of tropical (defined as 30 °S-30 °N) and global mean quantities with the Niño 3.4 index by means of a linear regression. We linearly regress the averaged TOA radiation budget against the Niño 3.4 index, which is defined as the SST anomaly calculated over the region 5 °S-5 °N, 120 °-170 °W. The OLR and SW are first de-seasonalized by removing the corresponding monthly mean value. They are then regressed against the Niño 3.4 index, for all months over the various time periods, and the correlation coefficients are calculated. The 2 years of data after the volcanic eruptions, El Chichon and Mt Pinatubo, have been removed due to their strong effect on the radiation budget. Three time periods are considered. The first is February 1985 - May 1989, which corresponds to the ERBE global observation period. The second is January 1979 - December 2008, which is the length of the model runs, and the third is March 2000 - June 2008, which corresponds to the CERES time period overlap with ISCCP.

The three time periods considered are shown on the x-axis in figure 2.4, with the correlation coefficient on the y-axis. Correlations that are significant at the 95% level are plotted with larger markers. We find that for data analyzed here, the slope of the linear regression (not shown) is generally linearly related to the correlation coefficient. This result is explained when considering the ratio of the slope (β) to the correlation coefficient (ρ), which is given by:

$$\beta = \frac{\sigma_{nino3.4}}{\sigma_{radiation}}\rho \tag{2.1}$$

where $\sigma_{nino3.4}$ is the standard deviation of the Niño 3.4 index, and $\sigma_{radiation}$ is the standard deviation of the radiation. As the monthly Niño 3.4 index is model-independent, its variance is constant, and the slope is proportional to the correlation coefficient divided by the variance in radiation. For the studies here, $\sigma_{radiation}$ is similar for different models and observations, which explains the linear relationship between the β and ρ. Quantitatively, $\beta \approx 1\rho$ °C/ Wm^{-2} in the tropics, and $\beta \approx 0.5\rho$ °C/ Wm^{-2} for globally averaged quantities.

Figure 2.4a shows the correlation of the tropical OLR with the Niño 3.4 index to be positive for all datasets and time periods considered. This indicates that during an El Niño event there is an increase in the OLR. The magnitude of the correlation is smallest for ERBE and AM2. For the CERES period, the correlations for the other models and the CERES EBAF data are similar, with a value of about 0.6.

In the SW, the models have a larger spread than in the OLR, especially when we consider the 2000-2008 time period results. As we are only considering the tropics here, the spread is attributable to differences in clouds. The CERES observations show a small correlation of only -0.3, which means that there is only slightly less reflected SW (i.e. an increase in SW absorption) during an El Niño event.

For the case of global OLR regressed against Niño 3.4 (figure 2.4b), there is a weaker relationship across the board. The correlation coefficient is approximately half that of the tropically averaged values, which implies that the extra-tropical response doesn't contribute significantly to the global mean. There may also be out-of-phase contributions from the extra-tropics that reduce the global correlation coefficients.

The SW also has a smaller correlation in the global mean, and the spread is centered closer to zero, with very few correlations significant at the 95% level. This indicates that the SW response to an El Niño event is not as robust as that of the

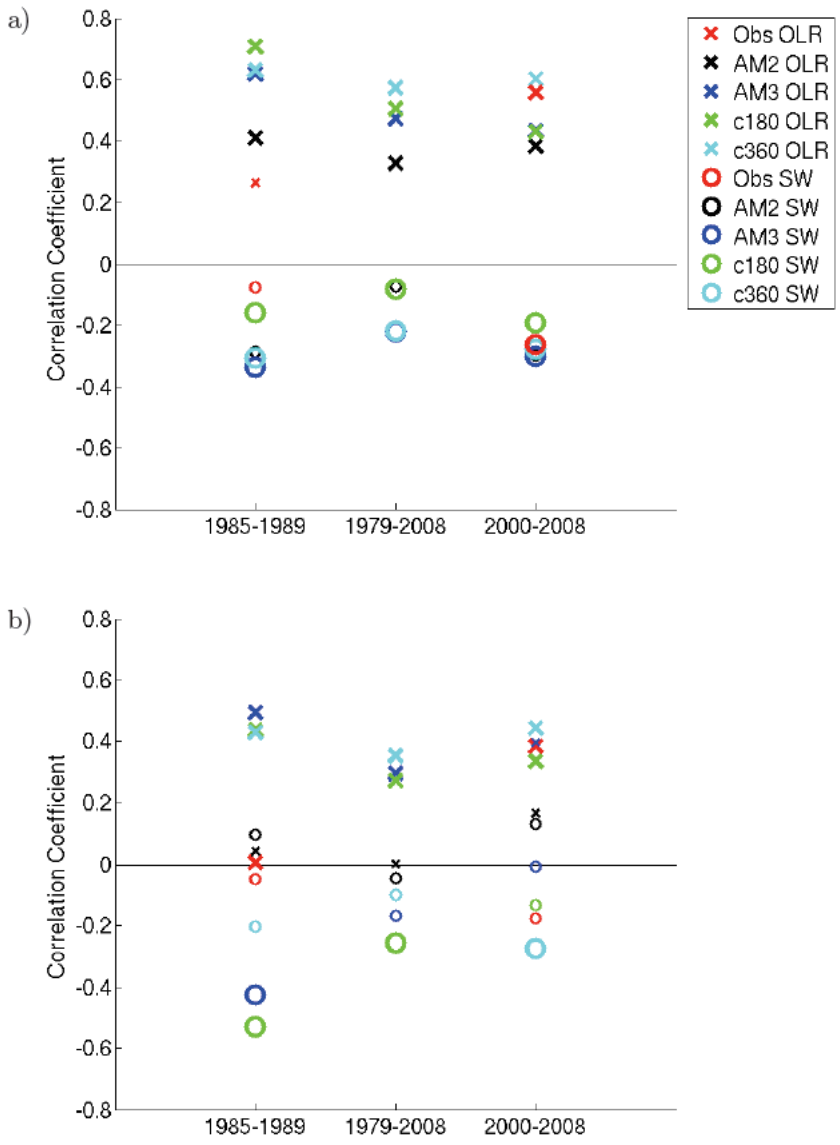


Figure 2.4: Correlation coefficient for a) tropically and b) globally averaged OLR and SW when linearly regressed against the Niño 3.4 index. The larger markers indicate significance at the 95% level.

OLR. We therefore conclude that from a tropical or global average point of view, ENSO events have a higher correlation and stronger response in the OLR than the SW. As discussed later however, this statement does not hold for local effects, which can be very large in both the OLR and SW due to changes in the locations of deep convection.

Our calculations show the linear regression of global average surface temperature against the Niño 3.4 index reaches maximum correlation at a lag of 3 months, in rough agreement with the 4 month lag found by Trenberth (2002). Similarly, the tropical average surface temperatures reach maximum correlation at 1 month lag. These lags in maximum correlations are not sharply peaked however, and make only small differences in either the linear regression slope or the correlation coefficient.

Given El Niño's seasonal phase locking, where the strongest events occur at the end of the calendar year, we also performed the linear regression for just December/January/February (DJF) months. The tropical correlation coefficient for OLR (for DJF only) increases compared to the full annual calculation, with values of 0.8 in the 2000-2008 time period. The same is true for the global correlation coefficient, with values as large as 0.6. This increase can be explained by the variance of the Niño 3.4 index, which is larger in DJF than in the annual mean, and therefore accounts for a larger fraction of the OLR variance in DJF (assuming background noise is roughly constant). This then results in a slightly larger correlation coefficient during DJF than when the regression is performed across all months. There is no consistent change in the correlation coefficients for the SW across the three time periods.

2.3.3 Differences between ERBE and CERES observations

Given the differences between the ERBE and CERES results in section 2.3.1 and 2.3.2, we investigate these two datasets more thoroughly. We first calculate the offset of the CERES data, relative to ERBE, and then investigate the regional changes in both radiation and clouds between the two time periods.

Of particular interest here is whether the differences are related to ENSO. The difference in the mean Niño 3.4 index in the CERES period relative to the ERBE period is 0.36 °C, i.e. the CERES period is on average in a more El Niño-like state

than the ERBE period, which may be expected to contribute to differences between the two periods.

	OLR mean	**LWCRF mean**	**SW mean**	**SWCRF mean**
ERBE	255.46	32.38	96.03	-43.90
AM3	253.41	29.88	98.25	-47.75
AM2	257.74	24.36	98.19	-48.84
c180	254.89	27.36	100.07	-49.49
c360	256.37	25.51	99.23	-48.73

Table 2.1: Climatological mean of tropical OLR, LWCRF, SW and SWCRF (Wm^{-2}) for the January 1985-December 1989 period.

	OLR mean	**LWCRF mean**	**SW mean**	**SWCRF mean**
CERES	259.93	27.42	94.55	-45.33
AM3	253.72	23.29	98.04	-47.51
AM2	258.24	22.72	98.83	-49.48
c180	255.01	22.06	99.40	-48.82
c360	256.76	21.72	98.34	-47.84

Table 2.2: Climatological mean of tropical OLR, SWCRF, SW and SWCRF (Wm^{-2}) for the January 2001-December 2007 period.

Tables 2.1 and 2.2 show the tropical averages of the ERBE and CERES periods, for full year periods in order to eliminate seasonal biases. CERES has a mean tropical OLR 4.5Wm^{-2} larger than that of ERBE, and a mean tropical SW 1.5Wm^{-2} smaller than ERBE. For comparison, the differences between the two periods in the model data are substantially smaller (see table 2.1 and 2.2). The question arises to what extent these large differences reflect true differences between the two periods not captured by the models, and to what extent they are a consequence of differences in measurement and post-processing of the ERBE and CERES data. A more detailed discussion on the differences between ERBE and CERES can be found in Raschke et al. (2012).

The -1.5Wm^{-2} difference in SW between the ERBE and CERES measurement may be related to differences in the assumed solar constant in the two datasets (recall

that CERES EBAF reports SW and OLR fluxes calibrated against the solar constant). For ERBE, the reported solar constant is, in terms of diurnally averaged insolation, 341.3Wm^{-2}, while for CERES the newer estimate of 340.0 Wm^{-2} is used (Loeb et al., 2009). For a typical global average albedo of $\sim 30\%$, the change in assumed incoming radiation of -1.3Wm^{-2} translates into a change in upwelling SW of about -0.4Wm^{-2}, or about a quarter of the effective difference of -1.5Wm^{-2}. Due to the calibration process, this change may also contribute to the differences in OLR, but it is clear that there remains a large difference (which is still larger than what the models show).

Assuming a linear relationship between ENSO index and average SW, OLR and SST, we can calculate an expected difference for the two periods due to the periods difference in average ENSO index of 0.36 °C. Using linear regressions, the change in ENSO index would imply a global average SST difference (higher in CERES period) of 0.02 °C for the HadISST data, while the effective difference in this dataset is 0.17 °C. For the tropical average, the corresponding numbers are 0.036 °C compared to an effective temperature difference of 0.17 °C (the tropical and global differences are indeed nearly identical between these periods). For both global and tropical averages, the effective differences are much larger than what would be expected based on the linear regression.

The models temperature responses to the change in SSTs, in turn, are around $0.2 - 0.3$ °C for globally averaged surface temperature, in reasonable agreement with the warming of 0.2 °C/decade over the 1975-2005 period reported by Hansen et al. (2006).

The same calculation for tropical OLR gives an expected increase of about 0.1Wm^{-2}, whereas the difference between CERES and ERBE is 4.5Wm^{-2}. Similarly, for tropical SW the expected change is about -0.1 Wm^{-2} and the difference between

CERES and ERBE data is $-1.5\mathrm{Wm}^{-2}$ (of which, as argued above, about $-0.4\,\mathrm{Wm}^{-2}$ may be attributed to calibration against different solar constants).

A linear regression against the ENSO index is, of course, a simplification that in particular does not account for the fact that ENSO events may occur in different flavors. Nonetheless, it appears to us that the difference in average ENSO state is probably not the main contributor to the large differences between the ERBE and CERES radiation data.

Further insight may be obtained from analysis of the spatial pattern of the difference between ERBE and CERES data. Figure 2.5a shows the CERES minus ERBE field for OLR after removal of the area average offset of $+4.5\mathrm{Wm}^{-2}$, Figure 2.5b shows the corresponding difference for SW after removal of the area average offset of $-1.5\mathrm{Wm}^{-2}$.

For large parts of the tropics (e.g. Africa south of the equator, the Amazon region and the South Pacific Convergence Zone and ITCZ over the Pacific), there is actually a remarkable see-saw between the changes in OLR and SW. Such a see-saw is expected for changes in the locations of deep convective clouds (which reduce OLR and increase reflected SW).

The equivalent of figure 2.5 for the four models is not shown, however the spatial pattern is remarkably similar to the observations, but with differences in magnitude. The variance in figure 2.5a for the observed OLR is $8.5(\mathrm{Wm}^{-2})^2$, whereas the variance for AM3, for example, is $18.9(\mathrm{Wm}^{-2})^2$.

Since ISCCP spans both periods, one may wonder to what extent that data can provide additional insights, specifically also whether the changes in OLR and SW pattern are consistent with ISCCP cloud changes.

Figure 2.5c shows the differences in ISCCP total cloud amount between the two periods, and figure 2.5d shows the differences in ISCCP high cloud amount. Comparison between figures 2.5a,b and d, shows that indeed the differences in OLR/SW in

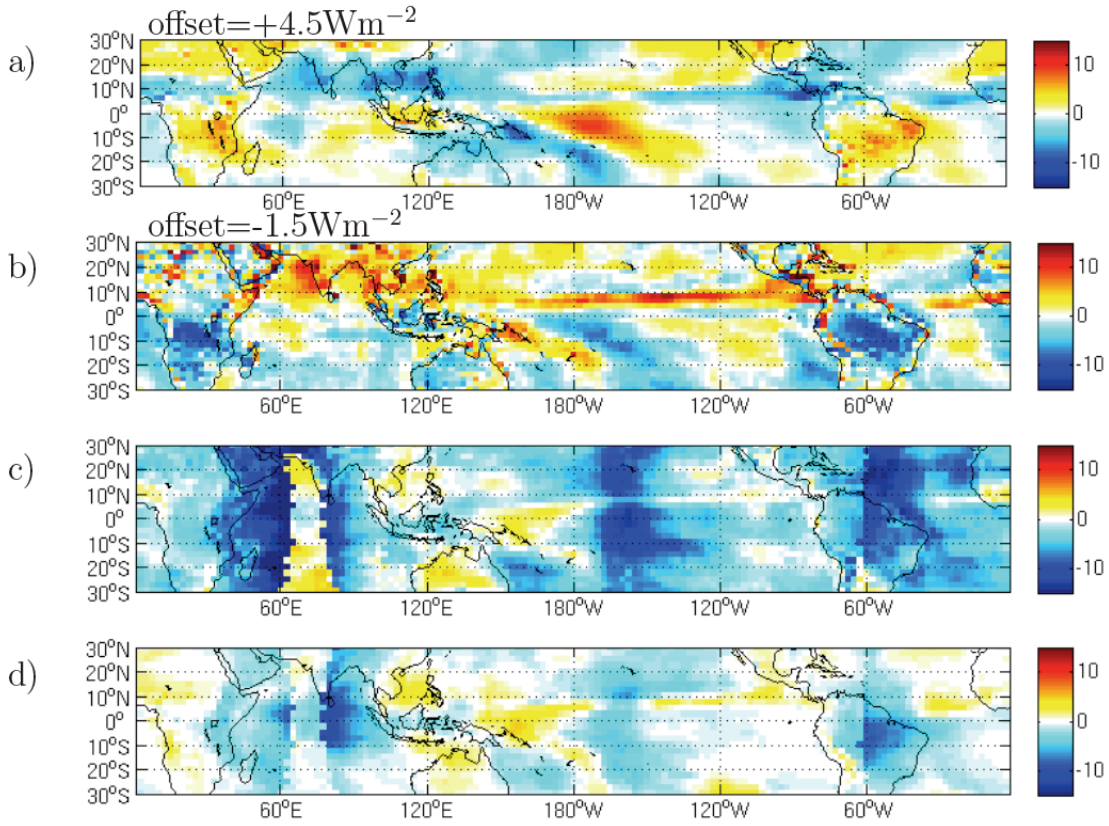


Figure 2.5: a) Mean CERES OLR minus mean ERBE OLR (with 4.5Wm^{-2} offset removed), b) Mean CERES SW minus mean ERBE SW (with -1.5 Wm^{-2} offset removed). Also shown is the difference in ISCCP mean c) Total and d) high cloud amount (%) for the CERES minus ERBE period. Only full year periods are used.

the eastern equatorial Pacific sector have the expected counterpart of an increase in high clouds north of the equator. Much of the differences in ISCCP cloud occurrence, however, is quite obviously an artefact arising from the major satellite changes, as described by Evan et al. (2007) and Knapp (2008).

With the models giving some credibility to the spatial pattern in OLR and SW of the difference between ERBE and CERES, it may be instructive to compare the pattern against a 'typical' ENSO pattern. Figure 2.6 shows a composite of the OLR/SW anomalies over the three El Niño events of the CERES time period (as shown on figure 2.3). Very prominent differences between the two patterns are seen over South

America and Africa, where the difference between CERES and ERBE is large but the ENSO pattern is weak.

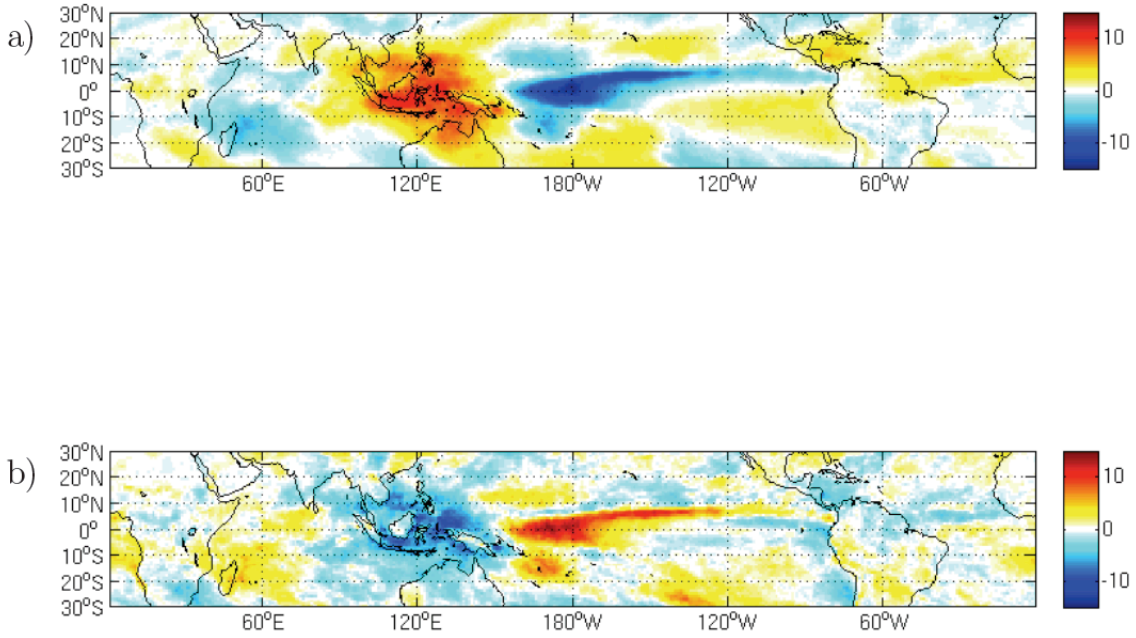


Figure 2.6: Composite of CERES a) OLR and b) SW anomalies (Wm^{-2}) during three El Niño events from 2001-2007. Anomalies are defined as the difference from the CERES EBAF 2001-2007 climatological mean.

To summarize, the area average offsets between ERBE and CERES are likely in no small part the result of differences in the measurement and post-processing of the ERBE and CERES data, with only a smaller contribution from the CERES period being on average more El Niño like than the ERBE period. The spatial pattern of the differences between ERBE and CERES is consistent with this finding inasmuch as it only weakly projects onto a 'typical' ENSO pattern. In contrast to the tropical average differences in OLR and SW, however, the spatial pattern may in fact reflect also true changes arising from changes in locations of clouds, specifically deep convective clouds. Problems in the ISCCP data, however, unfortunately prevent clear conclusions.

2.3.4 Base state regional results

The tropical average base state OLR and SW are shown in table 2.2 for CERES and the four models. The largest differences between CERES and the models are 6Wm^{-2}, with smaller differences between the models and ERBE, which is not surprising given that the model development was influenced by the ERBE data. A comparison between unbiased rms differences and correlations against CERES and ERBE show that AM3 agrees better with observations for SW than AM2 does (Donner et al., 2011), while for OLR the two models perform similarly.

Figure 2.7 shows the regional OLR difference, with the area-average bias removed, between the models and the CERES observations over the 2001-2007 time period. The bias for each model is calculated from the base state values in table 2.2. Despite the identical SSTs there are strong regional differences in the models. The western warm pool and Amazon region are persistent problem areas, particularly for AM2 and AM3. For example, the bias in the western Pacific in AM3 relative to CERES is as large as -36Wm^{-2}. The biases are smaller in HiRAM, with little influence of the models' spatial resolution as HiRAM c180 and c360 are very similar.

The same analysis is performed for the SW in figure 2.8. Similar to OLR, large differences are seen in the western warm pool, but the maxima are found off the western coasts of North America, South America and Africa. The bias is greatest off the coast of South America in AM2 and AM3, with a magnitude of -70Wm^{-2}, and the HiRAM models are only slightly better with biases of order -60Wm^{-2}. These regions are dominated by low-level stratus decks. The models' negative bias, relative to CERES, indicates that there are either too few clouds in this region or that they are not sufficiently bright so as to reproduce the observed albedo (see figure 2.8). This strong local SW bias is also the dominant signal when we examine the net TOA radiation budget. This is because the western Pacific has large local biases in both the SW and OLR, which cancel in the net to give reasonable agreement with observations.

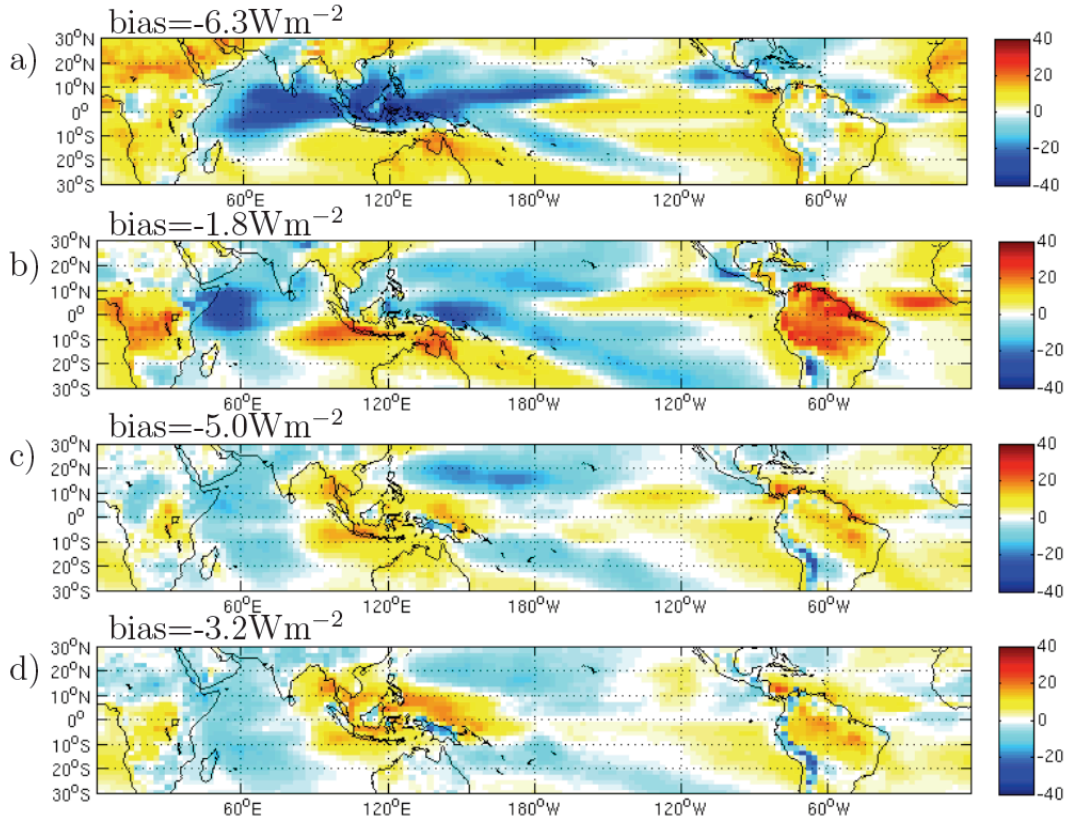


Figure 2.7: Climatological mean OLR (Wm^{-2}) in models minus CERES observations for a) AM3, b) AM2, c) HiRAM - c180 and d) HiRAM - c360.

There is no such local cancellation effect when considering the low level stratus clouds, as they only have a very small influence on the OLR, but a large influence on the SW. The small net SW bias of the tropical average (e.g. 3.5Wm^{-2} for AM3), implies that the large local biases are compensated by biases of opposite sign in other parts of the domain.

Analysis of high cloud amount shows that this explains the large radiation anomalies in the western Pacific, as AM3(sim) has roughly 1.7 times the high cloud amount reported by ISCCP. The other models also appear to have significantly larger high cloud amounts than ISCCP, as shown in table 2.3, although it is difficult to say exactly how much without the use of an ISCCP simulator. Comparison between AM3(sim) and AM3 shows that the ISCCP method fails to detect about 7% of the model clouds. The equivalent number for observations is not known.

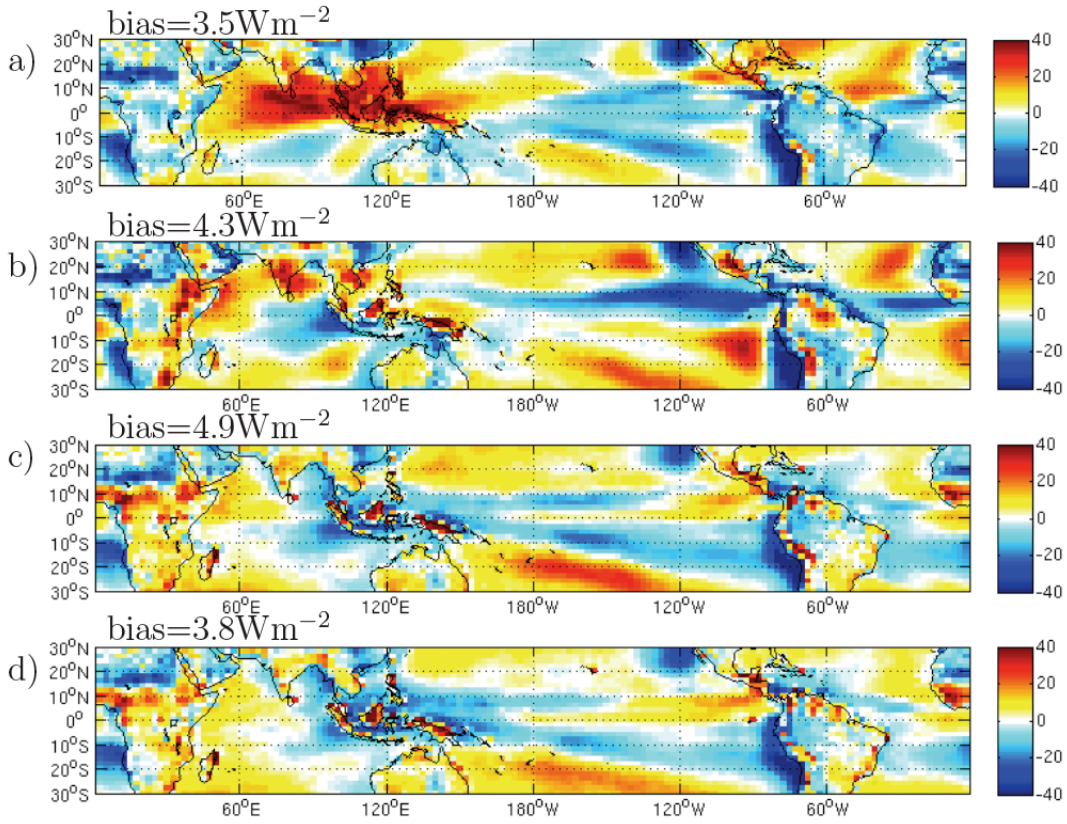


Figure 2.8: Climatological mean SW (Wm^{-2}) in models minus CERES observations for a) AM3, b) AM2, c) HiRAM - c180 and d) HiRAM - c360.

It is more difficult to make comparisons between the observations and models for mid- and low-level cloud amounts. Although we have the ISCCP simulator for AM3, the lower level clouds will be partially obscured by AM3's excessive high cloud amount. This can be seen in the differences between AM3(sim) and AM3 for the mid- and low-level cloud amounts (table 2.3), where the cloud fraction is significantly reduced when the ISCCP simulator is applied. However, given that all model outputs have smaller values than ISCCP we can state that there are too few mid-level clouds in the models. Exactly what this difference is though is difficult to say. A similar scenario is likely true for the low-level clouds, but of course there is now masking from both mid and high level clouds, so no definitive conclusions can be made.

	High	High anom	Mid	Mid anom	Low	Low anom
ISCCP	24.25	0.12	12.24	-0.09	20.87	-0.13
AM3(sim)	40.41	0.05	6.37	-0.08	13.29	-0.07
AM3	47.26	0.06	9.04	-0.11	24.62	-0.07
AM2	31.83	-0.06	10.80	0.01	25.34	-0.00
c180	39.85	-0.05	6.07	-0.06	26.55	-0.07
c360	38.15	-0.12	5.24	-0.01	26.76	-0.06

Table 2.3: Tropical average cloud base state amount and anomalies (%) during El Niño events for the January 2001-December 2007 period.

The high cloud base states for ISCCP and the four models are shown in figure 2.9. ISCCP has a maximum high cloud amount in the western Pacific of ∼30%, whereas AM3(sim) shows amounts of ∼50%. We have broken down the high cloud fraction into three optical depth (τ) categories - thin ($\tau < 3.6$), medium ($3.6 < \tau < 23$) and thick ($\tau > 23$), as defined by ISCCP, and averaged the cloud amounts over the latitudinal band 30 °S-30 °N. Whilst AM3(sim) overestimates the high cloud fraction across all optical depths, the difference is largest for the thin clouds with an overestimation of 10-15% cloud amount. The difference for the high clouds of medium optical thickness is 5-10% and <5% for the optically thick clouds. Also shown on this figure are the total high cloud amounts for all models, without being run through an ISCCP simulator. The overestimation of high clouds is not isolated to the western Pacific, and we see high cloud amount larger than ISCCP in all four models across the entire tropical Pacific. In the eastern Pacific the effect on the radiation budget however is not as large because the absolute values of cloud amount are lower in both observations and models. As mentioned above, applying the simulator to AM3 decreases the high cloud amount by roughly 7%, and whilst AM2 and HiRAM still have more high cloud than ISCCP they are in closer agreement with observations than AM3.

Figure 2.10 indicates this large high cloud bias of models against ISCCP is partially compensated for by a bias in the mid-level clouds. The ISCCP base state has ∼15% mid-level cloud amount in the western Pacific, however AM3 with the ISCCP

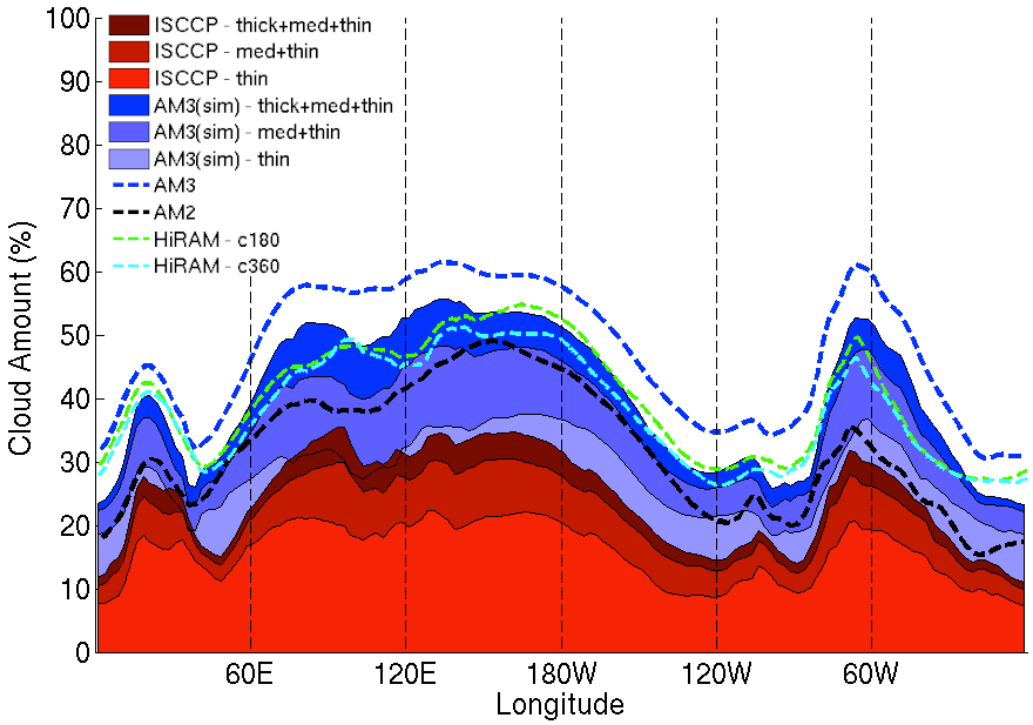


Figure 2.9: Climatological mean of high cloud amount (%) for ISCCP and AM3 with ISCCP simulator. The values are meridionally averaged from 30 °S-30 °N and plotted as a function of longitude for 3 different optical depth categories - thin, medium and thick. Dashed lines are total high cloud amounts from AM3, AM2, HiRAM-c180 and HiRAM - c360.

simulator shows 10%. Again, this difference is primarily due to thin clouds, followed by clouds of medium optical depth and negligible contribution by the very thick clouds, and extends across the tropical Pacific. When the ISCCP simulator is applied to AM3 for mid-level clouds there is a decrease in cloud amount. This difference between the AM3 and AM3(sim) case is larger than for the high cloud case, and is presumably caused by the masking effect of higher-level clouds.

Whilst these results may suggest AM2 cloud amounts are in better agreement with ISCCP observations, Klein et al. (2013) used an ISCCP simulator to show that AM3 is in fact an improvement over AM2 for both cloud properties and SW-relevant cloud properties.

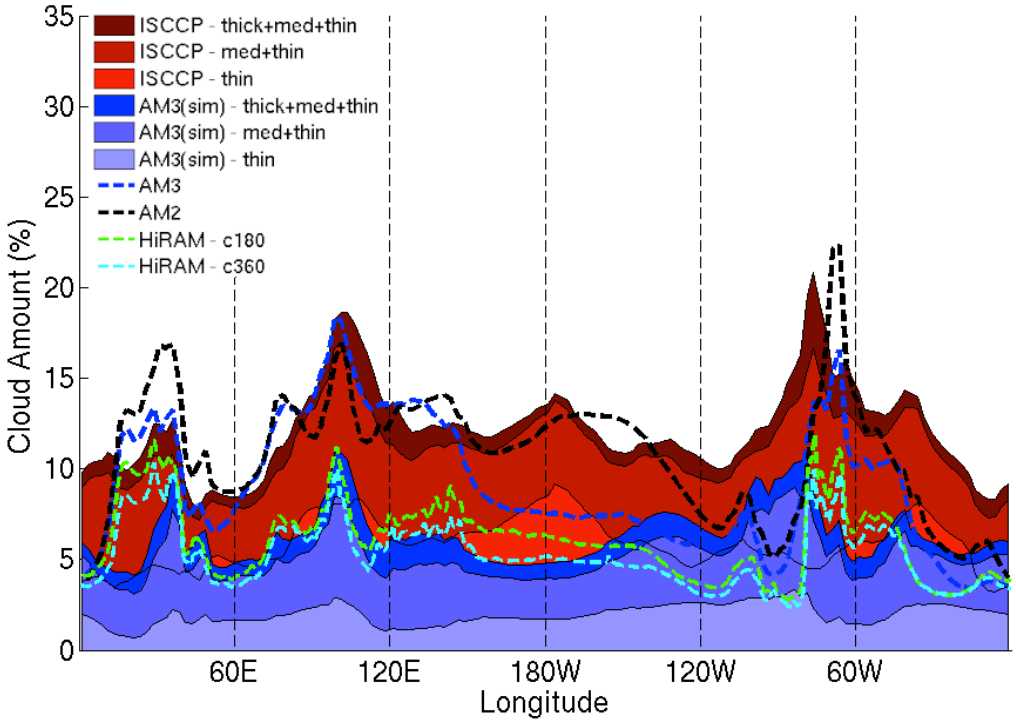


Figure 2.10: Same as figure 2.9 but for mid-level clouds.

The large SW bias of models against CERES off the coast of South America is consistent with the bias in the low cloud amounts of models relative to ISCCP. ISCCP observations have roughly 10% more low cloud amount than is shown by AM3 with the ISCCP simulator (figure 2.11). ISCCP also has significantly more low cloud amount across the entire tropics than is shown by AM3 with the simulator. The bias is smaller for AM2 and HiRAM, since these models have slightly larger low cloud amount than AM3, but lack of ISCCP simulator data products disallows quantification.

2.3.5 Regional TOA radiation anomalies

In contrast to the tropical average values, local anomalies frequently have a non-monotonic relationship with the Niño 3.4 index, rendering the linear regression approach inadequate. Instead, periods of El Niño events are examined, which are defined to be when the 5 month running mean of the Niño 3.4 index exceeds a magnitude

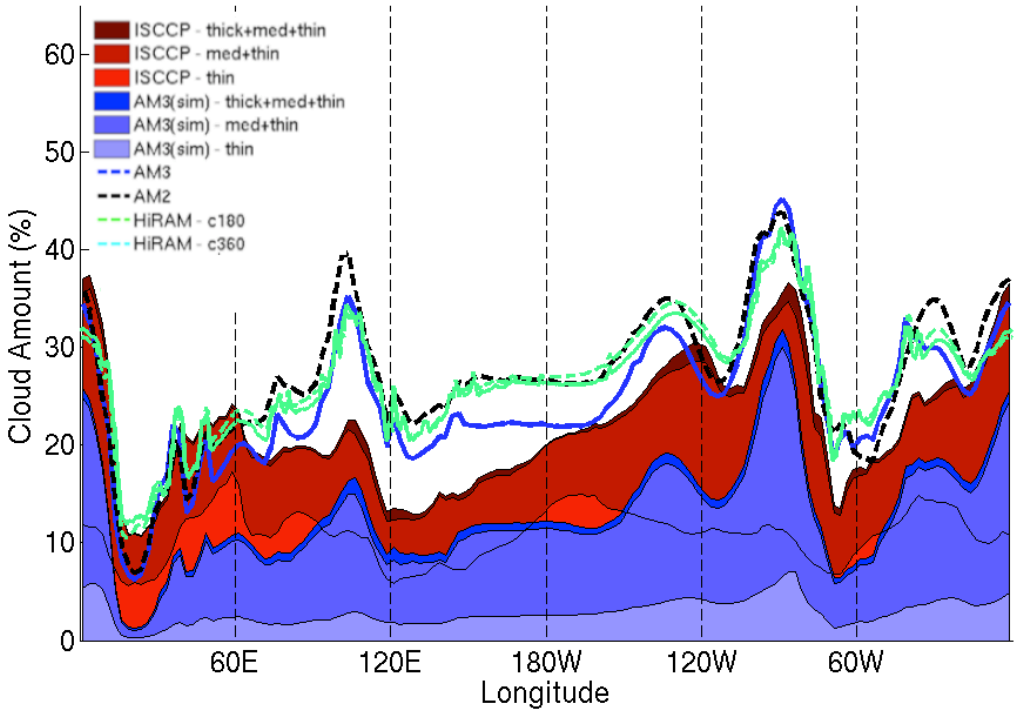


Figure 2.11: Same as figure 2.9 but for low-level clouds.

of 0.5 °C for at least 6 months (Trenberth, 1997). Due to the incompletely understood differences between ERBE and CERES, discussed in section 2.3.3, we restrict this analysis to CERES data, where 3 El Niño events occur within the 2001-2007 period. These events occur from April 2002-March 2003, June 2004-June 2005 and July 2006-February 2007 (see Figure 2.3). For each period, we calculate the PDFs of the anomalies for the quantities of interest.

The anomalies are defined as the difference between the monthly mean outgoing TOA radiation and the climatological mean over the CERES period. There will be some element of a seasonal bias as we are combining odd numbers of winter and summer months. However, since we focus on comparisons of observations to models over identical periods, the preference for certain seasons is not problematic.

Figure 2.12a shows the probability distribution of tropical OLR anomalies for CERES and the models, for all three El Niño events. We note a tendency for the models to have a longer negative tail than the CERES data, and a longer positive

tail for AM3. Inspection of the maps of the anomalies shows that the large tail of the negative anomalies in AM3, for example, arises from the central Pacific where AM3 has local anomalies in OLR of up to -99Wm^{-2} compared to -56Wm^{-2} for CERES. The PDF of the clear sky OLR anomalies (not shown) shows very good agreement between observations and all models, such that the differences in the PDFs of all-sky OLR is a consequence of the models' clouds, in particular upper tropospheric convective clouds.

The corresponding SW PDF is shown in figure 2.12b. Even more pronounced than with OLR, the models have larger tails than CERES, especially when we compare the probability of large negative anomalies. In other words, the variance of the anomalies during El Niño events is larger in models than observations. As discussed in section 2.3.3, a similar result was also found for the variance in the difference between the average ERBE and average CERES period, which was also larger in models than observations.

The tropical average OLR anomalies for El Niño events are shown in table 2.4. There is very good agreement between CERES and the models, perhaps with the exception of AM2, which has a weak response. Longwave Cloud Radiative Forcing (LWCRF), defined as the clear sky minus all sky values, shows the increase in OLR is no more than 50% due to a reduction in LWCRF. The remaining increase in OLR is therefore due to an increase in the clear-sky OLR. The tropical average SW anomalies are also shown in table 2.4. The SW anomalies in models vary in both sign and magnitude as we might expect from the weak correlations shown in figure 2.4, but are within 0.3Wm^{-2} of the CERES SW anomaly.

The generally good agreement of tropical average El Niño response in OLR and SW may seem surprising given the differences in the PDFs of local anomalies. The implication is that apparently the positive and negative *differences* in the PDFs largely

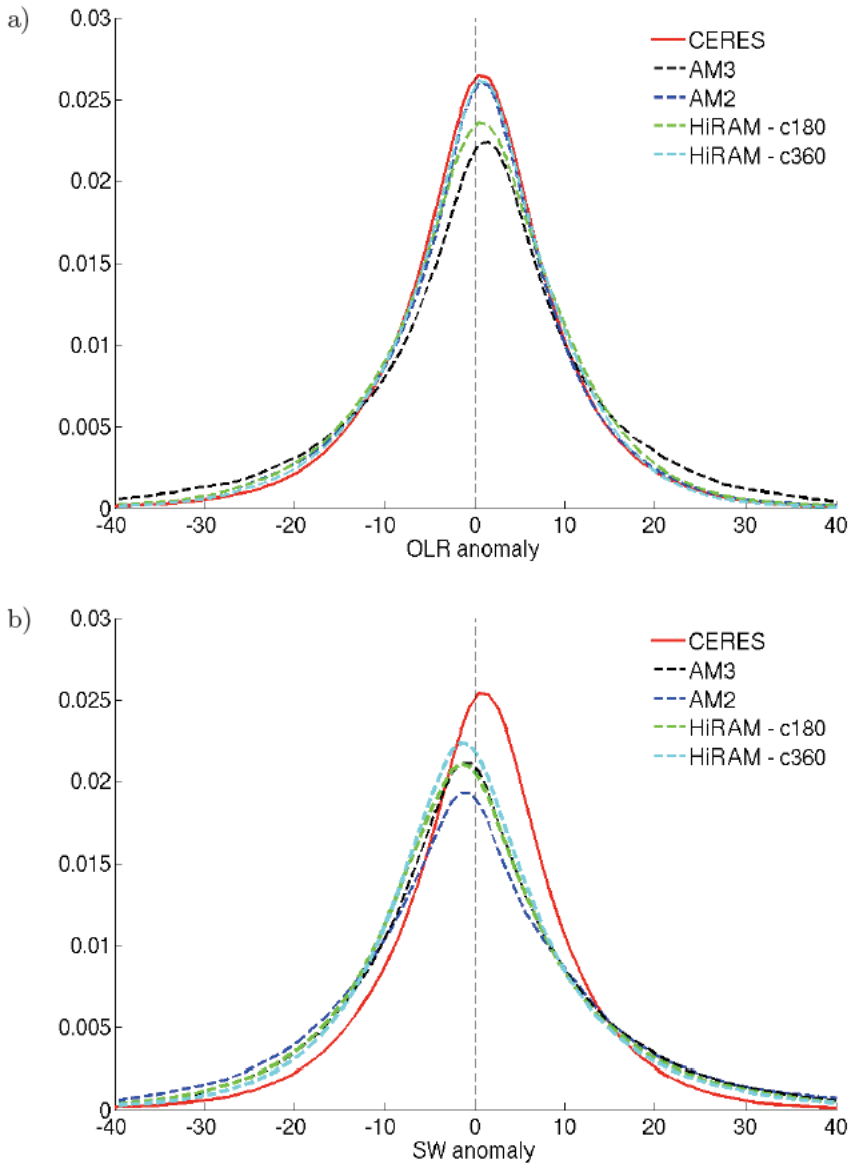


Figure 2.12: Probability distribution for a) OLR and b) SW anomalies (Wm^{-2}) for CERES, AM2, AM3, HiRAM c180 and c360 during 2001-2007 El Niño events.

cancel, which is remarkable in particular for the SW where the CERES and models PDFs differ quite substantially. In the following, we analyze this result in more detail.

2.3.6 Scaling of anomalies with the base state

We hypothesize that the differences in the PDFs of the anomalies are related to differences in the base state of models and observations. For example, if OLR and

	OLR anom	LWCRF anom	SW anom	SWCRF anom
CERES	0.35	-0.20	-0.04	0.10
AM3	0.29	0.05	-0.06	0.05
AM2	0.10	-0.03	-0.01	-0.00
c180	0.18	-0.11	-0.25	0.24
c360	0.23	-0.08	-0.11	0.10

Table 2.4: Tropical average OLR, LWCRF, SW and SWCRF (Wm^{-2}) anomalies during El Niño events for the January 2001-December 2007 period.

SW are linearly related to cloud amount, and total cloud amount was conserved, the same local fractional change in cloud amount would result in a stronger OLR and SW response for the case with a larger base state cloud amount. It also follows that for this scenario, differences in the redistribution of cloud amount in space give differences in the shape of the PDF of the anomalies, but that the sum over all PDFs necessarily evaluates to zero.

In reality, there is not a simple linear relationship between cloud amount and the cloud radiative effect, and explaining the behaviour of the SW and OLR anomaly PDFs is not straightforward. However, we find that this reasoning explains the response in high cloud amount remarkably well. Figure 2.13a shows the probability distribution of high cloud amount during the three El Niño periods for ISCCP, AM3(sim) and the four model outputs. As in the case of SW and OLR, the models' high cloud anomaly PDFs have longer tails. The models also have larger high cloud amounts in the base state (section 2.3.4) and, everything else being equal, one would expect the high cloud anomalies to scale like the ratio of the base state cloud amount. From table 2.3, we calculate the high cloud amount ratio for each model relative to ISCCP and divide the models high cloud anomalies with this factor. For example, for AM3(sim) we get a ratio of $40.41/24.25 \sim 1.7$ that we divide the AM3(sim) high cloud anomalies with. The resulting PDFs are shown in figure 2.13b. While not perfect, it is evident that the scaled high cloud PDFs of the models are in much bet-

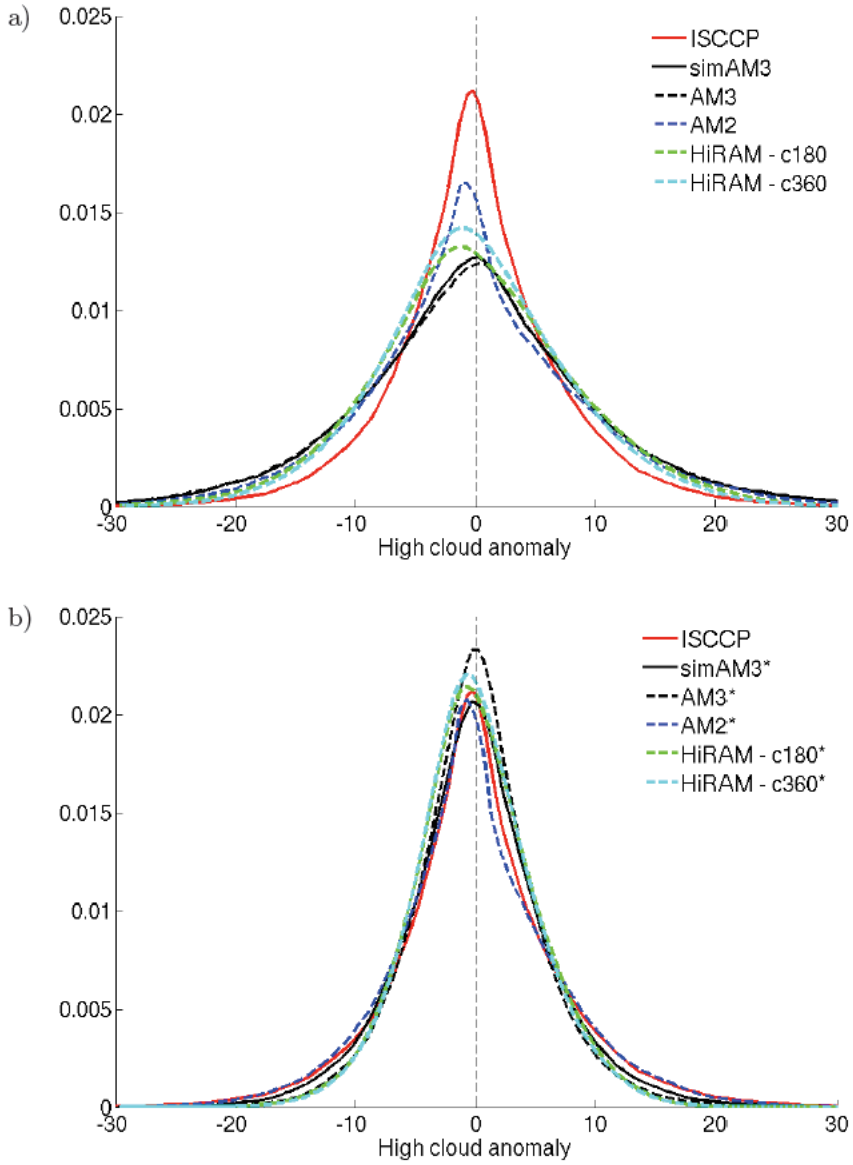


Figure 2.13: PDF of a) raw and b) scaled high cloud anomaly (%) during 2001-2007 El Niño events for ISCCP, AM3 with and without simulator, AM2, HiRAM - c180, and HiRAM - c360. Scaling factors are taken from the biases in base state high cloud amounts in table 2.3.

ter agreement with the ISCCP anomalies. This result implies that, at least for high cloud amount, the problem is reasonably linear, and that (i) biases in the models' base states are the primary cause of the local biases in the anomalies during El Niño (as opposed to errors in the redistribution of convection during El Niño); and (ii) that

the local biases in the anomalies during El Niño necessarily largely cancel in the area average.

This scaling of anomalies cannot be used for the mid- and low-level cloud PDFs because of problems caused by high cloud masking, which make it difficult to compare ISCCP with models.

We may expect the scaling to work for precipitation, however, as convective rainfall and high cloud amount are closely related. The base state mean precipitation values are shown in table 2.5. All of the models have larger mean precipitation than GPCP data, by a factor of approximately 1.2. (It has been suggested that GPCP may underestimate global mean precipitation; (Kato et al., 2011) argue that the net surface irradiances imply global mean precipitation about 10-20% higher than GPCP, and Stephens et al. (2012) argue based on satellite observations that global mean rainfall is likely between the GPCP estimate and 25% higher.)

Despite the models base state bias in precipitation, the PDFs of the models anomalies agree surprisingly well with GPCP observations. Therefore, scaling of the anomalies has only a small effect on the PDFs and does not significantly improve the results.

Given the close relationship between high cloud amount and precipitation, it is perhaps surprising the model precipitation base states agree better with GPCP than the model high cloud amount with ISCCP data. Consequently, the ratio of high cloud amount to precipitation will be different in models than in observations. AM3(sim) has a base state ratio of optically thick high-level cloud to precipitation of 1.3 %/(mm/day). ISCCP and GPCP observations put this ratio at approximately 0.9%/(mm/day), a lower cloud fraction per rain rate. During El Niño events the tropical average has perturbations about the base state of order $\pm 1\%$ of the optically thick high cloud and perturbations of order $\pm 0.1\%$ in precipitation. Given the unknown signs of these perturbations, which are dependent on the exact definition of

the base state period, the change in high cloud to precipitation ratio during El Niño events cannot be determined reliably.

	Tropical Mean	**Global Mean**
GPCP	3.01	2.65
AM3	3.68	3.04
AM2	3.64	2.93
c180	3.58	2.97
c360	3.59	2.98

Table 2.5: Climatological mean precipitation (mm/day) for the January 2001-December 2007 period.

The large local cloud anomalies average out to small anomalies in both the tropical and global average. For the high cloud amounts the largest tropical anomaly in models and observations is <0.15% and the largest global anomaly is <0.25% (as shown in table 2.3). ISCCP has the smallest mean high cloud amount, but has the largest tropical and global high cloud anomaly. Thus, our scaling argument only works for the shape of the PDFs but does not explain the ratio of the tropical mean anomalies.

It is also of interest to note the tropically and globally averaged values of both LWCRF and SWCRF (table 2.4). The tropically averaged LWCRF anomalies for El Niño events are no greater than 1% of the base state value and are even less for the SWCRF. In the global average, these numbers have decreased further to $< 0.2\%$. This is a surprising result given the large biases in the base state cloud and radiation fields, as well as the differences in the high cloud anomaly PDF. It appears that, in both models and observations, the cloud radiative effect is rather insensitive to perturbations.

2.4 Summary and Conclusions

Regressing the observed tropical OLR against the Niño 3.4 index results in a strong positive correlation of 0.6. The corresponding correlation coefficient for the tropical

SW case is -0.2. The four models analyzed were found to be in good agreement for the OLR but showed a large spread for the SW.

There are large differences between the ERBE and CERES OLR/SW observations. This is evident in not only the tropically averaged climatological values, but also in the unbiased regional differences between the two time periods. Relative to ERBE, CERES is determined to have an OLR offset of $+4.5\text{Wm}^{-2}$ and a SW offset of -1.5Wm^{-2}. The CERES period is a more El Niño-like period than that of ERBE, however, the differences in the period average OLR and SW are much larger than what would be expected based on the period average ENSO state difference, and the slope of a linear regression of OLR/SW against ENSO index.

The cause of the regional differences between the two time periods is unknown. The four models, however, all exhibit similar regional differences, which suggests they are not an artifact of the satellite calibration and post-processing, but due to a climatological difference. To what extent these differences influence the differences between the periods in the correlation coefficients between Niño 3.4 and OLR/SW (see figure 2.4) is unclear. Nevertheless, given the general uncertainty surrounding cloud and water vapor feedbacks, the regional agreement between the satellite observations and the models, which, among themselves, have substantial differences in their formulation of clouds and convection, is perhaps surprising and encouraging.

Comparison of the four models with CERES and ISCCP data shows large biases in the base states. In the OLR/SW fields, the biases are large on the regional scale but agree well with observations in the tropical mean. The high cloud amount in AM3, for example, is roughly double that of ISCCP observations in the base state, thus causing local OLR biases of up to -36Wm^{-2}, particularly in the western Pacific warm pool. There are also SW biases of up to -70Wm^{-2} in the stratus deck regions, where all four models appear to have too little low cloud amount. Exact mid/low cloud biases are difficult to determine due to the masking effect of high clouds.

The model high cloud amount bias, relative to ISCCP, is also evident in the anomalies during El Niño events. This is shown by the PDFs of anomalies having much longer tails for the models than for observations. A linear scaling approach is introduced, whereby each grid-point anomaly is scaled by the model-to-observation tropically averaged base state ratio. This results in the model PDFs being in much closer agreement with observations. This works for high cloud amount but not for OLR/SW, as the tropical average is in close agreement with observations.

While this scaling argument reasonably explains the differences in the shape of the PDFs, it provides little quantitative insight into the behavior of the tropical average during El Niño. For example, in the base state, AM3 has 1.7 times the high cloud amount observed by ISCCP. AM3's high cloud tropically averaged anomaly during El Niño events, however, is only 0.4 times the corresponding ISCCP high cloud anomaly.

Regardless of the base state, there is a considerable amount of symmetry and therefore cancellation between the large positive and negative anomalies. This results in the tropically averaged cloud amount and cloud radiative forcing anomalies being less than 0.5% and 0.2% of the base state, respectively.

As seen in section 2.3.3, 2.3.4 and 2.3.6, the models consistently have larger regional anomalies than seen in observations, even though they might have a smaller tropically averaged anomaly. This can have important implications for calculated values of "feedback" or "sensitivity", as the models have greater sensitivity than observations locally, but smaller sensitivity in the tropical mean.

Chapter 3

The role of large-scale convective organization for tropical high cloud properties

3.1 Introduction

High clouds act to both cool and warm the surface by reflecting shortwave radiation and trapping long wave radiation. The negative shortwave radiative effect has been shown to roughly cancel the positive longwave radiative effect (Kiehl, 1994), therefore, high clouds are often considered a secondary source of uncertainty in climate models, compared to low clouds (Bony and Dufresne, 2005). Nevertheless, changes in high cloud altitude, diurnal distribution and fractional coverage may induce changes in radiative forcing. Here, we study the factors that control tropical high cloud *amount* and its relation to deep convection, a topic that has received somewhat less attention than the altitude of deep convective clouds (Hartmann and Larson (2002)). High cloud amount is defined as the two-dimensional cloud fraction above 440hPa, consistent with the ISCCP product definition (Rossow and Schiffer, 1991).

Several simplified models have been shown to exhibit a decrease in convective area when the zonal surface temperature (T_s) gradients increase (Bretherton and Sobel, 2002; Larson and Hartmann, 2003; Ramanathan and Collins, 1991) . Given that high cloud production primary occurs in regions of deep convection, we would expect a change in convective area to induce a change in high cloud amount. Whilst the ISCCP dataset has nearly 30 years of high cloud amount observations, there are large uncertainties (Evan et al., 2007), that complicate the analysis of high cloud amount variability. Due to these observational uncertainties, we study the behaviour of tropical (30 °S-30 °N) high cloud amount with the GFDL AM2 atmospheric general circulation model (GFDL GAMDT, 2004), forced with prescribed perturbations to observed sea surface temperatures (SSTs). Quantitatively, results may depend on model formulation, and we therefore emphasize here the framework of the analysis that provides a physically plausible interpretation of the model results and involved mechanisms.

3.2 Experimental Setup

3.2.1 General Circulation Model

The Geophysical Fluid Dynamics Laboratory's (GFDLs) atmosphere-only model AM2 (GFDL GAMDT, 2004) has a horizontal resolution of 2°latitude×2.5°longitude, with 24 vertical levels and uses the relaxed Arakawa-Schubert convection scheme. The control run uses the HadISST (Rayner et al., 2003) and atmospheric forcings for the period 1979-2008. The 8 perturbation experiments all modify the time-evolving SSTs, and have the same forcings as the control run. For each perturbation, the results reported are the differences between the perturbed and control run averaged over the period 1979-2008.

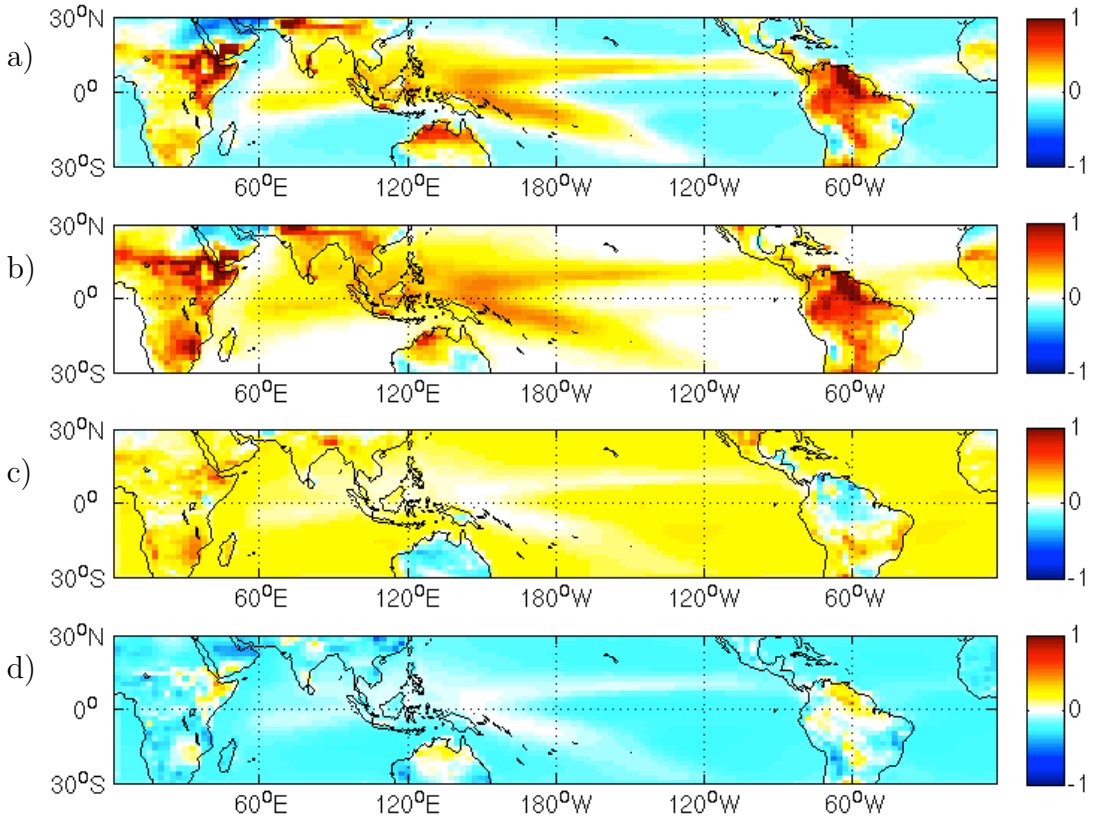


Figure 3.1: Climatological mean surface temperature changes (K) for experiments a) A, b) B, c) C, and d) D, as outlined in table 3.1. Positive values indicate an increase in temperature from the control run.

3.2.2 SST perturbations

The tropical SST and convection distributions are emerging properties of the coupled ocean-atmosphere system, with radiative, latent and sensible heat fluxes, as well as advective heat and moisture fluxes, constraining the distributions. By perturbing the SST distribution we probe the system for the sensitivity of, in this case, high cloud amount, but we do not imply that in the coupled ocean-atmosphere system temperatures in any one part of the tropics could change independently of the rest of the tropics. Specifically, one might expect that the energetic constraints enforce some stability in the large-scale distributions of SSTs and deep convection (Sobel et al., 2002) and hence also in high cloud amount. The model calculations shown below

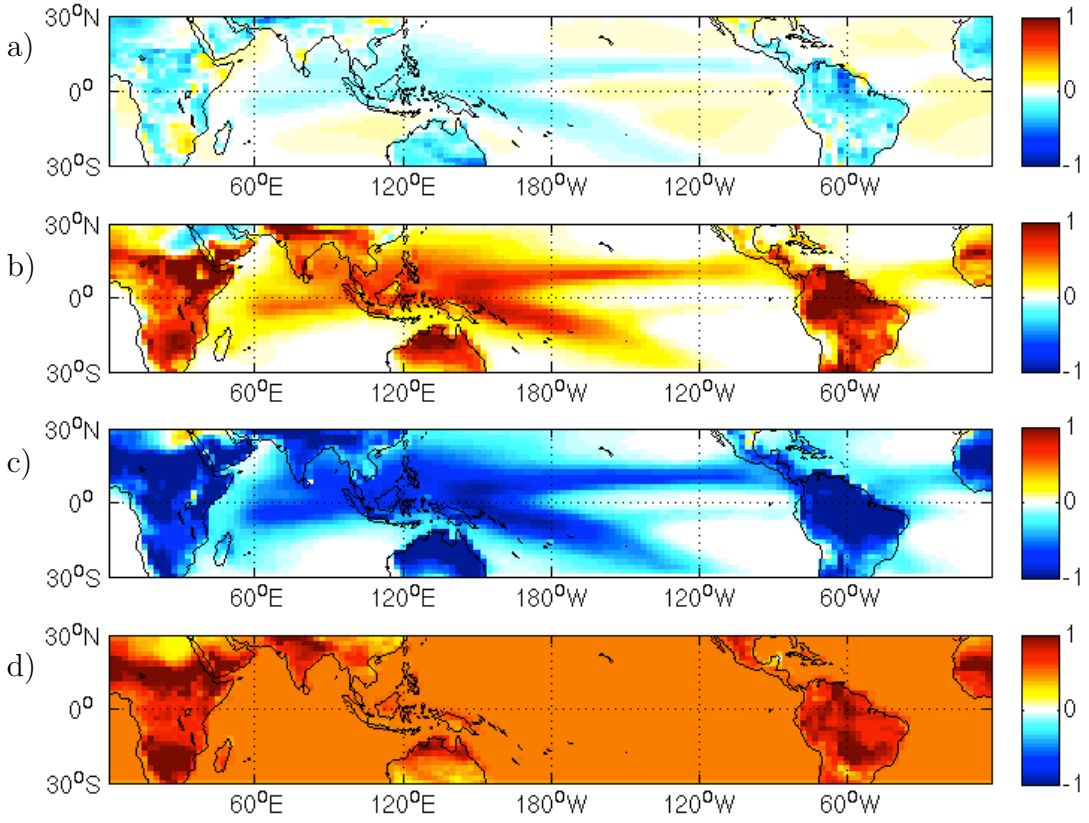


Figure 3.2: Same as figure 3.1 but for experiments a) E, b) F, c) G and d) U.

indicate that even when this feedback is artificially eliminated, high cloud amount is substantially less sensitive than expected from assumptions based on the control run.

For each month, we separate the tropical oceans into 4 classes according to monthly mean precipitation P, namely $P > 8$mm/day, $8 \geq P > 6$mm/day, $6 \geq P > 4$mm/day and 4mm/day $\geq P$. The threshold of 6mm/day corresponds to what is frequently taken as 'convective rainfall' (Sobel et al., 2002), though rare convective events may also have a monthly mean precipitation value less than 6mm/day. The tropical SSTs are then modified according to table 3.1, with the 8 experiments spanning a range of perturbations that modify the temperature contrast between convective and non-convective regions and tropical average SST (see figures 3.1 and 3.2). The parameters g_A and g_E are chosen such that the tropical average SST is not changed, whereby g_A is a multiplicative factor (modulating the amplitude of patterns)

and g_E is a constant offset. Note that the perturbations are sufficiently small so as not to invert spatial patterns. Also, the perturbations are not designed to test linearity or symmetric perturbation pairs, but to address the question of whether cloud amount changes follow a coherent pattern irrespective of the details of the perturbation.

3.2.3 Convective mass flux and high cloud amount

We establish the empirical relation between local (i.e., grid cell) convective mass flux m_c and high cloud amount for the monthly mean values. Figure 3.3(a) shows the joint distribution density, and the mean cloud amount, C(m_c), as a function of convective mass flux at 500 hPa, m_c, for the control calculation. Note that the relation is not compact, and cloud amount is skewed particularly for large convective mass fluxes as expected for bounded distributions. The lack of compactness is due to geographical differences in the spectra of events that lead to high cloud amount, namely: (i) local convection; (ii) non-convective clouds, and (iii) convective clouds without local convection due to advection from surrounding convective events.

We interpret changes in high cloud amount in terms of changes in convective mass flux distribution ($f(m_c)$, shown in Figure 3.3b for the control calculation) and changes in high cloud amount as a function of convective mass flux, $C(m_c)$. The total cloud amount is recovered by:

$$\langle C \rangle = \int f(m_c) \cdot C(m_c) \cdot \mathrm{d}m_c \tag{3.1}$$

but reconstruction of the geographical distribution of cloud amount based on $C(m_c)$ would give only an approximation. Changes in cloud amount between the control and perturbation calculation are decomposed:

$$\langle C \rangle' = \langle f' \cdot C \rangle + \langle f \cdot C' \rangle + \langle f' \cdot C' \rangle \tag{3.2}$$

EXP	$P < 4$	$4 < P < 6$	$6 < P < 8$	$P > 8$	$< T_s >'$	A_c'	$< m_c >'$	$< f'_{uni} \cdot C >$	$< f' \cdot C >$	$< f \cdot C' >$	$< f' \cdot C' >$
A	$SST \cdot g_A$	$SST \cdot g_A$	+1.00%	+2.00%	+0.03	−2.18	−4.60	−0.68	−1.21	+0.67	+0.02
B	—	—	+1.00%	+2.00%	+0.16	−1.74	−3.84	−0.57	−0.95	+0.59	0.00
C	+1.00%	+0.40%	—	—	+0.16	+0.79	+0.68	+0.10	+0.25	+0.01	0.00
D	−1.00%	−0.40%	—	—	−0.17	−0.91	−0.73	−0.11	−0.29	+0.09	0.00
E	$+1.00\% - g_E$	$+0.04\% - g_E$	$-g_E$	$-g_E$	−0.04	+1.17	+1.83	+0.26	+0.47	−0.21	+0.01
F	—	—	+1.50%	+3.50%	+0.29	−2.95	−7.03	−1.04	−1.74	+1.03	+0.02
G	—	−1.50%	−3.50%	−3.50%	−0.44	+4.35	+8.26	+1.16	+1.87	−1.43	−0.04
U	+0.50K	+0.50K	+0.50K	+0.50K	+0.56	−0.44	−2.53	−0.37	−0.43	+0.65	0.00

Table 3.1: Summary of the setup (left) and results (right) of the 8 perturbation experiments. Tropical SST perturbations are shown for the 4 regions: precipitation, P > 8 mm/day, $8 \geq P > 6$ mm/day, $6 \geq P > 4$mm/day and 4 mm/day $\geq P$. Also shown are the tropical mean anomalies in surface temperature T_s (K), convective area A_c(%), convective mass flux m_c (%), and the 4 decomposition terms of the high cloud amount anomalies: $f'_{uni} \cdot C$ (%), $f' \cdot C$ (%), $f \cdot C'$ (%) and $f' \cdot C'$ (%). See text for further details.

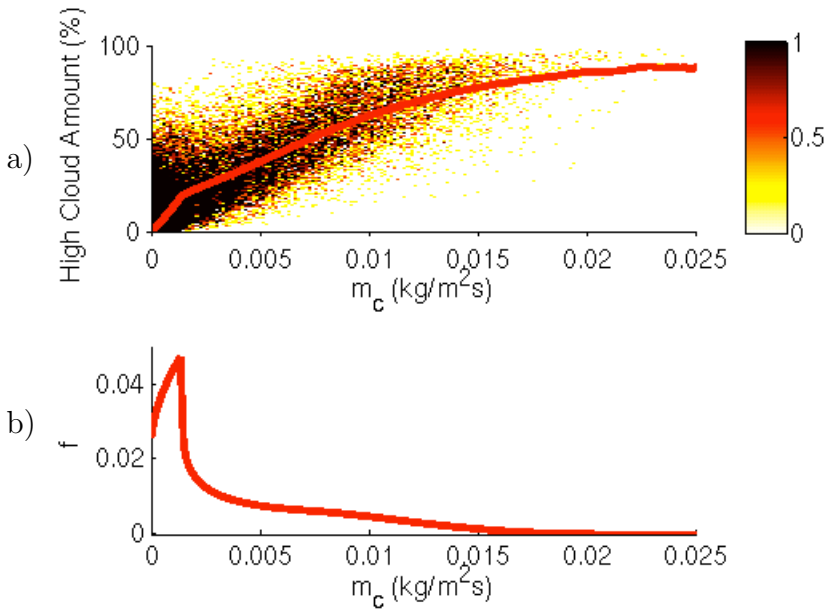


Figure 3.3: (a) Joint distribution density and mean, C(m_c) (solid red line), of the high cloud amount for the control calculation, as a function of 500hPa convective mass flux m_c, b) convective mass flux distribution f(m_c) for the control calculation. See text for further details.

$$\langle f_{uni} \cdot C \rangle \tag{3.3}$$

where the first term on the right hand side is the change due to the change in convective mass flux distribution that includes the non-linear relation between convective mass flux and cloud amount (Fig. 3.3a), the second term is the change in cloud amount due to a change in the relation between convective mass flux and cloud amount, and the last term is the correlated changes in convective mass flux distribution and cloud amount as a function of convective mass flux.

The term $\langle f' \cdot C \rangle$ is straightforward to interpret from the perspective of changes in the distribution of convection following the imposed changes in SSTs. However, there remains ambiguity because both a change in *mean* convective mass flux, and in the *distribution* function with constant mean convective mass flux can induce a change in $\langle f' \cdot C \rangle$. To resolve this ambiguity, we also calculate the change in cloud

amount that results if the change in convective mass flux (determined from the model outputs) were due to a spatially uniform fractional change in convective mass flux $k = \langle m_{c,exp} \rangle / \langle m_{c,ctl} \rangle$. The corresponding distribution function of convective mass flux is given by $f'_{uni} = f_{uni} - f$, with $f_{\rm uni}$ calculated using $m_{c,uni}(lon, lat, time) = m_{c,ctl}(\lambda, \theta, t) \cdot k$, and the expected cloud amount change by $\langle f'_{\rm uni} \cdot C(m_{c,ctl}) \rangle$. We show below that, for the experiments presented here, the cloud amount changes because the changes in the *mean* and *distribution* of convective mass flux have the same sign. This need not always be the case and is due to the fact that in our experiments there is a correlation between mean convective mass flux and fractional area coverage of convection.

Terms involving changes in the relation between convective mass flux and cloud amount, C', are more difficult to interpret and are discussed in Section 3.3.4.

Finally, we note that $C(m_c)$ and $f(m_c)$ show substantial seasonality and that a similar analysis can be done for the seasonal variability in high cloud amount. Hence, results depend on the base state and we therefore choose to study the problem with realistic SSTs rather than with an idealized SST distribution.

Figures 3.4 and 3.5 show the terms of the decomposition, and the terms for the scenario of a spatially uniform fractional change in convective mass flux, for all eight experiments. The curves are the integrals over convective mass flux, with integration starting at the maximum convective mass flux. Hence, the values at $m_c = 0$ are the total changes between each experiment and the control calculation. A summary of these four decomposition terms is given in table 3.1.

3.3 Results

We characterize the convective mass flux distribution and changes therein in terms of the tropical mean convective mass flux m_c and the fraction of the tropics that

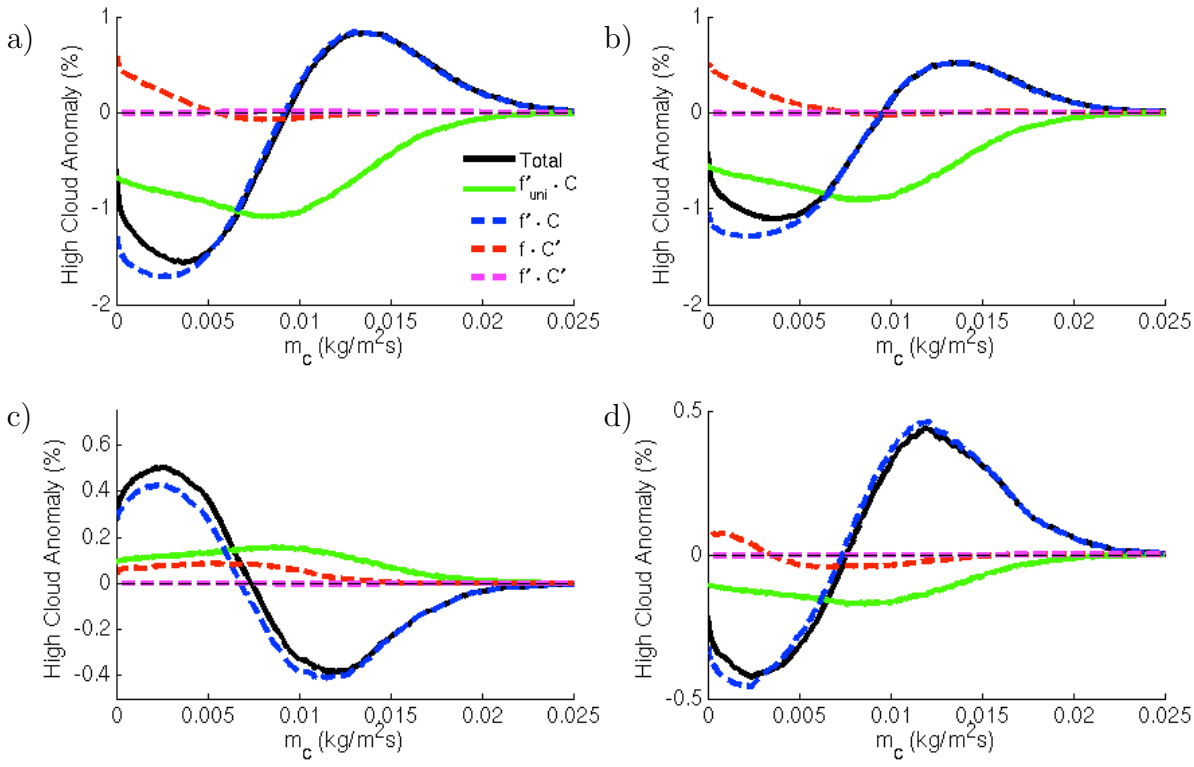


Figure 3.4: Total high cloud amount anomaly (black) for experiments a) A, b) B, c) C and d) D, integrated as m_c decreases such that the y-intercept gives the tropical mean high cloud anomaly. Also shown is $f'_{uni} \cdot C$ (green), which indicates the predicted high cloud anomaly that would result from a spatially uniform change in m_c, and the decomposition of the three contributors to high cloud amount anomaly: $f' \cdot C$ (blue dashed), $f \cdot C'$ (red dashed) and $f' \cdot C'$ (purple dashed). See text for further details.

contains 80% of the convective mass flux (A_c). Grid cells are sorted according to convective mass flux in each individual experiment and the results are not sensitive to the exact threshold value.

Figure 3.6 shows the results of all perturbation experiments in terms of the changes in tropical mean high cloud amount as a function of change in tropical SST (panel a), change in convective area fraction (panel b), and convective mass flux (panel c).

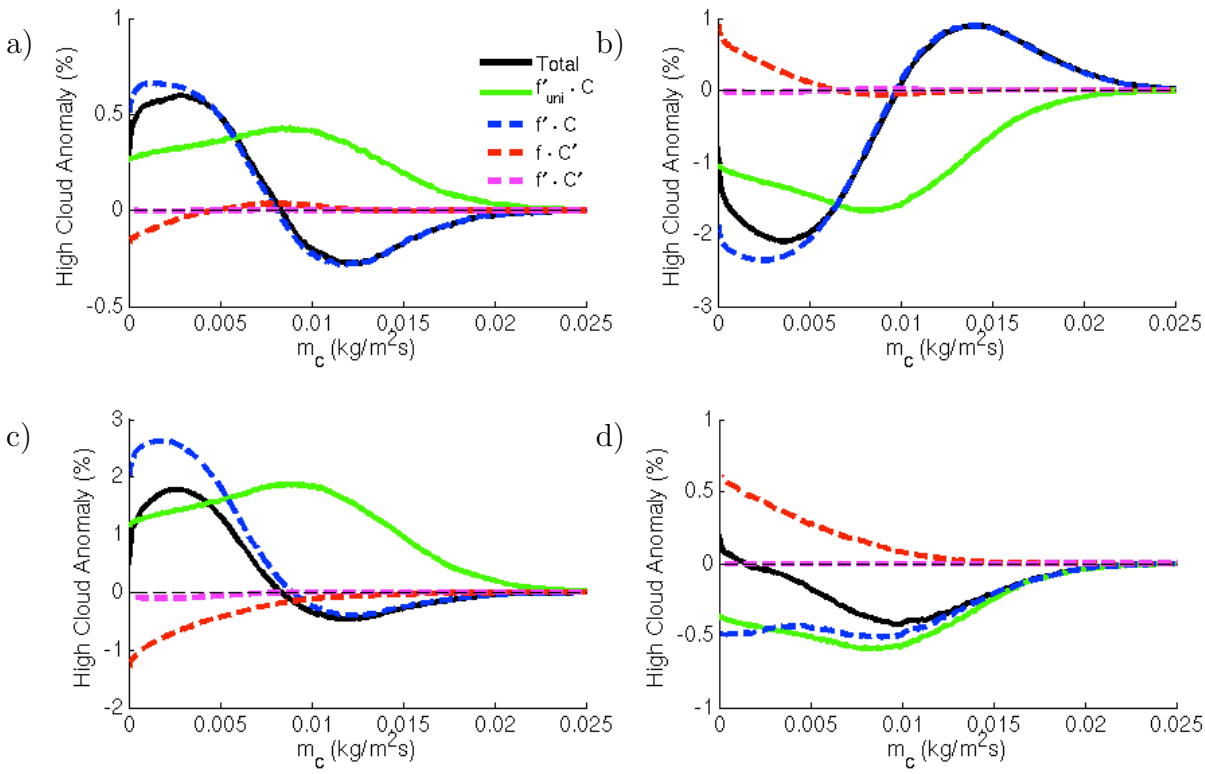


Figure 3.5: Same as figure 3.4 but for experiments a) E, b) F, c) G, and d) U.

.

3.3.1 Convective mass fluxes

While not directly displayed in Figure 3.6, the relation between tropical average convective mass flux and SST is dominated by the change in the regions of highest SSTs. All experiments that increase the temperature in convective regions show a decrease in convective mass flux, consistent with expectations (Held and Soden, 2006). Further, an increase/decrease in the temperature contrast between convective and non-convective regions leads to decrease/increase in the convective area fraction A_c. Figure 3.7 gives the A_c anomaly as a function of both tropical mean T_s and temperature gradient anomaly, where the temperature gradient is defined as the temperature within the region $(150 - 170°E$, $5°S - 5°N)$ minus that of the region $(240 - 260°E$, $5°S - 5°N)$, consistent with Larson and Hartmann (2003). A positive temperature gradient indicates the Western Equatorial Pacific is warmer than the Eastern Equato-

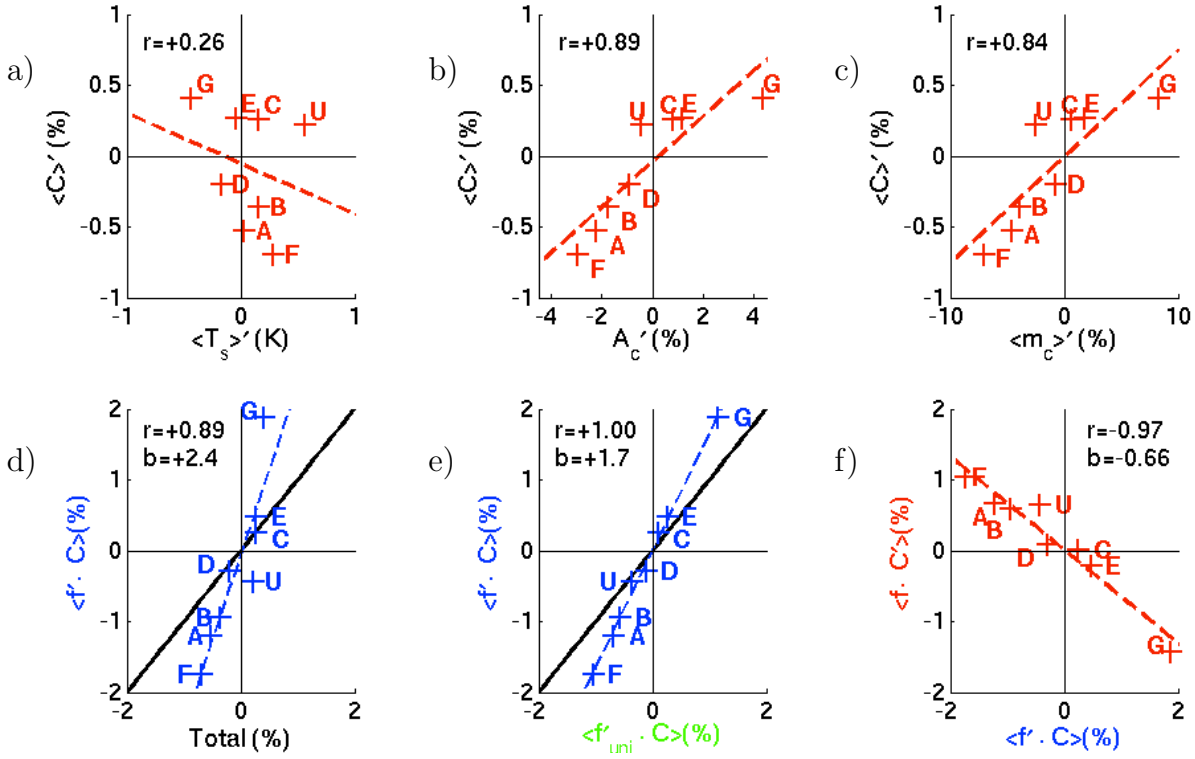


Figure 3.6: High cloud amount changes for each perturbation experiment as function of change in (a) tropical average surface temperature, (b) convective area fraction, and (c) tropical average convective mass flux. (d) $f' \cdot C$ against the model average high cloud change. (e) $f' \cdot C$ against the expectation for a uniform fractional change in convective mass flux. (f) The change in the relation between convective mass flux and cloud amount, $f \cdot C'$, against $f' \cdot C$. Colors in (d,e,f) as for terms in figure 3.4 and 3.5. Correlation coefficients, r, and linear regression slopes, b, are given for quantitative arguments.

rial Pacific, and a positive temperature gradient anomaly is indicative of an increase in the Western/Eastern Pacific (or convective/non-convective region) contrast. In our experiments the temperature change in the convective regions and the contrast between convective and non-convective regions are correlated except for the uniform warming experiment U.

3.3.2 Convective area and surface temperature gradients

To better understand why an increased temperature contrast results in a decreased A_c, additional analysis is performed and the results for experiment A are given. The

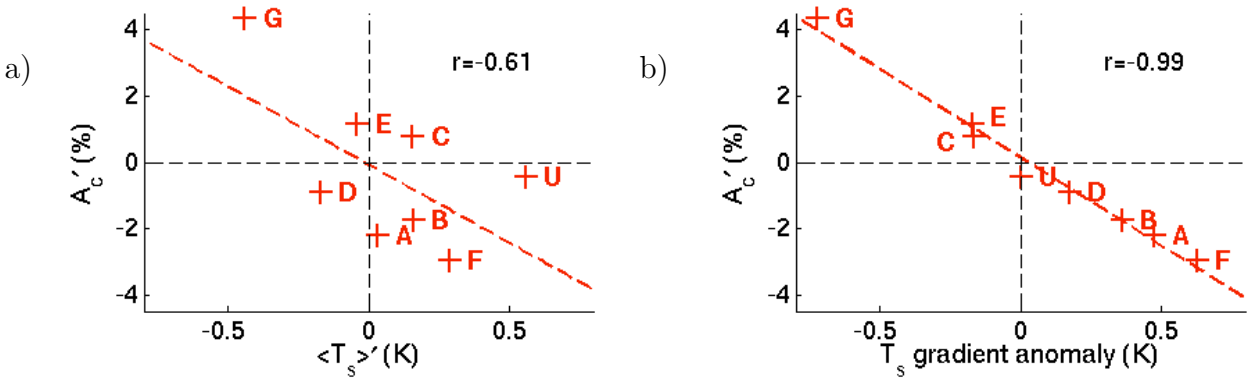


Figure 3.7: Convective area change (%) for each perturbation experiment as a function of change in a) tropical average T_s anomaly (K) (correlation coefficient r=-0.61) and b) zonal T_s gradient anomaly (K) (r=-0.99).

temperature perturbation for experiment A (see figure 3.8a) is an increase in the convective region SSTs and a decrease in the non-convective region SSTs. The black contour line represents a surface temperature anomaly of zero. Whilst $\langle T_s \rangle$ remains roughly constant, the temperature gradient between the eastern and western Pacific Ocean has increased substantially. (NB: The small change in $\langle T_s \rangle$ of +0.03K is due to changes over land where temperatures are not prescribed.)

Evaporation is proportional to i) the mean horizontal wind at the lowest model level, and ii) the difference in specific humidity between the lowest model level and the surface (saturation value at T_s). An increase in either T_s or wind will therefore increase the evaporation rate, assuming there is a moisture source. As shown in figure 3.8b, most regions inside the zero temperature anomaly line (i.e. grid cells with positive temperature anomalies) show an increase in evaporation. This is not true, however, of specific humidity at the lowest model level, which actually decreases in several regions inside the zero temperature contour line (figure 3.8c). This can be explained by the process of advection. Whilst the increased T_s increases evaporation, the change in T_s gradient also induces winds that advect the moisture away at a large enough rate that the local specific humidity decreases. This strong advection can be seen in the 900mb convergence field, shown in figure 3.9a. Whilst there is

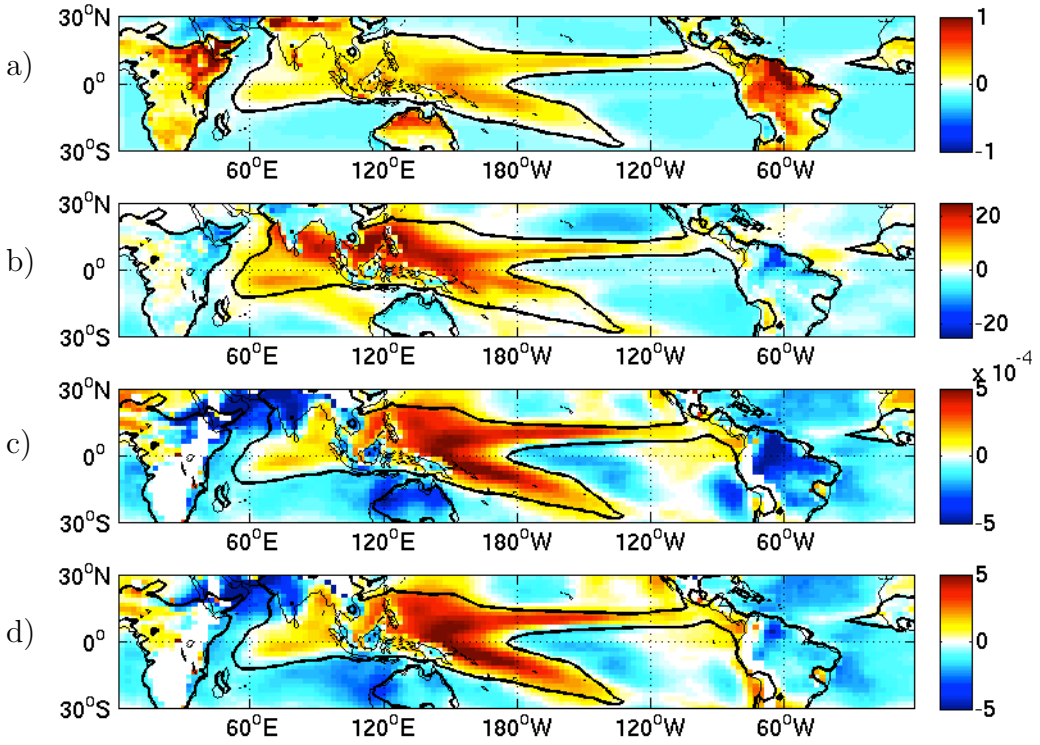


Figure 3.8: Experiment A changes for a) surface temperature (K), b) evaporation ($kg/m^2/s$), c) specific humidity (kg/kg) and d) moist static entropy at 900mb ($J/kg/K$). Solid black contour line indicates where the temperature difference between experiment A and the control run is zero.

convergence into certain regions, such as the South Pacific Convergence Zone (SPCZ) and in the western Pacific north of the Equator, there are also regions that exhibit strong divergence. Areas that have a decrease in specific humidity coincide with regions of divergence, such as over the maritime continent and around the zero T_s anomaly (solid black line) in the Indian Ocean.

Due to the complex nature of convective processes, it is difficult to determine where or when convection will occur. There are, however, proxies which indicate a high probability of a convective event occurring, one of which is the moist static entropy (MSE). In the control run, MSE is largest in the west-Pacific convective regions (as expected), and the change in MSE in experiment A is shown in figure 3.8d. The MSE increases in most regions of increased T_s, with the exception of some areas

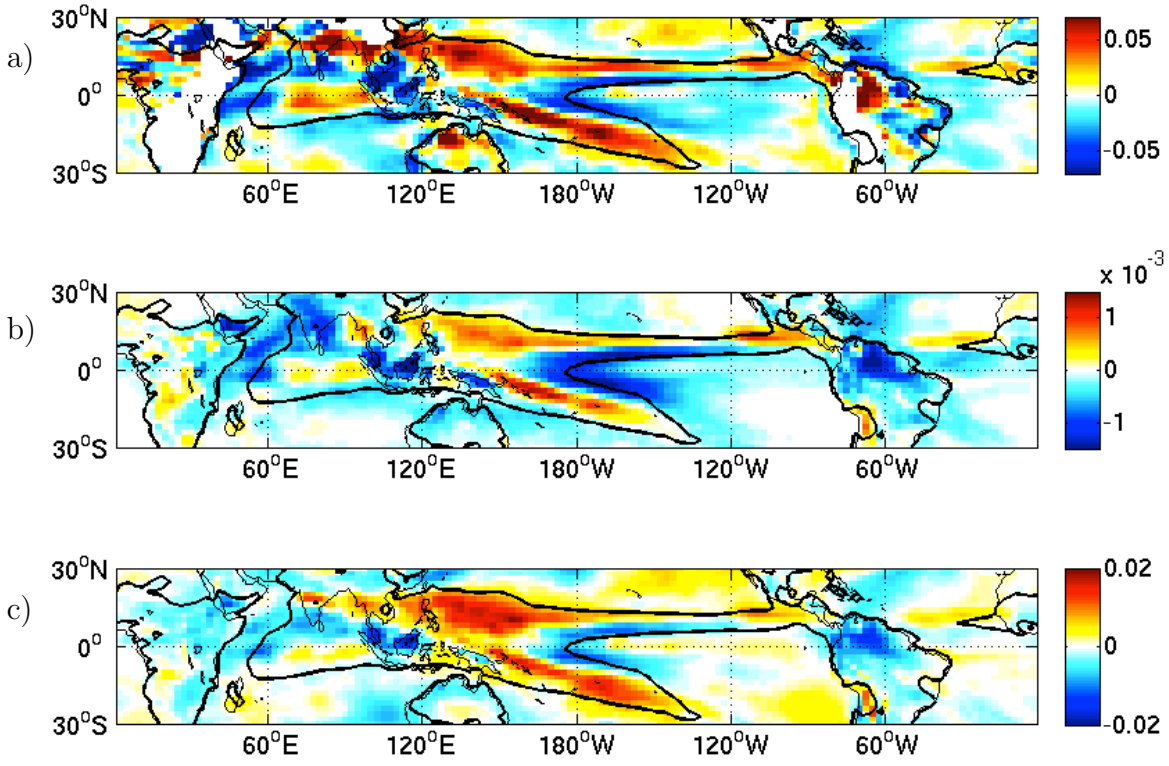


Figure 3.9: Experiment A changes for a) convergence at 900mb (s^{-1}) b) $-1\times$Omega at 500mb (pa/s), c) convective mass flux ($kg/m^2/s$). Solid black contour line indicates where the temperature difference between experiment A and the control run is zero.

along the zero temperature contour line (e.g. in the Indian Ocean). MSE is a function of both temperature and specific humidity, therefore the decrease in specific humidity in the Indian ocean overrides the increase in temperature, and causes a decrease in MSE. It is critical to note that we have only increased the SST in 'convective' regions (i.e. where precipitation exceeds 6mm/day), and yet in some areas this increased temperature has actually decreased the likelihood of convection.

The convective mass (m_c) flux at 500mb is shown in figure 3.9b. There is an increase in m_c in the SPCZ and north of the equator in the West Pacific. There is a significant area however, within this zero T_s anomaly line that exhibits a decrease in m_c. Figure 3.9c is simply the 500mb Omega, multiplied by -1, and is spatially very similar to m_c but with an additional positive homogenous offset.

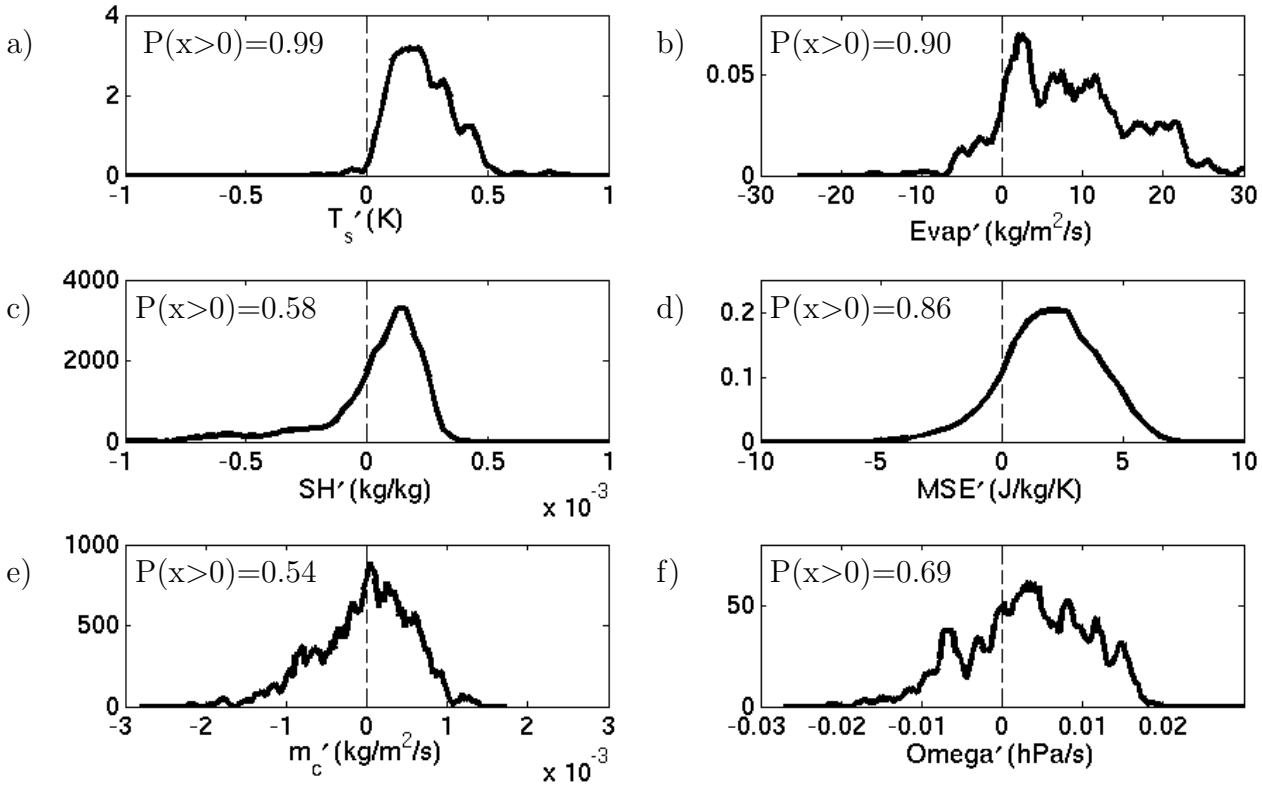


Figure 3.10: PDF of experiment A changes within the convective region (i.e. where precipitation exceeds 6mm/day), for a) surface temperature (K) b) evaporation ($kg/m^2/s$), c) specific humidity (kg/kg), d) moist static entropy at 900mb ($J/kg/K$), e) convective mass flux at 500mb ($kg/m^2/s$), and f) $-1\times$Omega (pa/s). Also shown is the probability of the anomaly to be positive (i.e. the fractional area that has a positive anomaly).

A more quantitative analysis of these regional map results is given in figure 3.10, where PDFs of the anomalies in temperature, evaporation, specific humidity, MSE, m_c(500mb) and -1×Omega(500mb) are shown. The PDFs only consider anomalies within the zero temperature anomaly line (i.e. the solid black contour line in figures 3.8 and 3.9). Also indicated on each panel of the figure is the probability of a grid cell have a positive anomaly. For example, 99% of the region has an increase in temperature, but only 90% has an increase in evaporation, as there are limited water sources over the Asian continent. Due to the strong divergence of moisture, however, only 58% of the region sees as increase in specific humidity and this affects the MSE

(as discussed above), which only increases in 86% of the region. Finally, we see that m_c increases in 54% of the region, whilst -1×Omega increases in 69%.

The important result here is that although 99% of the convective region increases in temperature, the convective mass flux only increases in 54% of the region. The increased temperature gradient in experiment A serves to increase the convergence of moisture into the maximum SST region, and contracts the region of high MSE and convection. So it is not the absolute value of T_s that is relevant for m_c but rather the spatial distribution T_s, which is quantified by A_c.

Neelin (2003) proposed a mechanism to explain why a region of increased SSTs causes a decrease in convective area. Their study focused on both doubled-CO_2 scenarios and El Nino events, with the use of an intermediate climate model, and found that the tropospheric temperature warmed in both cases. Given that an updraft occurs when the air in the boundary layer is warmer than the ambient sounding in the free troposphere, when the troposphere is warmed, boundary layer air must be moister for convection to occur. They term this the "upped-ante mechanism". In the middle of the convergence zone, where there are large amounts of moisture, this increased ante is not a barrier and convection continues and even tends to be enhanced by the increased moisture in the converging air. However, on certain margins of the convection zone where there is a strong low level flow coming from a climatologically non-precipitation region, the increased ante can be a significant barrier. This inflow of less moist air into a region that ought to have a higher boundary layer moisture to convect produces a balance where precipitation is reduced and there is a reduction in large-scale rising motion.

The 'upped ante mechanism' can indeed explain the physical processes of experiment A, where the convective SSTs and tropospheric temperatures increase, leading to an increased barrier to convection and a decrease in the convective area.

In experiment D, on the other hand, the convective SSTs are held constant and the non-convective SSTs are decreased, leading to an overall decrease in tropospheric temperature. According to the 'upped ante mechanism' this would decrease the barrier to convection and increase the convective area, however there is also advection of air from the non-convective to convective regions. The specific humidity in non-convective regions will have decreased, due to the decrease in SST, which results in an effective drying of the convective regions. This drying effect will presumably act to decrease the convective area, and compensates for the decreased barrier for convection. The net effect of these two compensating mechanisms is an overall decrease in convective area.

3.3.3 High cloud amount

Figure 3.6(a-c) shows the change in high cloud amount has some relation with the change in average SST, which is determined by the p-test statistic to be statistically insignificant, but that the associations with convective area fraction A_c and convective mass flux (m_c) are much stronger. The strong correlation with A_c (panel b) may be the consequence of the non-linear relation between average cloud amount and convective mass flux, $C(m_c)$. A focusing of convective mass flux (i.e., a decrease in A_c) leads to an increase in the distribution function f at high convective mass fluxes and a decrease at low mass fluxes. The shape of $C(m_c)$ (recall Figure 3.3) then implies a decrease of the tropical average cloud amount even if the tropical average convective mass flux ($\int f \cdot m_c \mathrm{d}m_c$) remains constant. Similarly, the strong correlation with tropical mean mass flux changes (panel c) may be expected on the basis that deep convection is a sufficient (but not necessary) condition for high clouds. However, since A_c' and $\langle m_c \rangle'$ are correlated in our experiments, attribution of high cloud amount changes cannot be established based on Figures 3.6(a-c), and we must discuss the decomposition described in Section 3.2.3.

3.3.4 Compensation in non-convective regions

Figure 3.6(d) shows that $\langle f' \cdot C \rangle$ overestimates the changes in high cloud amount by approximately a factor 2 (exceptions, e.g., uniform warming U, noted). Similarly, $\langle f' \cdot C \rangle$ is larger than expected from the spatially uniform fractional change in convective mass flux again by about a factor 2. This implies that the change in mean convective mass flux, and the change in spatial distribution, each contribute similarly to the high cloud amount change. Finally, Figure 3.6(f) shows that $\langle f' \cdot C \rangle$ and $\langle f \cdot C' \rangle$ are strongly anti-correlated with a ratio of about -1/2. The cross term, $\langle f' \cdot C' \rangle$ is much smaller in all experiments. Hence, changes in C (i.e., C') render total high cloud amount less sensitive than expected from holding of C constant, i.e., from $\langle f' \cdot C \rangle$.

A detailed inspection of $\langle f \cdot C' \rangle$ of all experiments, and of the maps of high cloud amount changes, shows that the average change $\langle f \cdot C' \rangle$ is strongly influenced by the contribution at low convective mass fluxes. This result in turn is linked to the change in tropical average convective mass flux: increasing/decreasing tropical average convective mass flux leads to a decrease/increase in high cloud amount in non-convective regions.

We find that in non-convective regions relative humidity increases/decreases in response to a decrease/increase in tropical average convective mass flux, and that the change in relative humidity is primarily due to a change in specific humidity rather than temperature. This is demonstrated by closer analysis of the South Eastern Pacific ($255 - 290°E$, $20 - 30°S$), where the control run climatological values of m_c are small (as shown in figure 3.11a)) and subsidence dominates (figure 3.11b). The climatological values of cloud fraction, temperature, specific and relative humidity are also given in figure 3.11 for reference. In experiment A, where there is a 4.6% decrease in tropical convective mass flux, this non-convective region has a 10% decrease in subsidence, a 7% increase in specific and relative humidity, and a 20% increase in cloud fraction (NB: anomalies are given as a percentage of the control run values at

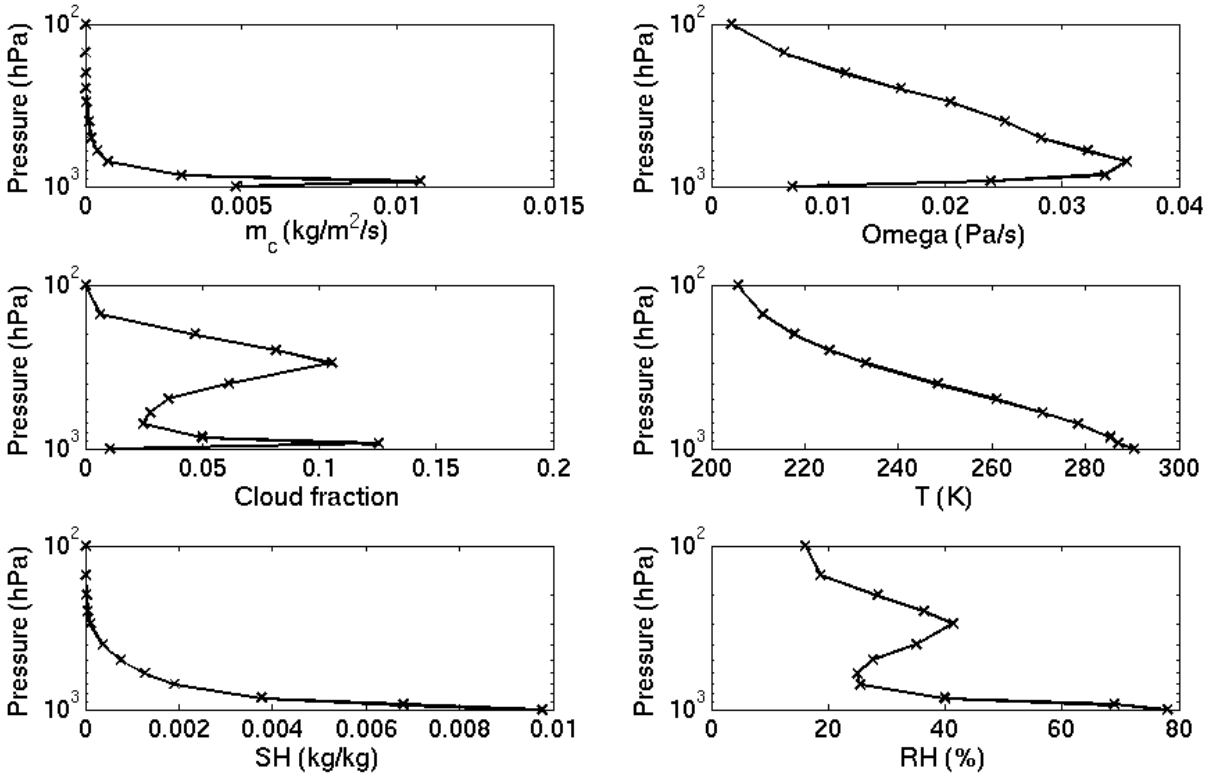


Figure 3.11: Control run values for a) m_c ($kg/m^2/s$), b) omega (hPa/s), c) cloud fraction, d) temperature (K), e) specific humidity (kg/kg), and f) relative humidity (%) averaged over the region ($255 - 290°E$, $20 - 30°S$).

the 200hPa level). The m_c anomalies are only given for the lower troposphere as the control m_c values above 500hPa approach zero and thus give percentage anomalies that are not meaningful. The increase in 200hPa relative humidity is primarily due to changes in specific humidity as the temperature anomalies are of order 0.1%. This increase in relative humidity and cloud fraction then compensates for the convective mass flux induced decrease in high cloud amount, which arises from the $\langle f \cdot C' \rangle$ term.

The anomalies for experiment G, which has an increase in tropical convective mass flux of 8.3%, are shown in figure 3.13. As the tropical convective mass flux increases, there is a 30% increase in subsidence, a 20% decrease in specific and relative humidity, and a 40% decrease in cloud fraction. This is a mirror image response to that seen in experiment A, and again acts to compensate the high cloud amount anomalies which arise from changes in convective mass flux.

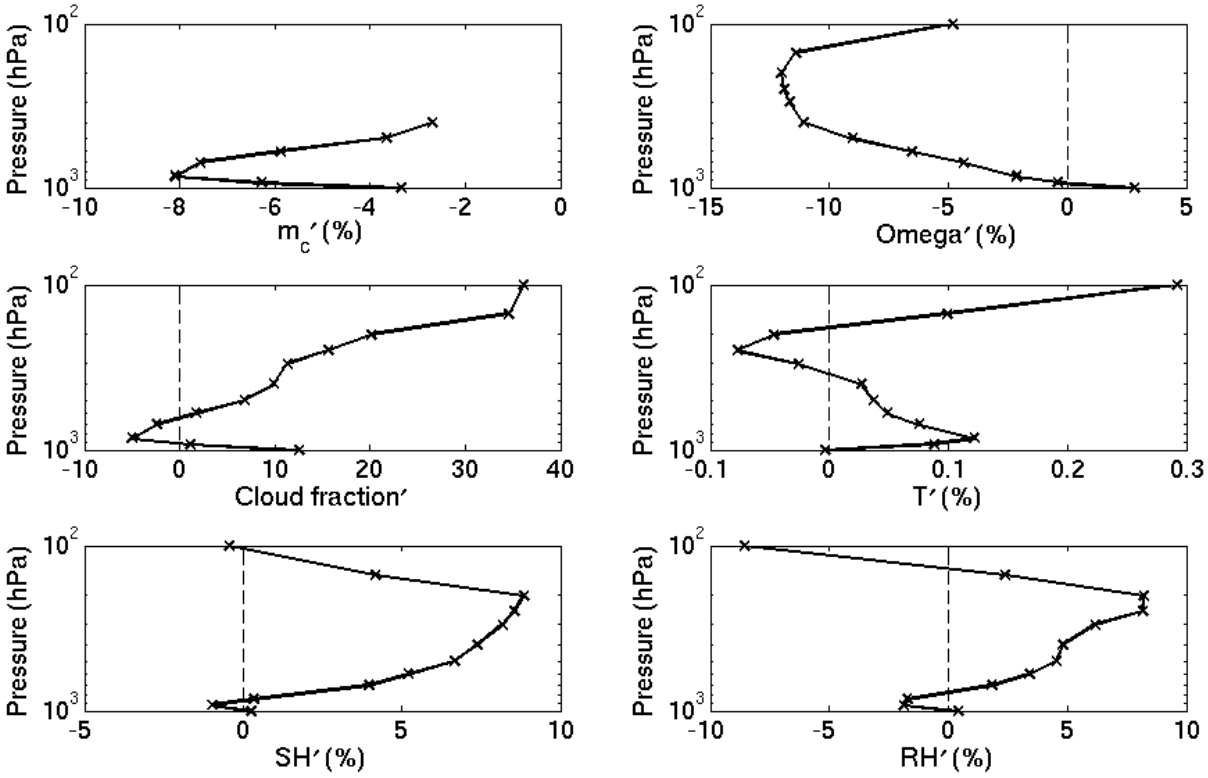


Figure 3.12: Experiment A changes for a) m_c, b) omega, c) cloud fraction, d) temperature, e) specific humidity, and f) relative humidity averaged over the region $(255 - 290°E,\ 20 - 30°S)$. Changes are given as a percentage change in the base state values (see figure 3.11).

Whilst the change in relative humidity explains the change in cloud amount, the mechanistic link to the tropical average convective mass flux change is non-trivial. While beyond the scope of this paper, we note that the change in turnover timescale associated with the change in average convective mass flux alone cannot explain the change in specific humidity. Rather, we hypothesize that the moistening is a consequence of the change in subsidence tendency relative to horizontal mixing time scale.

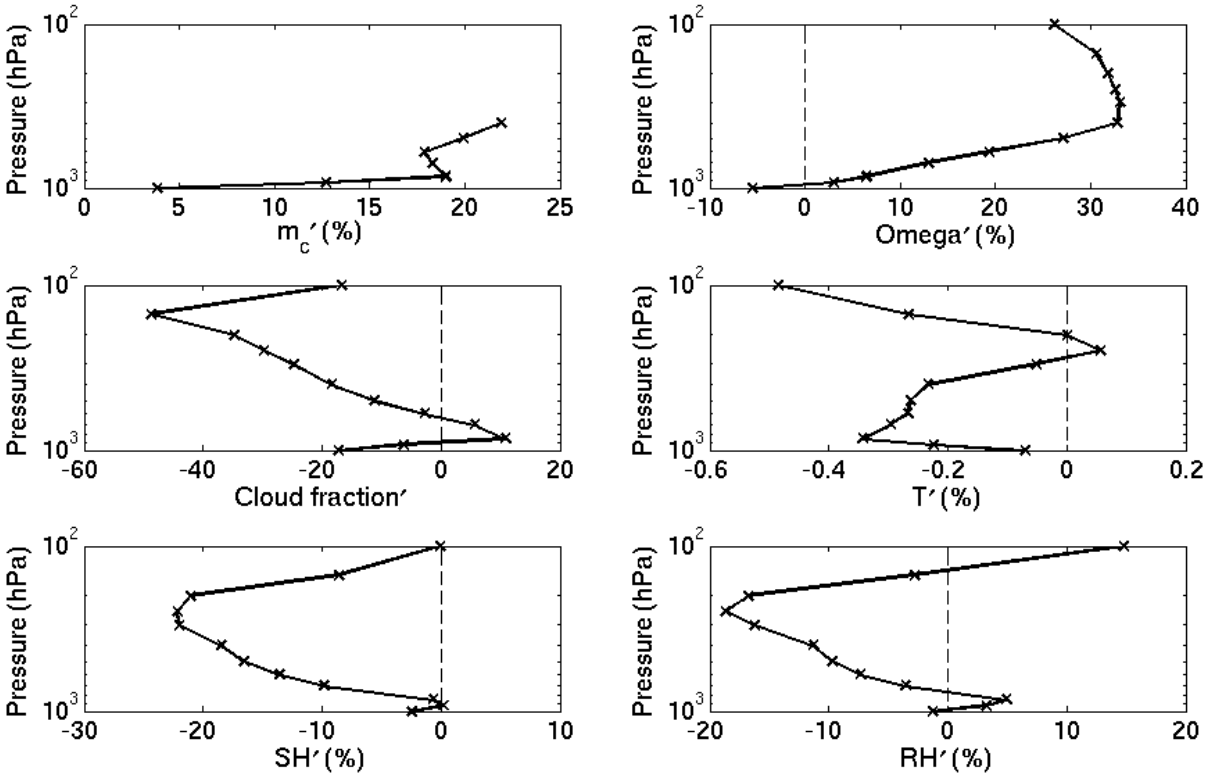


Figure 3.13: Same as figure 3.12 but for experiment G.

3.4 Additional Results

The following results, which have not been published, provide a brief overview of how precipitation, liquid/ice water paths, low cloud amount and TOA radiative flux respond to perturbations in convective mass flux.

3.4.1 Precipitation Anomalies

Global mean precipitation is constrained by the surface energy budget (Held and Soden, 2006). An increase in surface temperature increases the energy available for evaporation/latent heating, thus the tropical mean precipitation anomaly is strongly correlated with the tropical mean surface temperature anomaly (r=+0.95, see figure 3.14). These results are in agreement with predictions from Held and Soden (2006), who state a 2% increase in precipitation per degree of surface temperature warming.

Also shown in figure 3.14 are the weaker correlations of the precipitation anomaly against $A_c\prime$ (r=-0.42) and $\langle m_c \rangle\prime$ (r=-0.56).

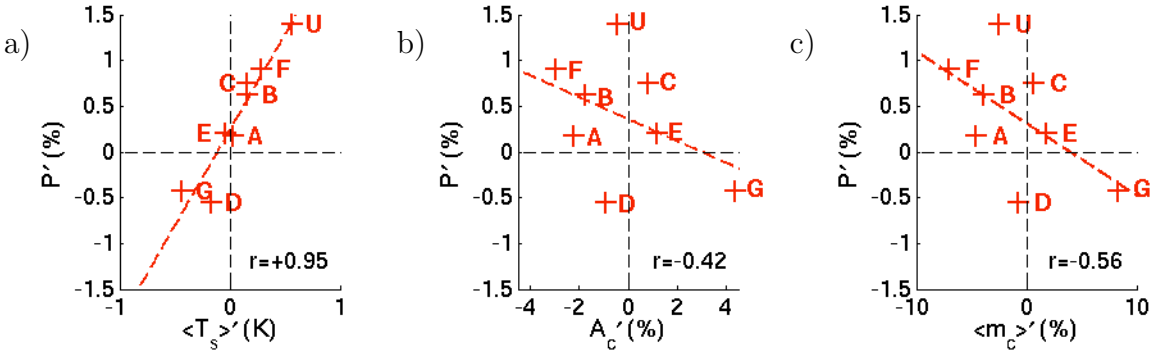


Figure 3.14: Total precipitation changes (%) for each perturbation experiment as a function of change in (a) tropical average surface temperature (correlation coefficient, r=+0.95), (b) convective area fraction (r=-0.42) and (c) tropical average convective mass flux (r=-0.56).

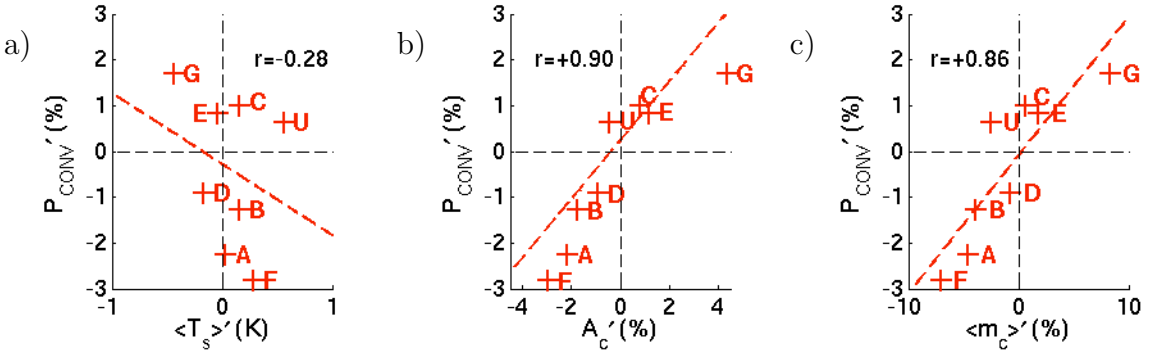


Figure 3.15: Convective precipitation changes (%) for each perturbation experiment as a function of change in (a) tropical average surface temperature (correlation coefficient, r=-0.28), (b) convective area fraction (r=+0.90) and (c) tropical average convective mass flux (r=+0.86).

Total precipitation can be decomposed into two components: convective and stratiform. Convective precipitation is the dominant term and accounts for 82% of the total precipitation in the tropics. Figure 3.15 shows the linear regression of the convective precipitation anomaly against $\langle T_s \rangle\prime$ (r=-0.28), $A_c\prime$ (r=+0.90) and $\langle m_c \rangle\prime$ (r=+0.86). Note that a certain fractional change in $\langle m_c \rangle$ results in a fractional change of convective precipitation roughly one third the size. This is due to changes in the boundary

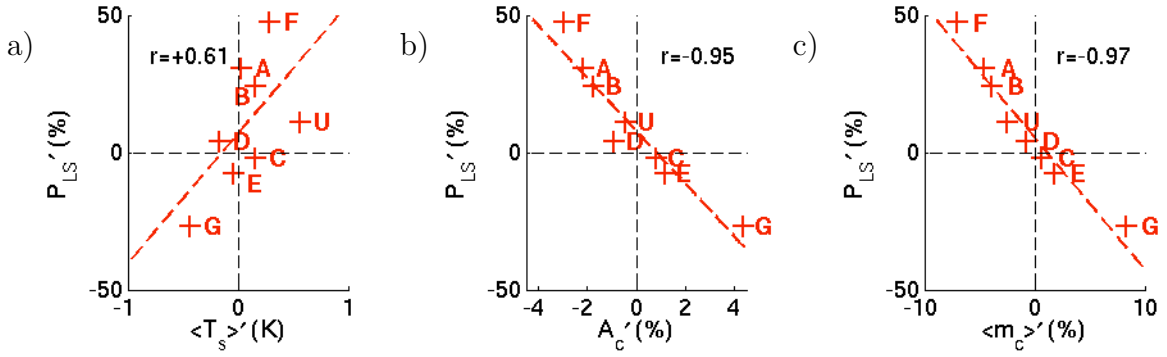


Figure 3.16: Stratiform precipitation changes (%) for each perturbation experiment as a function of change in (a) tropical average surface temperature (correlation coefficient, r=+0.61), (b) convective area fraction (r=-0.95) and (c) tropical average convective mass flux (r=-0.97).

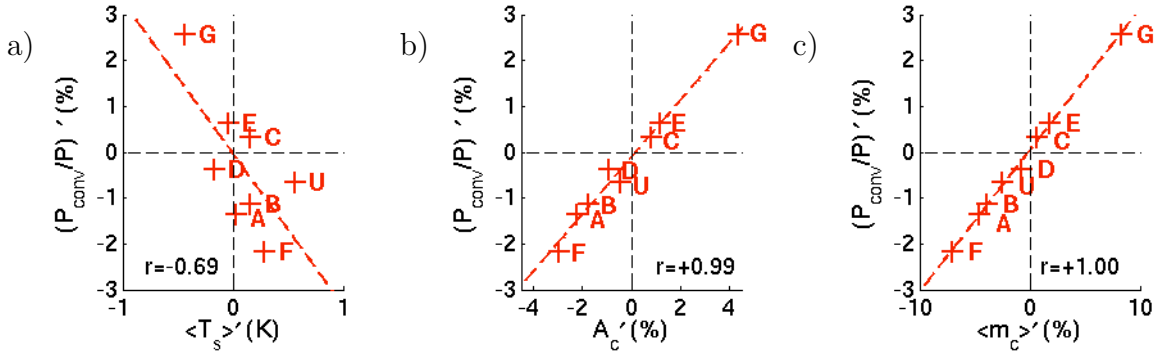


Figure 3.17: Changes in the percent of total rainfall that is defined as 'convective', as a function of change in a) tropical average surface temperature (correlation coefficient, r=-0.69), (b) convective area fraction (r=+0.99) and (c) tropical average convective mass flux (r=+1.00). Positive values indicate an increase in the percent of rainfall that is convective, relative to the base state percentage of 82%. .

layer specific humidity, which is a function of both local T_s but also surface winds. For example, experiment A has a decrease in A_c and $\langle m_c \rangle$, but the convective region has an increase in specific humidity, which counteracts these decreases to give a smaller than expected decrease in convective precipitation. The stratiform precipitation anomaly is shown in figure 3.17, and has correlation coefficients of r=+0.61, r=-0.95, and r=-0.97 when respectively linearly regressed against $\langle T_s \rangle'$, A_c' and $\langle m_c \rangle'$. The percentage anomalies of stratiform precipitation are large, however a 30% increase for experiment A is actually only an increase of order 0.1mm/day.

Whilst the total precipitation anomaly is most strong correlated with $\langle T_s \rangle \prime$, the individual components are clearly more strongly correlated with $A_c \prime$ and $\langle m_c \rangle \prime$, and are actually anti-correlated with one another. This anti correlation of convective and stratiform precipitation results in changes to the partitioning of precipitation. In the base state, convective precipitation accounts for 82% of the total precipitation, however as T_s increases, this percentage decreases with a correlation coefficient of r=-0.69. In other words, the fraction of the precipitation that is stratiform increases as the surface warms. As the convective area and convective mass flux increase, however, the convective precipitation accounts for a larger percentage of the total, with respective correlation coefficients of +0.99 and+1.00. These results indicate that whilst the tropical precipitation is constrained by the surface energy budget, the regional precipitation responses are determined by local changes in convective area and convective mass flux.

3.4.2 Liquid and Ice Water Paths

Whilst the majority of this work focuses on high cloud amount, the liquid (LWP) and ice water paths (IWP) are also important as they determine the clouds affect on the TOA energy balance. In this section we examine the dependence of LWP and IWP on tropical mean surface temperature ($\langle T_s \rangle$), convective area (A_c) and convective mass flux (m_c).

As with the high cloud amount analysis, we compute the joint distribution density of IWP and LWP against m_c at 500hPa (shown in figure 3.18). This joint distribution is calculated from the values of IWP/LWP and m_c in each individual grid cell over the 30 year control run. It is immediately obvious that the relationship between IWP/LWP and m_c is nonlinear, as for any given m_c value there is a large range of IWP/LWP values that could occur. In order to understand these plots and the

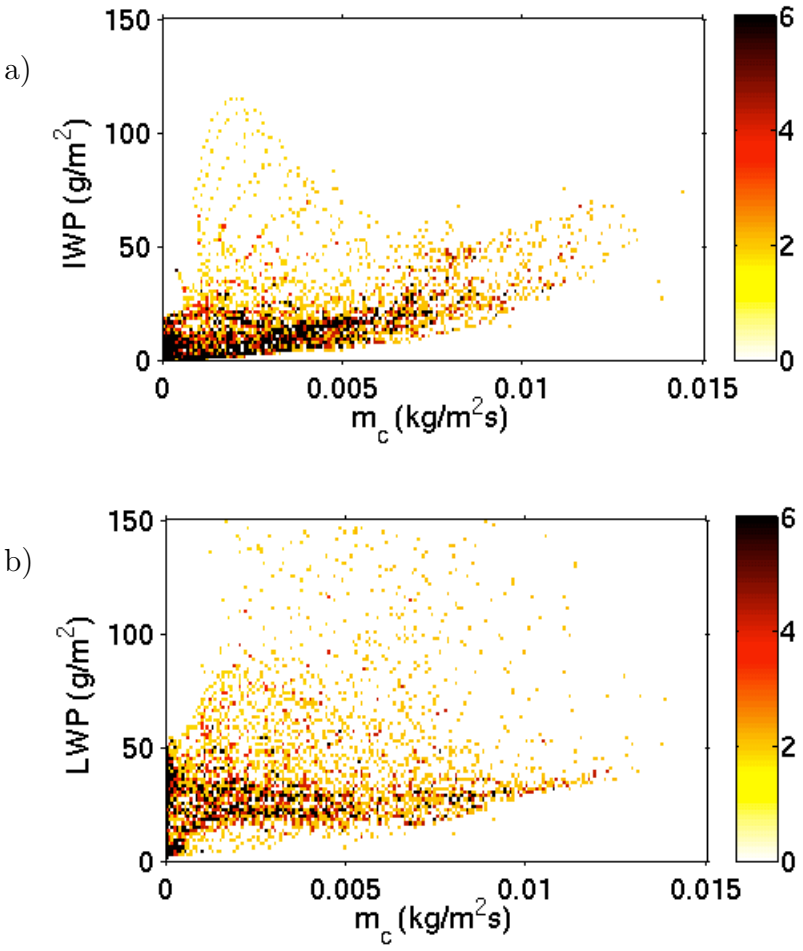


Figure 3.18: Joint distribution density for a) IWP (g/m^2) and b) LWP (g/m^2) against m_c (kg/m^2/s).

low correlation coefficients of +0.46 and +0.22, for IWP and LWP respectively, we examine the equations that govern a grid cell's liquid and ice water amount.

$$\frac{\partial q_{l,i}}{\partial t} = A_{l,i} + C_{l,i} + BL_{l,i} + S - E - G_p - \frac{1}{\rho}\frac{\partial}{\partial z}(\rho\overline{w'l'})_{entr} \tag{3.4}$$

The rate of change of the liquid/ice mixing ratio ($q_{l,i}$) is given by equation 3.4 (Tiedtke, 1993). Here, $A_{l,i}$ represents transport of liquid/ice through the boundaries of the grid volume, $C_{l,i}$ and $BL_{l,i}$ are the sources of cloud liquid/ice from convection and boundary-layer turbulence, respectively, S is the condensation/sublimation rate, E is the rate of evaporation of cloud liquid/ice, G_p is the rate of generation of precipitation

by conversion of cloud droplets into raindrops and deposition of cloud ice, and the last term is the flux divergence due to entrainment processes at the top of stratocumulus clouds. Equation 3.4 makes the usual assumption that clouds encountered at a model level extend vertically over the whole model layer depth.

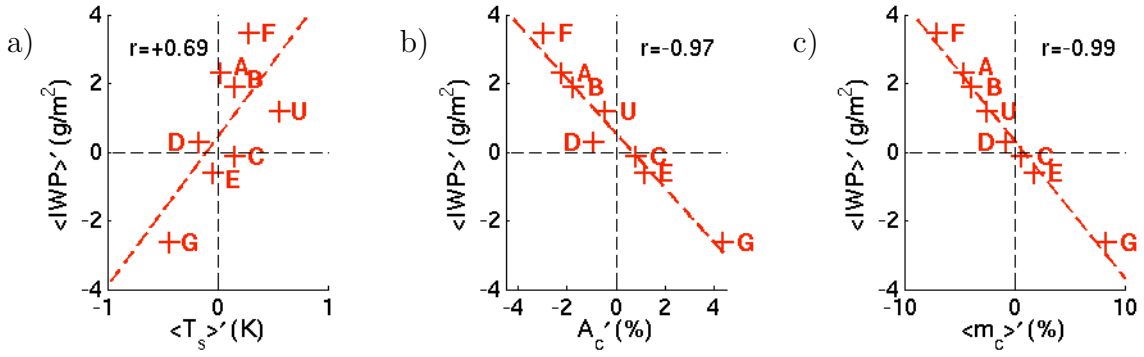


Figure 3.19: Ice water path changes (g/m^2) for each perturbation experiment as a function of change in (a) tropical average surface temperature (correlation coefficient, r=+0.69), (b) convective area fraction (r=-0.97) and (c) tropical average convective mass flux (r=-0.99).

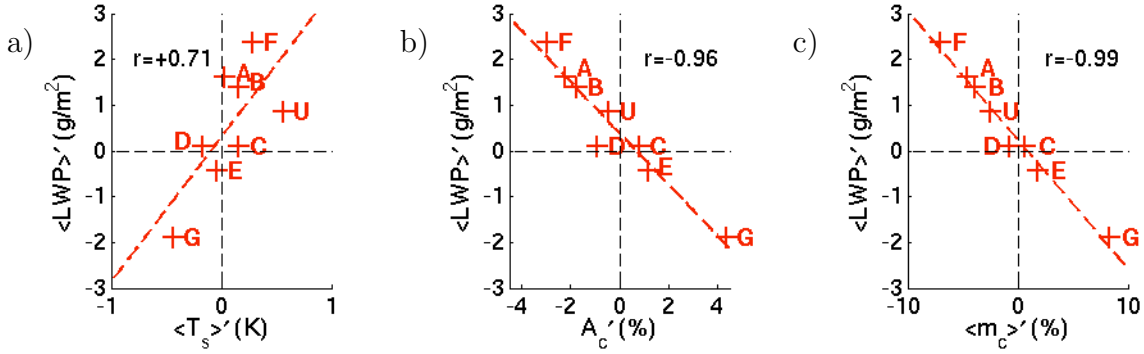


Figure 3.20: Liquid water path changes (g/m^2) for each perturbation experiment as a function of change in (a) tropical average surface temperature (correlation coefficient, r=+0.71), (b) convective area fraction (r=-0.96) and (c) tropical average convective mass flux (r=-0.99).

Unfortunately, model output does not permit analysis of these individual terms, however it is clear that the liquid/ice mixing ratio is a summation of many terms and results in IWP/LWPs that are highly nonlinear with respect to the convective mass flux. Given the low correlation between IWP/LWP and m_c one might also expect

there to be a low correlation between the tropical mean anomalies of these variables, however this is not the case. As shown in figures 3.20 and 3.19, there are correlations between IWP/LWP anomalies and $\langle T_s \rangle'$ of roughly +0.7, and correlations larger than +0.96 when IWP/LWP anomalies are regressed against A_c' and $\langle m_c \rangle'$.

3.4.3 Low Clouds

In contrast to the compensating radiative forcing of high clouds (i.e. LW and SW roughly cancel), low clouds primarily reflect shortwave radiation and have little effect on long wave radiation. Roughly 80% of the tropics is covered with low-level cumulus clouds (Bony et al., 2004), which combined with the strong negative cloud radiative forcing, results in low-level clouds being the largest contribution to the net energy balance of the Earth (Hartmann and Michelsen, 1993). Given the sensitivity of clouds to changes in surface temperature and/or thermodynamic structure of the atmosphere, there is a large degree of uncertainty around both the magnitude and sign of low cloud feedback.

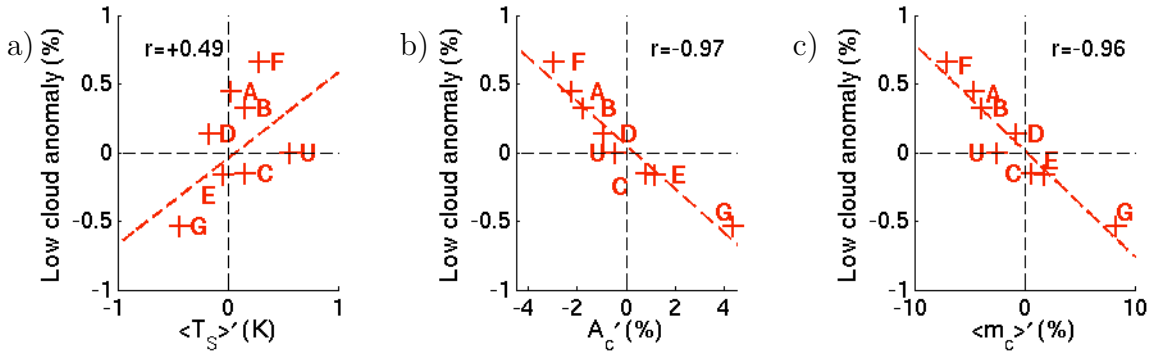


Figure 3.21: Low cloud amount changes (g/m^2) for each perturbation experiment as a function of change in (a) tropical average surface temperature (correlation coefficient, r=+0.49), (b) convective area fraction (r=-0.97) and (c) tropical average convective mass flux (r=-0.96).

The results from this study indicate a positive feedback between low cloud amount and surface temperature (r=+0.49, see figure 3.21). One should be cautious of this

result, however, as GFDL's AM2 model has been shown to simulate a correlation between omega and total cloud amount that is disagreement with observations (Clement et al., 2009). Also shown in figure 3.21 is the linear regression of low cloud amount anomaly against both $A_c\prime$ (r=-0.97) and $\langle m_c \rangle\prime$ (r=-0.99). Comparison against high cloud anomaly results in figure 3.6 indicate that there is a strong anti-correlation between high and low cloud anomalies, though explaining the physical mechanism responsible is beyond the scope of this thesis.

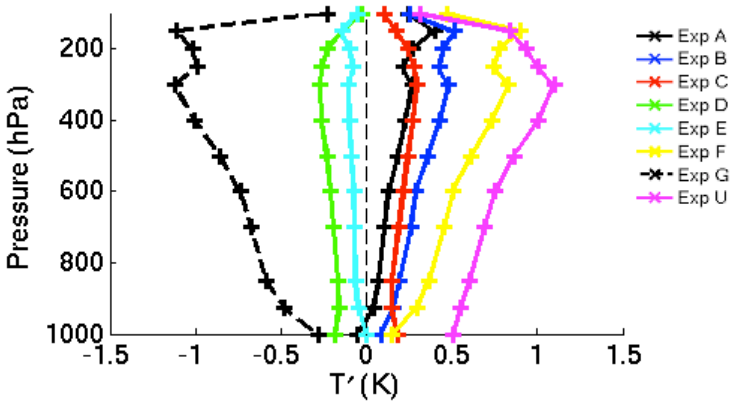


Figure 3.22: Vertical temperature profile changes (K) for each perturbation experiment.

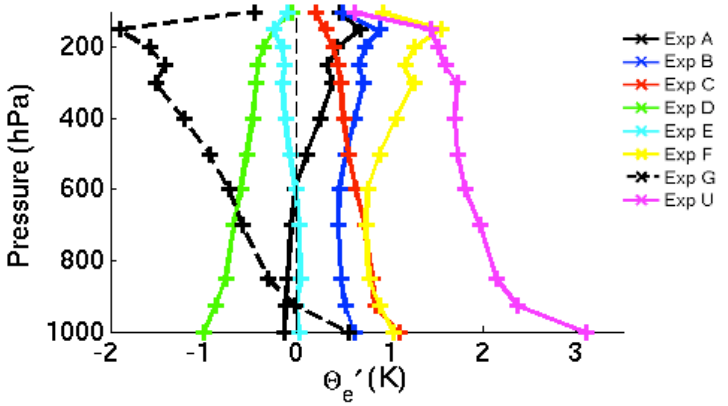


Figure 3.23: Vertical equivalent potential temperature profile changes (K) for each perturbation experiment.

In an attempt to better understand the low cloud anomalies, profiles of the anomalies in temperature and equivalent potential temperature are examined (see figure 3.22

and 3.23). The equivalent potential temperature (θ_e) is the temperature a parcel of air would reach if all the water vapor in the parcel were to condense, releasing its latent heat, and the parcel was brought adiabatically to a standard reference pressure of 1000hPa. In stable conditions, θ_e increases with altitude, therefore comparisons of θ_e of various experiments provides a measure of the stability of the atmosphere. For this purpose we define the low-atmosphere stability to be $\theta_e(700hPa) - \theta_e(925hPa)$.

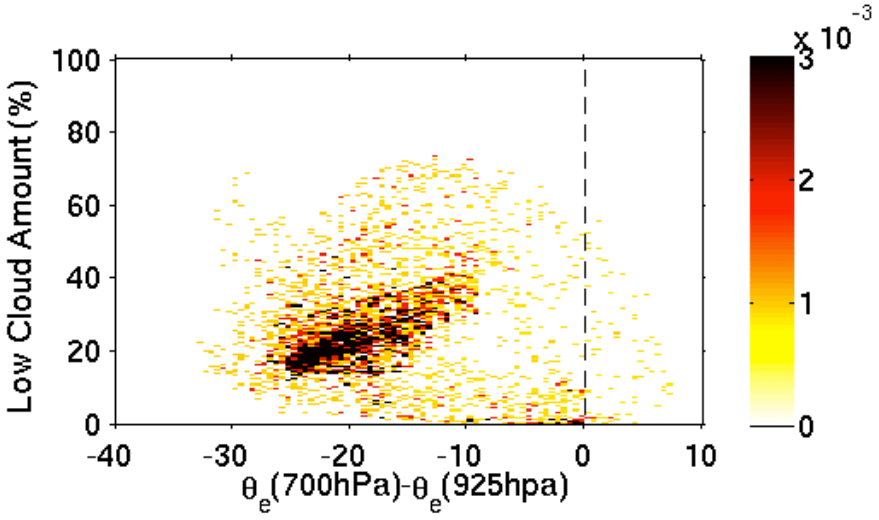


Figure 3.24: Joint distribution density of low cloud amount (%) against the difference in equivalent potential temperature between 700mb and 925mb (K).

The joint distribution density of low could amount against low-atmospheric stability is shown in figure 3.24 for the 30 year control run. Whilst there is a large degree of spread (r=-0.23), an increase in low-atmosphere stability does appear to somewhat coincide with an increase in low cloud amount. Similarly, there is a weak positive relationship (r=+0.53) between low cloud and low-atmospheric stability anomalies. A possible reason for the weak correlation is the low cloud amount encompasses both stratus clouds, which are positively correlated with low-atmospheric stability, and shallow cumulus clouds, which would presumably be anti-correlated with low-atmospheric stability.

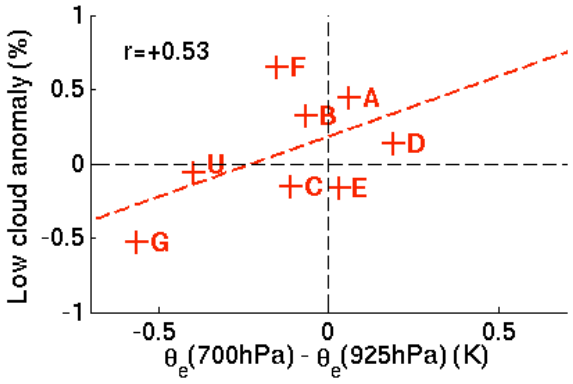


Figure 3.25: Low cloud amount change (%) as a function of the change in the difference in equivalent potential temperature between 700mb and 925mb (K).

3.4.4 Implications for TOA Radiation Budget

Finally, we examine the effect of T_s, A_c and m_c changes on the TOA radiation budget. Figure 3.26 shows the OLR and absorbed SW changes in experiment A, with respect to the control run. For ease of comparison with section 3.3.2 , the solid black contour line of zero temperature change is included. As expected, areas with increased high cloud amount have a decrease in OLR and an increase in reflected SW. It is remarkable that an increase in zonal temperature gradient of only $0.5K$ can result in local SW changes of $\sim 10W/m^2$. It is important to note, however, that we have effectively suspended any atmosphere-ocean coupled feedback, which may prevent such a temperature gradient from occurring in nature.

As expected, the tropical mean OLR increases with tropical mean surface temperature $\langle T_s \rangle$ (r=+0.77). Due to the strong positive correlation between high cloud amount and both A_c and $\langle m_c \rangle$, OLR decreases as both A_c (r=-0.96) and $\langle m_c \rangle$ (r=-0.99) increase.

Absorbed SW is more complicated than OLR as we need to take into consideration the effects of both high and low clouds. As $\langle T_s \rangle$ increases so too does the low cloud amount (see figure 3.21), which causes an increase in albedo and decrease in absorbed SW (r=-0.64). As A_c and $\langle m_c \rangle$ increase, low cloud amount decreases, and

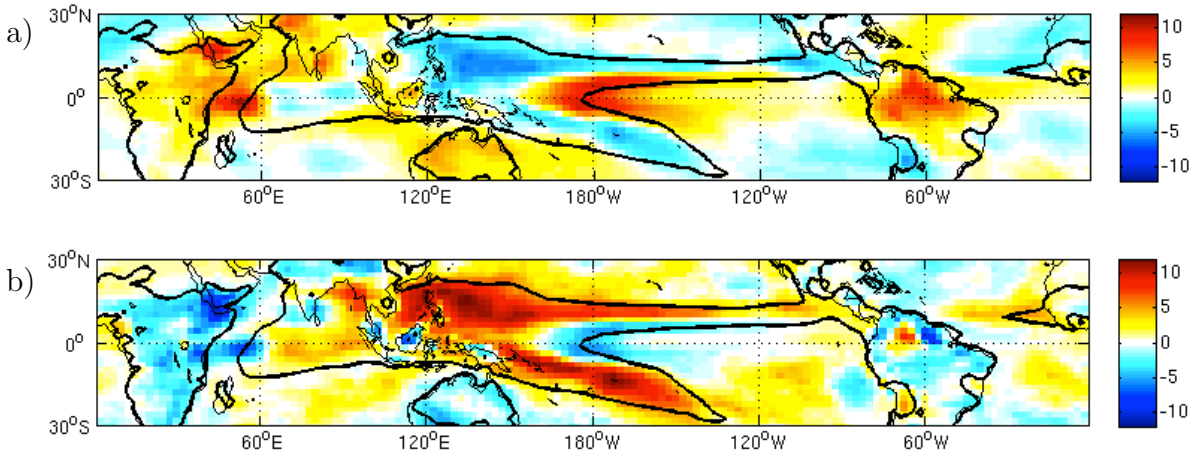


Figure 3.26: Experiment A changes for a) OLR (W/m^2) and b) reflected SW (W/m^2). Positive values indicate an increase relative to the control run.

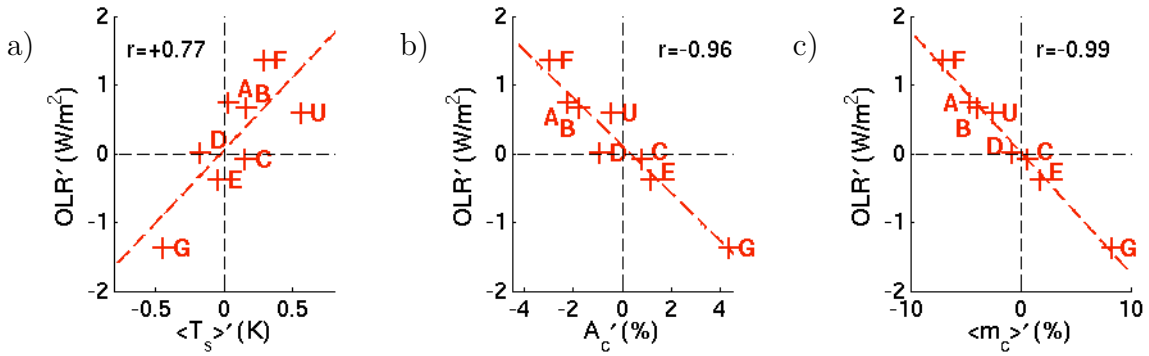


Figure 3.27: OLR changes (W/m^2) for each perturbation experiment as a function of change in (a) tropical average surface temperature (correlation coefficient, r=+0.77), (b) convective area fraction (r=-0.96) and (c) tropical average convective mass flux (r=-0.99).

the absorbed shortwave increases (r=+0.99). The changes in high cloud amount are anti-correlated to that of the low cloud amount, which would presumably decrease the magnitude of the absorbed SW anomalies. Overall, however, the sign of the absorbed SW change appears to be driven by changes in the low cloud amount.

As $\langle T_s \rangle$ increases, both the OLR and SW act to cool the system, which, in a coupled atmosphere-ocean system, would restore the original $\langle T_s \rangle$. For example, a perturbation of $\langle T_s \rangle\prime = -1K$ results in a net TOA imbalance of -4W/m^2. On the other hand, an increase in either A_c or $\langle m_c \rangle$ causes both OLR and SW to warm the

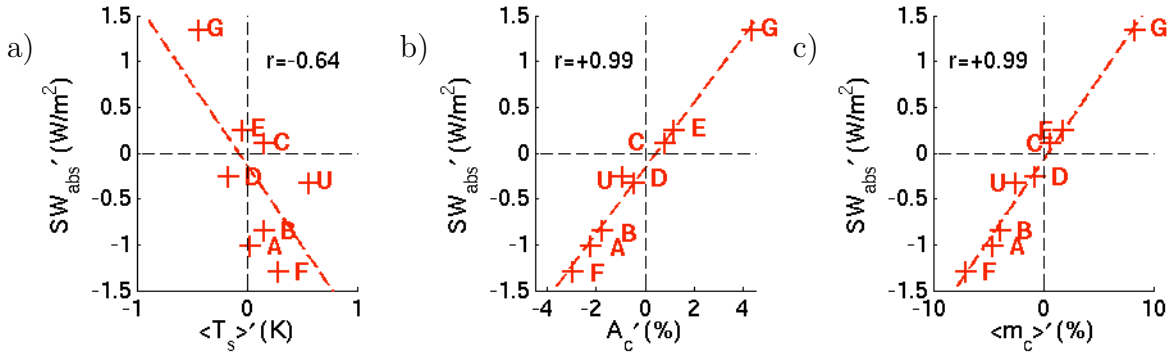


Figure 3.28: Absorbed SW changes (W/m^2) for each perturbation experiment as a function of change in (a) tropical average surface temperature (correlation coefficient, r=-0.64, (b) convective area fraction (r=+0.99) and (c) tropical average convective mass flux (r=+0.99).

system, with a 5% perturbation in $\langle m_c \rangle$ resulting in a net TOA imbalance of $+2W/m^2$. It is beyond the scope of this thesis to understand the impact such a perturbation in m_c would have on coupled system.

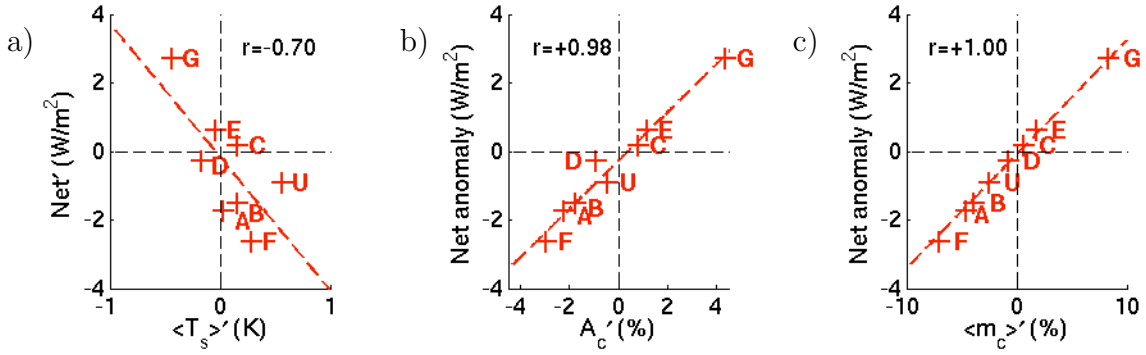


Figure 3.29: Net radiation changes (W/m^2) for each perturbation experiment as a function of change in (a) tropical average surface temperature (correlation coefficient, r=-0.70), (b) convective area fraction (r=+0.98) and (c) tropical average convective mass flux (r=+1.00).

3.5 Conclusions

Our model calculations show that tropical high cloud amount may change less than expected, due to compensation from clouds in non-convective regions that respond to changes in tropical average mass flux. While changes in high cloud amount (combining

convective and non-convective clouds) cannot be directly converted to changes in the column cloud radiative forcing, these results show how different processes that are mechanistically coupled act to reduce the sensitivity of tropical high cloud amount to perturbations.

We also found there to be strong anti-correlations between tropical mean convective mass flux and low cloud amount, liquid water path (LWP) and ice water path (IWP). This is despite the non-linear relationship of low cloud, LWP and IWP with convective mass flux in the base state. As expected, precipitation is most strongly a function of tropical mean surface temperature, however, top-of-atmosphere radiation is more strongly correlated with the convective area and tropical convective mass flux than the tropical mean surface temperature.

Chapter 4

The importance of convective SSTs on tropospheric temperature

4.1 Introduction

Vertical amplification of tropospheric temperature trends are a robust feature of climate change and are supported by radiosonde observations (Lanzante et al., 2003; Thorne et al., 2005). Global circulation models from the Coupled Model Intercomparison Project (CMIP5) also exhibit enhanced tropospheric warming, relative to surface temperature warming, but generally overestimate the magnitude of the trend (Fu et al., 2011; Seidel et al., 2012). A fundamental challenge in comparing these coupled GCMs with observations is that models have inherently different internal variability and spatial distributions of surface temperature. One alternative is to use atmosphere-only models from the Atmospheric Model Intercomparison Project (AMIP), where the sea surface temperatures (SSTs) are prescribed. Whilst tropospheric trends in AMIP simulations are somewhat closer to observations, they still exhibit a large inter model spread (Po-Chedley and Fu, 2012).

Tropospheric temperatures are influenced by surface temperatures via convective adjustment, which results in a temperature profile that roughly approximates a moist adiabat. Convective adjustment, however, only exists in the warmest SST regions where there is frequent precipitation. Given that tropospheric temperatures are dynamically constrained to be nearly horizontally uniform in the tropics (Charney, 1963; Scheider, 1977; Sobel and Bretherton, 2000), it follows that mean tropical tropospheric temperature is determined by the surface temperatures in these warm, precipitating regions (Sobel et al., 2002).

Here we use a method suggested by Flannaghan et al. (2014), whereby we weight the surface temperature of each grid-cell by its fractional amount of precipitation, and show that the precipitation-weighted SST trend explains much of the variability in the tropospheric temperature trend. Previously, Flannaghan et al. (2014) have applied this method to two ensembles of GFDL HiRAM model runs with different commonly used prescribed SSTs, namely the HadISST1 (Rayner et al., 2003) and 'Hurrell' (Hurrell et al., 2008) observational data sets. They found that the two ensembles have a difference in upper tropical tropospheric temperature trends that is a factor 3 larger than expected from moist adiabatic scaling of the tropical average SST trend difference. They conclude that the discrepancy in temperature trends is a consequence of SST trend differences being largest in regions of deep convection.

In the previous chapter, we calculated the change in the tropical mean vertical temperature profile for each of the eight perturbation experiments (see figure 3.22). As expected, an increase in surface temperature results in a warming of the troposphere. The magnitude of this warming however varies from experiment to experiment, as a 1K perturbation of convective SSTs has a larger impact on tropospheric warming than the same perturbation in a non-convective region, due to the convective adjustment mechanism discussed above. Figure 4.1 plots the change in 300mb tropospheric temperature (T_a) as a function of both SST and the precipitation-weighted SST (P·SST).

Whilst there is indeed a strong correlation between T_a and SST (correlation coefficient, r=+0.91), the correlation between T_a and $P \cdot SST$ is stronger (r=+0.98). This result indicates that T_a is more strongly determined by $P \cdot SST$ than simply SST. We explore this concept further by analyzing the output of 19 atmosphere-only models from the Couple Model Intercomparison Project (CMIP5), as whilst all 19 models are forced with historically observed SSTs, there is a large degree of spread in the tropospheric temperatures (Po-Chedley and Fu, 2012)

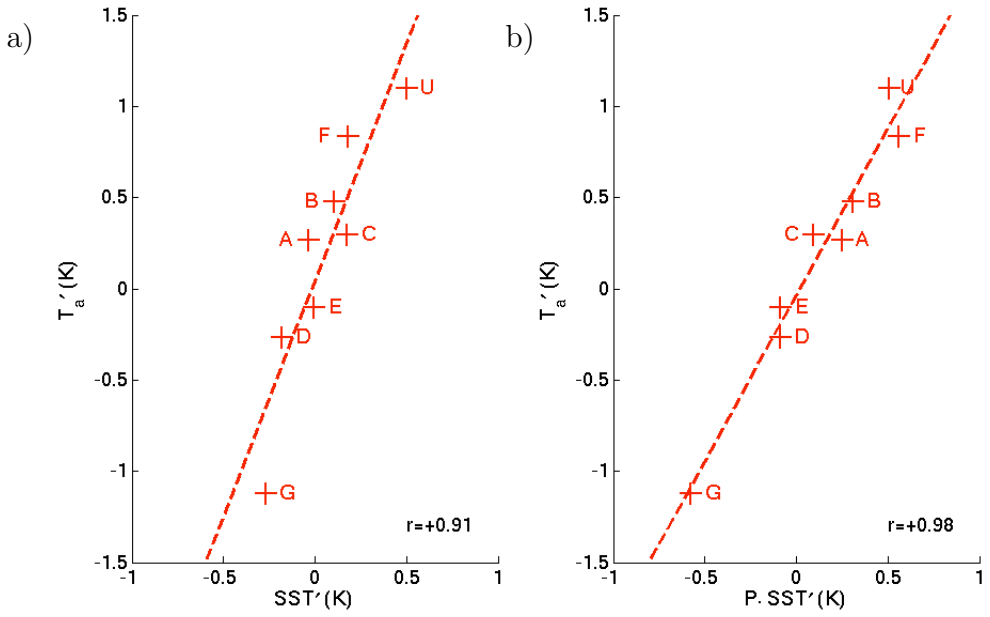


Figure 4.1: 300mb tropospheric temperature changes as a function of changes in a) sea surface temperature (K) and b) precipitation-weighted sea surface temperature (K), for the eight perturbation experiments detailed in Chapter 3.

4.2 Experimental Setup

4.2.1 Data

This study uses CMIP5 simulations (Taylor et al., 2012) from the Atmospheric Model Intercomparison Project (AMIP). Analysis is performed on nineteen AMIP models, as in Po-Chedley and Fu (2012), with up to three ensembles from each. Whilst only

one or two ensemble members are available for several models, if more than three ensembles are available, then the first three in the archive are taken. The time period considered is 1979-2008 and only models that have output for all months are included.

AMIP models use observational records of sea ice and SST evolution as boundary conditions, and therefore have a similar SST trend and variability as observations. As discussed in Flannaghan et al. (2014), models are typically forced with either the HadISST (Rayner et al., 2003) or Hurrell (Hurrell et al., 2008) observational datasets, however, the exact agreement between monthly SSTs in the model and observations depends on how the SSTs are specified in the model. In the initial AMIP simulations, the observed monthly mean SSTs were specified for the middle of each month, and in most models daily SSTs were obtained by linearly interpolating between these monthly mean values (Taylor et al., 2000). Whilst this is the traditional method, much of the SST variance on sub-monthly time-scales is filtered out and the amplitudes of seasonal and inter annual variations in SSTs are damped. For example, consider the warmest month of the year. In order to recover the monthly mean value, the maximum temperature in the month must exceed the mean, but this is clearly impossible if temperatures are linearly interpolated between monthly mean values.

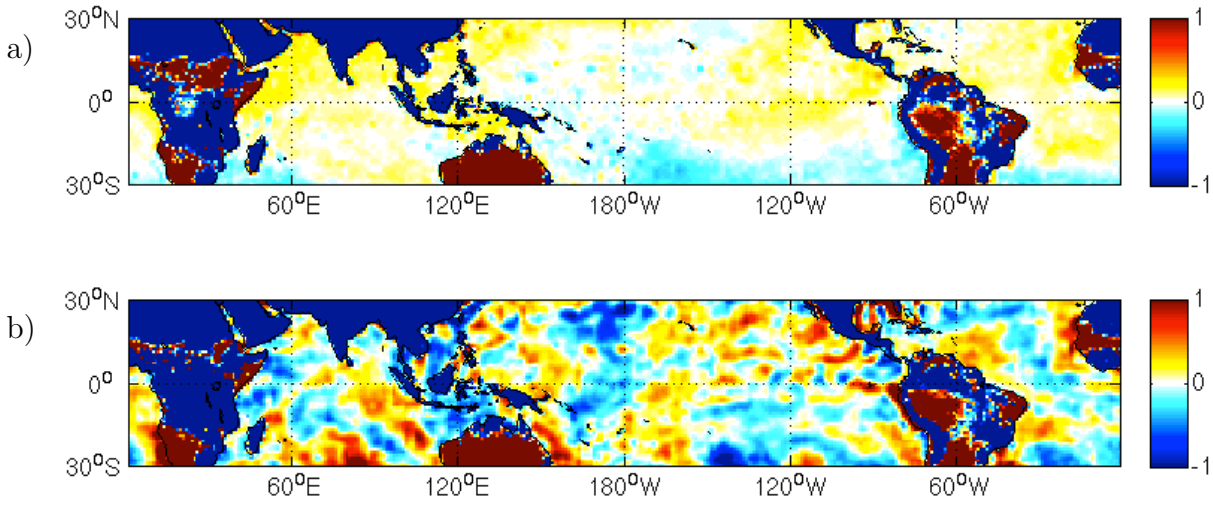


Figure 4.2: GFDL HiRAM-c180 minus a) HadISST and b) Hurrell monthly mean surface temperature (K) for January 1990.

Under the traditional method, the modeled monthly mean temperature for a given month (T_j^*) is related to the monthly mean observational data (T_j) by:

$$T_j^* = (T_{j-1} + 6T_j + T_{j+1})/8 \tag{4.1}$$

Thus for month j, the monthly mean resulting from this procedure is a weighted average of the temperature for three months centered on month j. The monthly mean, T_j^*, will therefore generally differ from T_j by a few tenths of a degree. This is the method used for both of the GFDL models: HiRAM-c180 and HiRAM-c360. Figure 4.2 gives the difference in surface temperature between HiRAM-c180 and a) HadISST observations, and b) Hurrell observations, for January 1990. Whilst the model is in better agreement with the HadISST dataset, there are still regional differences of up to $\sim$0.2K (NB: differences over land are significantly larger as these are not prescribed).

Figure 4.3 also gives the difference between HiRAM-c180 and observations for January 1990, however the 'observations' are now weighted by equation 4.1. The difference between HiRAM-c180 and the weighted HadISST field is zero over all oceans, thus indicating the model input is calculated from linear interpolation of monthly HadISST observations.

Comparison between observations and modeled SSTs for the remaining 17 models gives results similar to that of figure 4.2, with each model in better (but not perfect) agreement with either the HadISST or Hurrell dataset. It is unclear what method individual modeling groups have used in deriving the input SSTs, however they do not appear to use the same interpolation technique employed by GFDLs models. Regardless, all but one of the models are still able to replicate the observed SST trends. The single outlier, MRI-CGCM, exhibit SSTs that don't appear to follow either observational dataset and have different SSTs for each of its ensemble members (i.e. each time the model is run it has different boundary conditions). The SST trend is also larger than either of the observational trends. The reason for this is not clear,

however we hypothesize that the prescribed SSTs might be derived from a coupled model output.

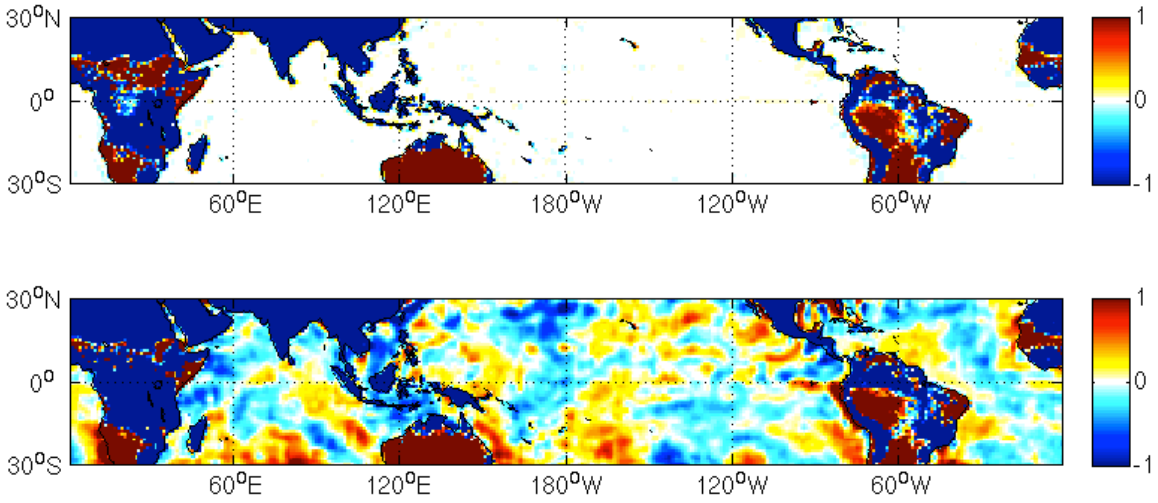


Figure 4.3: GFDL HiRAM-c180 minus interpolated a) HadISST and b) Hurrell monthly mean surface temperature (K) for January 1990. The interpolated fields are calculated using equation 4.1.

4.2.2 Analysis

The model variables used in our analysis are the tropical ($30°S$-$30°N$) surface temperatures (T_s), 300hPa atmospheric temperature (T_a), and precipitation (P). Whilst SSTs are prescribed for the models, they are not provided in the AMIP archive and we therefore extrapolate the SST from the T_s field using a land/sea mask. This mask is on a 1°latitude×1°longitude grid, which must be interpolated to each model grid. The interpolation of the land/sea mask can cause some issues in coastal regions, where the grid-cell is a combination of both land and sea, therefore we have computed tropical SSTs using only grid-cells that contain no land. Depending on the resolution of the model this can cause a small ($< 0.005K$) error in the calculated SST trend.

In addition to the tropical mean SST, we also calculate $P \cdot SST$, which is the precipitation weighted SST. Following Flannaghan et al. (2014), $P \cdot SST$ is calcu-

lated at monthly time-intervals by weighting the temperature in each grid-cell by the fraction of precipitation that is occurring in that grid cell, relative to that months total tropical precipitation.

4.3 Trend Results: 1984-2008

Trends are calculate by ordinary least squares regression over the period 1984-2008, in order to avoid previously noted problems in the SST data (Flannaghan et al., 2014; Po-Chedley and Fu, 2012). As expected, T_a trends exhibit a wide range of values from +0.17 to +0.46 K/decade, despite the prescribed boundary conditions (figure 4.4). The SST trends are divided into two groups that correspond to (1) models forced with HadISST data (SST trend = +0.87K/dec), and (2) models forced with Hurrell data (SST trend = +0.11K/dec). There are also several runs with an SST trend >0.12K/dec, which correspond to the MRI-CGCM3 model that doesn't appear to use either of the aforementioned observational datasets for the boundary conditions.

The raw values of trends are given in table 4.1 for the individual ensemble members, and table 4.2 for the ensemble means. Whilst the spread in T_a trend cannot be explained entirely by the spread in SST trends, it is worth noting that every model that uses the HadISST dataset has a lower T_a trend than any model that uses the Hurrell dataset. The correlation coefficient between the trends in T_a and SST is +0.93 for the ensemble mean values.

The T_a trend is also plotted as a function of $P \cdot SST$ in figure 4.4b, and has the increased correlation coefficient of +0.99 for the ensemble mean values. Whilst the relationship between T_a and $P \cdot SST$ trends is more linear than the relationship between T_a and SST, there is still some degree of spread within the two separate SST groups. Two possible factors that could contribute to this spread are internal variability and differences in model parameterizations, e.g. different convection schemes.

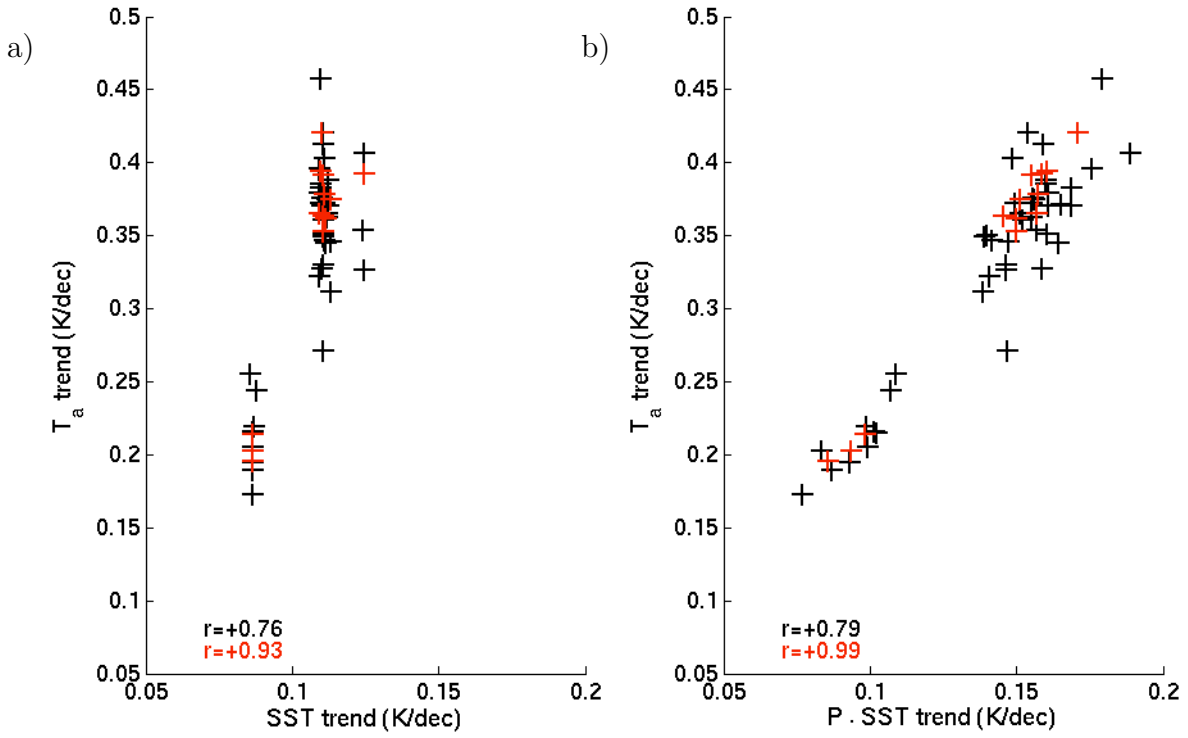


Figure 4.4: Scatter plot of 300mb atmospheric temperature (T_a) trend against a) SST trend and b) P·SST trend. All trends are calculated over the period 1984-2008 and have units of K/decade. Black markers indicate values from individual ensemble members, whilst red markers indicate the ensemble means. The correlation coefficients (r) are given for both individual ensemble members (black text) and ensemble means (red text).

The scaling factors, $F_S = T_a/SST$ and $F_P = T_a/(P \cdot SST)$, are computed by dividing that atmospheric temperature trend by the surface temperature trend variables, SST and $P \cdot SST$, respectively. These factors give a measure of how amplified the surface warming is at altitude and are functions of the model physics and parameterizations. F_S has a multi-model mean of 3.2±0.5 (see figure 4.6), with the individual F_S values dependent on both the model and the individual ensemble member run. F_P has a mean value of 2.4±0.1, which is roughly consistent with moist adiabatic lapse rate theory and radiosonde observations (Santer et al., 2005). These two scaling factors are plotted against one another in figure 4.5, clearly contrasting the large range of F_S values against the relatively small range of F_P values. Given the

standard deviation for F_P is roughly one fifth that for F_S, we conclude that $P \cdot SST$ trend is a more accurate predictor of T_a trend than simply SST trend.

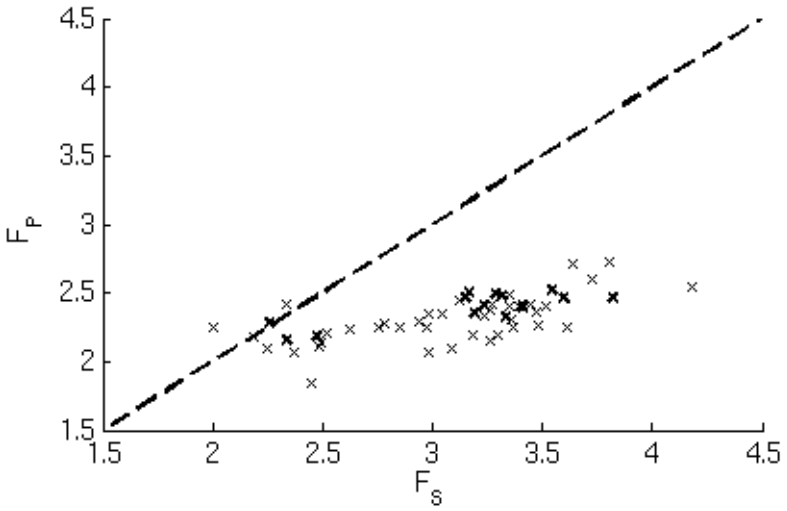


Figure 4.5: Scatter plot of scaling factors, $F_S = T_a/SST$ and $F_P = T_a/(P \cdot SST)$, for the individual ensemble members of 19 AMIP models. Ensemble means are indicated by bold symbols and the dashed line represents the 1:1 relationship.

If we consider the multi-model mean scaling factor, $\overline{F_P}$, the jth ensemble mean will have a scaling factor of $F_P^j = \overline{F_P} + F_P^j{\prime}$. Similarly, the precipitation-weighted SST trend for the jth ensemble mean will be given by $(P \cdot SST)^j = \overline{P \cdot SST} + (P \cdot SST)^j{\prime}$. The 300hPa temperature trend for the jth ensemble is therefore:

$$T_a^j = \left[\overline{F_P} + F_P^j{\prime}\right]\left[\overline{P \cdot SST} + (P \cdot SST)^j{\prime}\right] \tag{4.2}$$

A single multi-model mean F_P is calculated, however calculating a mean for each SST group (i.e. HadISST and Hurrell) does not affect the results significantly. The right hand side of equation 4.2 can be expanded to give the sum of four terms, (1) $\overline{F_P} \cdot \overline{P \cdot SST}$, (2) $\overline{F_P} \cdot (P \cdot SST)^j{\prime}$, (3) $F_P^j{\prime} \cdot \overline{P \cdot SST}$, and (4)$F_P^j{\prime} \cdot (P \cdot SST)^j{\prime}$. The first term is equal to 2.20 K/dec, the second and third terms are plotted against one another in figure 4.7, and the fourth term is negligible. The summation of terms (2) and (3) will give the differences of that models T_a trend from the multi-model mean,

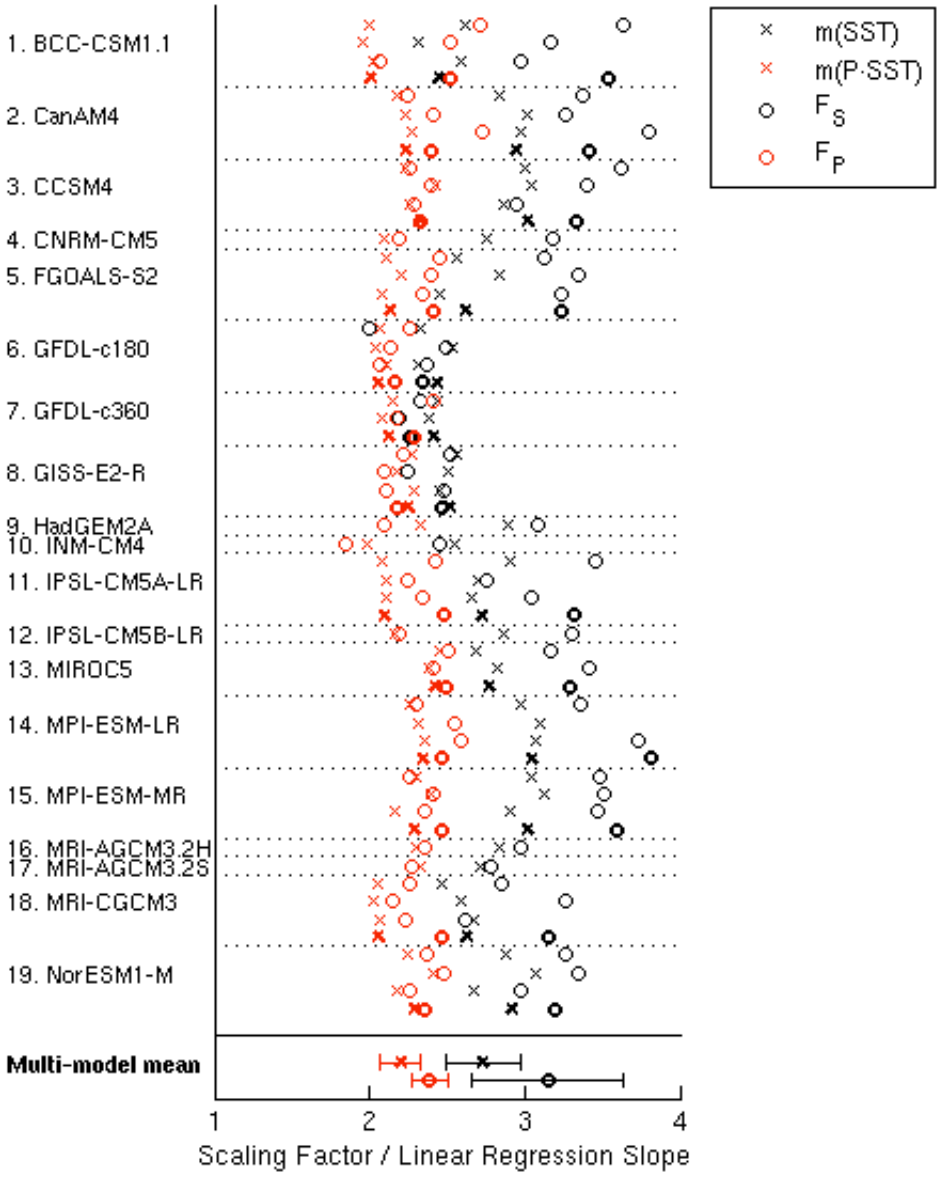


Figure 4.6: Scaling factors, $F_S = T_a/SST$ and $F_P = T_a/(P \cdot SST)$, and linear regression slopes, m(SST) and m$(P \cdot SST)$, for the 19 AMIP models. Ensemble means are indicated by bold symbols.

therefore the dotted square outlines on figure 4.7 indicate T_a trend differences of the same magnitude. Only the 13 models for which we have ensemble means are plotted.

The term on the x-axis, $F_P^{j\prime} \cdot \overline{P \cdot SST}$, is the difference in T_a trend that is due to the difference in F_P for that particular model. The term on y-axis,$\overline{F_P} \cdot (P \cdot SST)\prime$, is the difference in T_a trend that is due to a difference in precipitation-weighted SST

values. Given the strong relationship between $P \cdot SST$ and T_a one might expect $\overline{F_P} \cdot (P \cdot SST)\prime$ to be the dominant term, with only a small contribution from the differences in the individual models F_P values. However, it is clear that these two terms are comparable in magnitude, and that the spread in T_a trends are due in equal part to differences in $P \cdot SST$ and F_P. Further understanding of F_P differences would involve analysis of the physics and parameterizations of individual models and is beyond the scope of this thesis.

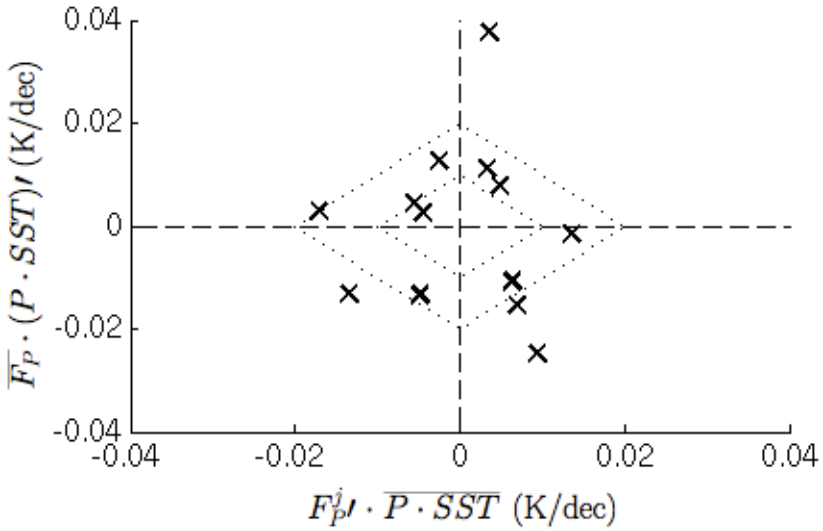


Figure 4.7: Decomposition of T_a trend into $F_P^j\prime \cdot \overline{P \cdot SST}$ (K/dec) and $\overline{F_P} \cdot (P \cdot SST)\prime$ (K/dec) for 13 ensemble means. See text for further details.

4.4 Time series results: 1979-2008

Given the strong correlation between atmospheric temperature (T_a) and precipitation-weighted SST ($P \cdot SST$) trends, one would expect to also see a strong correlation between the time series of T_a and $P \cdot SST$. In order to test this, we have taken annual means over the period 1979-2008, to eliminate any seasonal bias, and linearly regressed each models T_a time series against the corresponding SST and $P \cdot SST$ time series to give the linear regression slopes: m(SST) and m($P \cdot SST$), respectively.

These linear regression slopes are given in figure 4.6, along with the scaling factors F_S and F_P. Though the slopes and scaling factors are calculated on vastly different timescales, there is remarkable agreement between them, indicating the relationship between T_a and the surface is fundamentally the same. Interestingly this agreement is stronger for the slopes and scaling factor of $P \cdot SST$, than SST, which has a larger degree of variability (see figure 4.8).

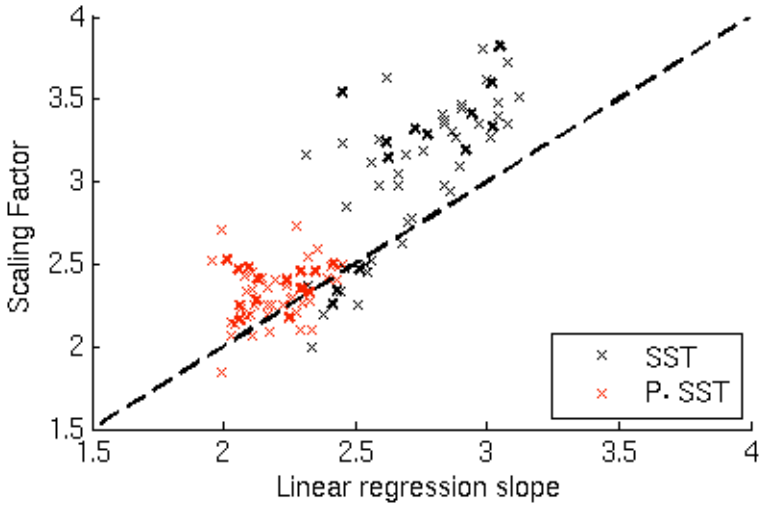


Figure 4.8: Plot of SST and $P \cdot SST$ scaling factors as a function of their corresponding linear regression slope. Ensemble means are indicated by bold markers, and the dashed line indicates the 1:1 relationship between scaling factor and slope.

The correlation coefficient from this linear regression is given in figure 4.9 for each ensemble member, with the ensemble means indicated by bold markers. The correlation of T_a is higher with $P \cdot SST$ than SST for all models, with multi-model mean correlation coefficients of +0.95 and +0.99 for SST and $P \cdot SST$, respectively.

For each pair of ensemble means, we have also computed the time series of differences in T_a, SST and $P \cdot SST$. We then calculate the correlation coefficient between the difference in T_a and the difference in SST (or $P \cdot SST$), in order to determine whether differences in T_a between models are driven by differences in surface temperatures. These results are shown in table 4.3 for SST, and table 4.4 for $P \cdot SST$. The mean correlation is larger for $P \cdot SST$ (r=+0.68) than for SST (r=+0.19), indicat-

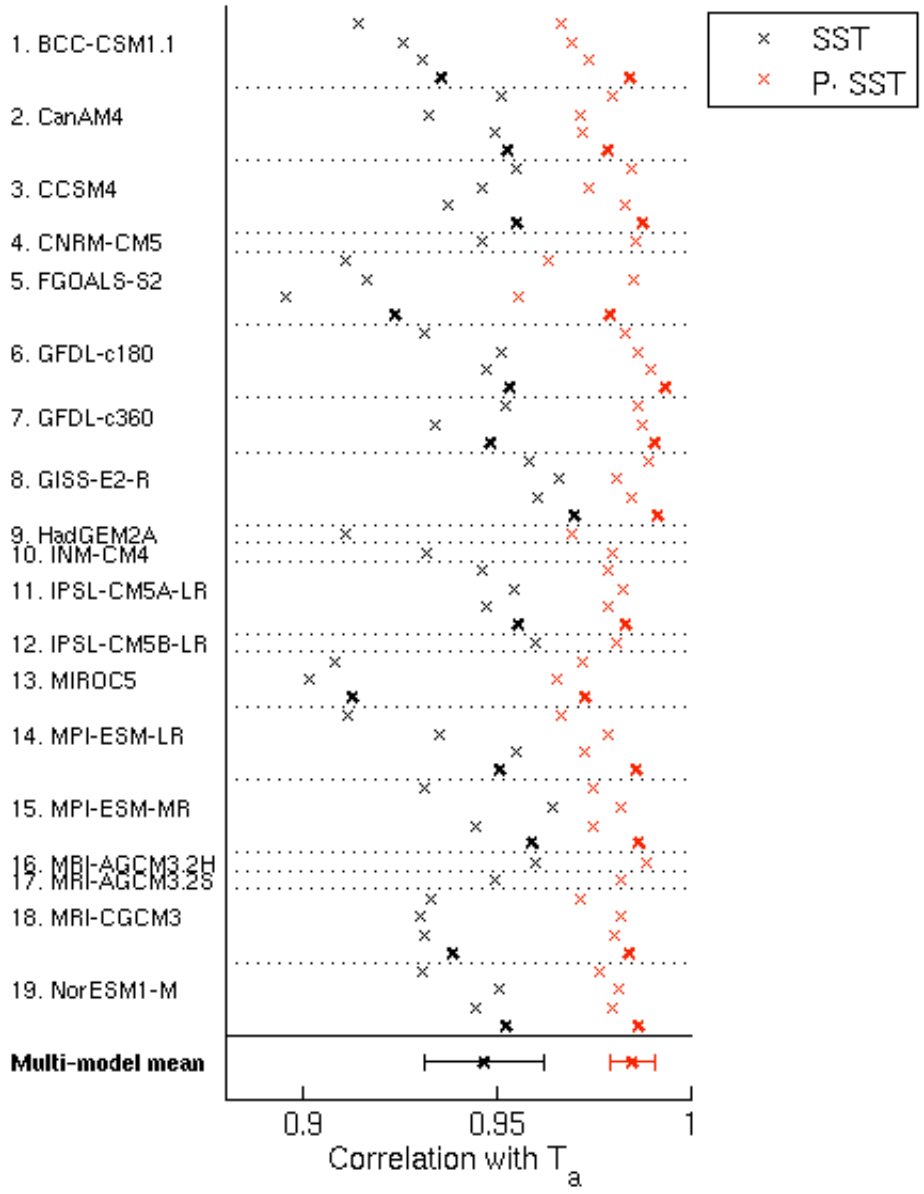


Figure 4.9: Correlation coefficient of the 1979-2008 T_a time series with SST and $P \cdot SST$. Ensemble means are indicated by bold markers.

ing that roughly 50% of the variance in T_a differences are indeed due to differences in $P \cdot SST$. The small correlation coefficients in table 4.4, such as between GFDL HiRAM-c180 and c-360, are most likely due to the fact that they have identical SSTs and convective parameterizations. The similarity between these two models results in small $P \cdot SST$ differences, and T_a differences that are driven primarily by other factors (e.g. random noise). This is supported by the T_a trends in table 4.1, where

multiple runs of HiRAM-c180 result in identical $P \cdot SST$ values but T_a trends that range from +0.173 to 0.216 K/decade.

4.5 Conclusions

We have analyzed the results of 19 AMIP models, which use observational records of sea ice and SST evolution as boundary conditions, and have been run over the period 1979-2008. We find that the AMIP inter model spread in tropical tropospheric temperature trends are due, at least in part, to differences in the precipitation-weighted SST trend (r=+0.99). Tropospheric temperature trends are also correlated with SST trends (r=+0.93), as SSTs are not constant across models due to (1) differences in observational datasets and (2) differences in how SSTs are interpolated for model input. Similar correlations are found when analyzing tropospheric temperature variations on inter annual timescales.

Our analysis confirms that the troposphere does experience enhanced warming relative to the surface, with an amplification or scaling factor of $F_P = 2.4 \pm 0.1$, with respect to the precipitation-weighted SST. When calculated with respect to SSTs alone, the scaling factor (F_S) has a larger magnitude and spread of F_S 3.2 ± 0.5, thus confirming F_P is a more accurate predictor of tropospheric temperature changes.

	T_S (K/dec)	SST (K/dec)	$P \cdot SST$ (K/dec)	300hPa T_a (K/dec)
1. BCC-CSM1.1	0.167	0.111	0.149	0.403
	0.151	0.110	0.139	0.350
	0.147	0.110	0.159	0.328
2. CanAM4	0.152	0.110	0.165	0.372
	0.167	0.112	0.151	0.365
	0.154	0.111	0.154	0.421
3. CCSM4	0.143	0.109	0.176	0.396
	0.145	0.109	0.155	0.372
	0.139	0.109	0.141	0.322
4. CNRM-CM5	0.156	0.110	0.160	0.351
5. FGOALS-s2	0.143	0.111	0.142	0.347
	0.137	0.112	0.156	0.375
	0.155	0.112	0.155	0.363
6. GFDL-HIRAM-c180	0.110	0.086	0.077	0.173
	0.132	0.087	0.101	0.216
	0.128	0.087	0.099	0.205
7. GFDL-HIRAM-c360	0.111	0.087	0.084	0.202
	0.123	0.086	0.087	0.189
8. GISS-E2-R	0.128	0.087	0.099	0.219
	0.112	0.087	0.093	0.195
	0.138	0.087	0.102	0.215
9. HadGEM2A	0.161	0.112	0.164	0.345
10. INM-CM4	0.138	0.111	0.147	0.271
11. IPSL-CM5A-LR	0.160	0.112	0.160	0.388
	0.153	0.113	0.138	0.312
	0.158	0.113	0.147	0.345
12. IPSL-CM5B-LR	0.154	0.112	0.169	0.370
13. MIROC5	0.151	0.111	0.140	0.350
	0.151	0.110	0.156	0.376
14. MPI-ESM-LR	0.160	0.110	0.161	0.370
	0.160	0.110	0.179	0.457
	0.162	0.111	0.159	0.413
15. MPI-ESM-MR	0.159	0.110	0.169	0.382
	0.162	0.110	0.160	0.385
	0.143	0.109	0.161	0.380
16. MRI-AGCM3.2H	0.107	0.086	0.109	0.256
17. MRI-AGCM3.2S	0.125	0.088	0.107	0.244
18. MRI-CGCM3	0.144	0.124	0.157	0.353
	0.180	0.124	0.189	0.406
	0.161	0.125	0.146	0.327
19. NorESM1-M	0.151	0.110	0.152	0.361
	0.155	0.111	0.150	0.372
	0.160	0.111	0.146	0.330

Table 4.1: Trends in T_S, SST, P·SST and 300hPa T_a calculated over the period 1984-2008, in units of K/decade, for the individual ensemble members of 19 AMIP models.

	T_S **(K/dec)**	SST **(K/dec)**	$P \cdot SST$ **(K/dec)**	**300hPa** T_a **(K/dec)**
1. BCC-CSM1.1	0.155	0.110	0.155	0.391
2. CanAM4	0.160	0.111	0.157	0.378
3. CCSM4	0.144	0.109	0.157	0.365
5. FGOALS-s2	0.144	0.112	0.150	0.361
6. GFDL-HIRAM-c180	0.122	0.087	0.094	0.202
7. GFDL-HIRAM-c360	0.117	0.087	0.086	0.195
8. GISS-E2-R	0.128	0.087	0.098	0.214
11. IPSL-CM5A-LR	0.157	0.113	0.151	0.375
13. MIROC5	0.150	0.110	0.145	0.363
14. MPI-ESM-LR	0.161	0.110	0.171	0.421
15. MPI-ESM-MR	0.154	0.110	0.160	0.394
18. MRI-CGCM3	0.160	0.124	0.159	0.392
19. NorESM1-M	0.154	0.111	0.150	0.353

Table 4.2: Trends in T_S, SST, P·SST and 300hPa T_a calculated over the period 1984-2008, in units of K/decade, for the ensemble means of 13 AMIP models. The numbering of the models is consistent with that introduced in table 4.1.

	1	2	3	5	6	7	8	11	13	14	15	18	19
1. BCC-CSM1.1	—	0.138	-0.205	-0.372	0.496	0.507	0.568	0.032	-0.379	-0.112	-0.235	0.206	0.432
2. CanAM4	—	—	-0.088	-0.225	0.563	0.582	0.629	-0.126	-0.307	0.057	0.061	0.111	0.066
3. CCSM4	—	—	—	-0.417	0.622	0.620	0.687	-0.107	-0.343	0.066	0.077	0.358	0.238
5. FGOALS-s2	—	—	—	—	0.633	0.629	0.639	-0.376	0.019	-0.110	-0.298	0.229	-0.411
6. GFDL-HIRAM-c180	—	—	—	—	—	-0.193	-0.112	0.618	0.625	0.532	0.637	0.643	0.566
7. GFDL-HIRAM-c360	—	—	—	—	—	—	0.176	0.604	0.618	0.559	0.668	0.690	0.574
8. GISS-E2-R	—	—	—	—	—	—	—	0.704	0.642	0.609	0.732	0.657	0.634
11. IPSL-CM5A-LR	—	—	—	—	—	—	—	—	-0.338	-0.408	-0.202	0.276	-0.071
13. MIROC5	—	—	—	—	—	—	—	—	—	-0.074	-0.199	0.161	-0.335
14. MPI-ESM-LR	—	—	—	—	—	—	—	—	—	—	-0.096	0.123	-0.007
15. MPI-ESM-MR	—	—	—	—	—	—	—	—	—	—	—	0.318	-0.083
18. MRI-CGCM3	—	—	—	—	—	—	—	—	—	—	—	—	0.234
19. NorESM1-M	—	—	—	—	—	—	—	—	—	—	—	—	—

Table 4.3: Correlation of the difference in atmospheric temperature with the difference in SST between 2 models. Differences are calculated from ensemble mean time series, and the mean correlation coefficient across all ensembles is +0.19.

	1	2	3	5	6	7	8	11	13	14	15	18	19
1. BCC-CSM1.1	—	0.467	0.585	0.732	0.908	0.912	0.855	0.740	0.700	0.502	0.417	0.646	0.505
2. CanAM4	—	—	0.490	0.393	0.861	0.885	0.853	0.504	0.574	0.256	-0.135	0.295	0.694
3. CCSM4	—	—	—	0.552	0.917	0.930	0.922	0.550	0.683	0.674	0.441	0.435	0.644
5. FGOALS-s2	—	—	—	—	0.885	0.901	0.837	0.782	0.601	0.522	0.585	0.654	0.605
6. GFDL-HIRAM-c180	—	—	—	—	—	0.550	0.513	0.894	0.831	0.887	0.885	0.904	0.905
7. GFDL-HIRAM-c360	—	—	—	—	—	—	0.579	0.898	0.876	0.891	0.887	0.902	0.910
8. GISS-E2-R	—	—	—	—	—	—	—	0.844	0.850	0.890	0.884	0.812	0.922
11. IPSL-CM5A-LR	—	—	—	—	—	—	—	—	0.717	0.538	0.477	0.711	0.565
13. MIROC5	—	—	—	—	—	—	—	—	—	0.678	0.537	0.615	0.773
14. MPI-ESM-LR	—	—	—	—	—	—	—	—	—	—	0.680	0.459	0.621
15. MPI-ESM-MR	—	—	—	—	—	—	—	—	—	—	—	0.262	0.561
18. MRI-CGCM3	—	—	—	—	—	—	—	—	—	—	—	—	0.533
19. NorESM1-M	—	—	—	—	—	—	—	—	—	—	—	—	—

Table 4.4: Correlation of the difference in atmospheric temperature with the difference in $P \cdot SST$ between 2 models. Differences are calculated from ensemble mean time series, and the mean correlation coefficient across all ensembles is +0.68.

Chapter 5

Critical Discussion

The primary objectives of this thesis have been to understand how tropical changes in sea surface temperature (SSTs) and convective mass flux affect high cloud amount, top-of-atmosphere radiative flux, precipitation and tropospheric temperature. Here, we will summarize the primary results and conclusions from chapters 2, 3 and 4.

In Chapter 2, we made use of the short timescale and large amplitude of ENSO to analyze the relation between variations in spatial patterns and area-averaged quantities in the top-of atmosphere radiative fluxes, cloud amount and precipitation, over the period 1979-2008. We used both satellite observations and atmosphere-only models, which are forced with prescribed SSTs, to enable us to directly compare model output with observations. Analysis of the climatological mean (base states) of four GFDL models shows that while OLR and SW biases may be large on the regional scale, they agree relatively well with observations in the tropical mean. The high cloud amount in AM3, for example, is roughly double that of ISCCP observations in the base state, thus causing local OLR biases of up to -36W/m^2, particularly in the western Pacific warm pool. There are also SW biases of up to -70W/m^2 in the stratus deck regions, where all four models appear to have too little low cloud amount. Exact

biases of mid and low level cloud amounts are difficult to quantify due to the masking effect of high clouds.

This inability to evaluate a model's low and mid level cloud amount is a significant constraint. The majority of cloud feedback uncertainty arises from low clouds, however if we are unable to accurately evaluate low clouds in the climatological mean, we face an impossible task in evaluating low cloud feedbacks. The ISCCP simulator is a useful tool in comparing observations and models, as it tells us what ISCCP would 'see' if the model world was in fact reality. To date, however, the ISCCP simulator has only been run with GFDL AM3. Future inclusion of not only ISCCP, but also CloudSat and CALIPSO simulators, on all climate models would be a productive step forward in the evaluation of modeled cloud properties. As active sensors, both CloudSat and CALIPSO have the added advantage of being able to retrieve cloud profile information, thus significantly enhancing the information gained from ISCCP alone.

An El Niño event is associated with an increase in tropical average sea surface temperature of order +0.1K (with a maximum of +0.5K), large local anomalies of +2K (maximum of +6K), and tropical tropospheric warming of +0.5K (maximum +1K). We find that model-to-observation biases in the base state translate into corresponding biases in anomalies in response to El Niño. The pattern and amplitude of model biases in reflected shortwave (SW) and outgoing long wave radiation (OLR) follows expectations based on their biases in cloud amount. In other words, models with a positive cloud amount bias compared to observations, have too strong local responses to El Niño in cloud amount, SW, OLR and precipitation.

Tropical average OLR increases in response to El Niño in observations and models, as the correlation coefficients (r) between OLR and the Nino 3.4 index are in the range 0.4-0.6. Weaker correlations are found for SW(r: -0.6 to 0), cloud amount (r:-0.2 to

+0.1), and precipitation (r:-0.2 to 0). Compositing El Niño events over the period 2001-2007 yields similar results.

These results indicate that the primary response to El Niño is an increase in clear sky OLR, due to a heat pulse from the ocean, and a spatial reorganization of the atmosphere. This can be explained from the point of view that El Niño is "essentially a simple shift of the entire (SST) histogram, with no change in shape" (Sobel et al., 2002). The tropical mean high cloud amount changes very little during El Niño, and we therefore argue total high cloud amount is insensitive to such a 'shift' in the SST histogram. Remarkably, this weak response in high cloud amount is consistent across both models and observations, even when very large base state cloud biases exist.

Chapter 3 takes one of the atmosphere-only models from Chapter 2, GFDL AM2, and forces it with various idealized SSTs. In particular, we are interested in changing the underlying forcing *distribution* of SSTs, rather than simply shifting the distribution as we did in Chapter 2. This allows us to study the sensitivity of high clouds, TOA radiative fluxes and precipitation to the spatial distribution of SSTs and large-scale convective organization. In addition to the 'control' run, which is identical to that used in Chapter 2, eight separate SST perturbation experiments are performed. Each experiment involves a perturbation of tropical SSTs in either the convective region, non-convective region, or both, and is run for the 30 year period 1979-2008.

We characterize the convective mass flux distribution and changes therein in terms of the tropical mean convective mass flux, $\langle m_c \rangle$, and the fraction of the tropics that contains 80% of the convective mass flux (A_c). As expected, warming of convective areas decreases the tropical average convective mass flux ($\langle m_c \rangle$) (Held and Soden, 2006). Further, an increase/decrease in the temperature contrast between convective and non-convective regions leads to a decrease/increase in the convective area fraction A_c, consistent with the "upped-ante mechanism" (Neelin, 2003). Unfortunately, our efforts to determine a statistical relationship between local convective mass flux

and high cloud amount were unsuccessful. This was due to the relation being not only skewed, particularly for large convective mass fluxes (as cloud amount cannot exceed 100%), but also non-compact. The degree of spread is due to geographical differences in the spectra of events that lead to high could amount, namely (i) local convection, (ii) non-convective clouds, (iii) convective clouds without local convective due to advection from surrounding convective events. Despite this complex relationship between local (i.e. grid-cell scale) m_c and high cloud amount we found high correlations between the tropical mean values.

We showed that while the change in tropical mean high cloud amount has some relation with the change in average SST (r=+0.26), the associations with convective area fraction A_c (r=+0.89) and convective mass flux $\langle m_c \rangle$ (r=+0.84) are much stronger. Surprisingly, however, all experiments show a fractional high cloud amount change that is less than fractional changes in $\langle m_c \rangle$. High cloud amount is half as sensitive as expected from the climatological average cloud amount, as a function of convective mass flux, due to strong compensation from non convective high cloud. The latter results from changes in relative humidity related to changes in tropical mean $\langle m_c \rangle$ and the corresponding effect on local subsidence rates. This compensation effect renders high cloud amount remarkably robust to perturbations, though radiative effects of convective and non convective clouds will differ.

Quantitatively, the amount of compensation between convective and non-convective high cloud amount might depend on model formulation. For this reason, we have emphasized the framework of analysis, which provides a physically plausible interpretation of the model results and involved mechanisms. Ideally, other modeling groups would run similar experiments based on our framework, that would in turn provide a more robust characterization of high cloud responses to changes in convective organization as forced by changes in the SST distribution. Perhaps an initial

step would be to perform this analysis on other GFDL models, such as HiRAM, before reaching out to the larger climate modeling community.

For reasons that are not well understood, we also find that there are strong anti-correlations between $\langle m_c \rangle$ and tropical mean low cloud amount (r=-0.96), LWP (r=-0.99) and IWP (r=-0.99). This is a surprising result given the non-linear relationship between local $\langle m_c \rangle$ and low cloud amount (or LWP or IWP) in the climatological base state.

The response of the top-of-atmosphere radiative balance to changes in either $\langle m_c \rangle$ or A_c is complex as we need to consider multiple changes within the atmosphere. For example, as $\langle m_c \rangle$ increases, so too does high cloud amount, however IWP and LWP decrease. Despite these opposing effects, the high cloud amount changes dominate the OLR, which decreases as $\langle m_c \rangle$ increases. The absorbed SW response is dominated by changes in low cloud amount, and absorbed SW increases with increasing $\langle m_c \rangle$.

As expected, total tropical precipitation is most strongly a function of mean surface temperature. This is due to energy constraints at the surface, which limit the rate of evaporation and consequently precipitation (Held and Soden, 2006).

Finally, in Chapter 4 we examine tropospheric temperature in 19 Atmospheric Model Intercomparison Project (AMIP) models, which have prescribed SSTs but still exhibit a large inter model spread in tropospheric temperature trends. We note that the tropospheric temperature is influenced by surface temperatures via convective adjustment, which primarily exists in regions of warm SST and frequent precipitation. Because tropospheric temperatures are dynamically constrained to be nearly horizontally uniform in the tropics, the tropical mean tropospheric temperature must be determined by SSTs in these warm precipitating regions.

As expected, the 300hPa tropospheric temperature (T_a) trends exhibit a wide range of values from +0.17K to +0.46 K/decade, when calculated over the period 1984-2008. We find that ensemble mean tropospheric temperature trends, are more

strongly correlated with precipitation-weighted SST trends (r=+0.99) than with SST trends alone (r=+0.93). Similar correlations are found when the analysis is performed on inter annual, rather than decadal, timescales. Nevertheless, the strong correlation with SST trends is surprising as one would expect AMIP models, which use observational records of sea ice and SST evolution as boundary conditions, to have the same SST values. However, the monthly SST fields vary from model to model. This is for two main reasons: (1) two different observational datasets are used, HadISST and Hurrell, and (2) each model then interpolates the observational dataset to form its own boundary conditions. Unfortunately, the interpolation techniques used for each model are not immediately apparent.

Vertical amplification of tropospheric temperatures, relative to the surface, are a robust feature of climate change and are further supported by our analysis. The tropospheric temperature scaling factors were found to be 3.2 ± 0.5 and 2.4 ± 0.1, when calculated with respect to the SST and precipitation-weight SST trends, respectively. Difference in T_a trends between models was found to be due to both differences in precipitation-weighted SST trends, and differences in scaling factors, in roughly equal parts. Scaling factors themselves appear to depend on both model formulation and on the noise/variability of each individual ensemble member. When the scaling factor is determined with respect to the precipitation-weighted SST trend, the standard deviation is considerably smaller, suggesting that precipitation-weighted SSTs are a more accurate way of predicting tropospheric temperature trends.

Bibliography

Adler, R. and Huffman, G. (2003), 'The version-2 global precipitation climatology project (GPCP) monthly precipitation analysis (1979-present)', *Journal of Hydrometeorology* **4**, 1147–1167.

Bender, F. A., Ramanathan, V. and Tselioudis, G. (2012), 'Changes in extratropical storm track cloudiness 1983 to 2008: observational support for a poleward shift', *Climate Dynamics* **38**, 2037–2053.

Bony, S., Colman, R., Kattsov, V. M., Allan, R. P., Bretherton, C. S., Dufresne, J.-L., Hall, A., Hallegatte, S., Holland, M. M., Ingram, W., Randall, D. A., Soden, B. J., Tselioudis, G. and Webb, M. J. (2006), 'How Well Do We Understand and Evaluate Climate Change Feedback Processes?', *Journal of Climate* **19**, 3445–3482.

Bony, S. and Dufresne, J. (2005), 'Marine boundary layer clouds at the heart of tropical cloud feedback uncertainties in climate models', *Geophysical Research Letters* **32**, L20806.

Bony, S., Dufresne, J., Le Treut, H., Morcrette, J. and Senior, C. (2004), 'On dynamic and thermodynamic components of cloud changes', *Climate Dynamics* **22**, 71–86.

Boucher, O., Randall, D., Artaxo, P., Bretherton, C., Feingold, G., Forster, P., Kerminen, V.-M., Kondo, Y., Liao, H., Lohmann, U., Rasch, P., Satheesh, S. K., Sherwood, S., Stevens, B. and Zhang, X. Y. (2013), Clouds and Aerosols., *in* 'Climate Change 2013: The Physical Science Basis. Contribution of Working Group I to the Fifth Assessment Report of the Intergovernmental Panel on Climate Change.', Cambridge University Press, Cambridge, United Kingdom and New York, NY, USA.

Bretherton, C. S., McCaa, J. R. and Grenier, H. (2004), 'A new parameterization for shallow cumulus convection and its application to marine subtropical cloud-topped boundary layers. Part I: Description and 1D results', *Monthly Weather Review* **132**, 864–882.

Bretherton, C. S. and Sobel, A. H. (2002), 'A simple model of a convectively coupled Walker circulation using the weak temperature gradient approximation', *Journal of Climate* **15**, 2907–2920.

Charney, J. G. (1963), 'A Note on Large-Scale Motions of the Tropics', *Journal of the Atmospheric Sciences* **20**, 607–609.

Clement, A. C., Burgman, R. and Norris, J. R. (2009), 'Observational and model evidence for positive low-level cloud feedback.', *Science* **325**(5939), 460–4.

Collins, M., An, S., Cai, W., Ganachaud, A., Guilyardi, E., Jin, F., Jochum, M., Lengaigne, M., Power, S., Timmermann, A. and Others (2010), 'The impact of global warming on the tropical Pacific Ocean and El Niño', *Nature Geoscience* **3**, 391–397.

Donner, L. (1993), 'The Cumulus Parameterization Including Mass Fluxes, Vertical Momentum Dynamics, and Mesoscale Effects', *Journal of the Atmospheric Sciences* **50**, 889–906.

Donner, L. J., Seman, C. J., Hemler, R. S. and Fan, S. (2001), 'A Cumulus Parameterization Including Mass Fluxes, Convective Vertical Velocities, and Mesoscale Effects: Thermodynamic and Hydrological Aspects in a General Circulation Model', *Journal of Climate* **14**, 3444–3463.

Donner, L. J., Wyman, B. L., Hemler, R. S., Horowitz, L. W., Ming, Y., Zhao, M., Golaz, J.-C., Ginoux, P., Lin, S.-J., Schwarzkopf, M. D., Austin, J., Alaka, G., Cooke, W. F., Delworth, T. L., Freidenreich, S. M., Gordon, C. T., Griffies, S. M., Held, I. M., Hurlin, W. J., Klein, S. a., Knutson, T. R., Langenhorst, A. R., Lee, H.-C., Lin, Y., Magi, B. I., Malyshev, S. L., Milly, P. C. D., Naik, V., Nath, M. J., Pincus, R., Ploshay, J. J., Ramaswamy, V., Seman, C. J., Shevliakova, E., Sirutis, J. J., Stern, W. F., Stouffer, R. J., Wilson, R. J., Winton, M., Wittenberg, A. T. and Zeng, F. (2011), 'The Dynamical Core, Physical Parameterizations, and Basic Simulation Characteristics of the Atmospheric Component AM3 of the GFDL Global Coupled Model CM3', *Journal of Climate* **24**, 3484–3519.

Evan, A. T., Heidinger, A. K. and Vimont, D. J. (2007), 'Arguments against a physical long-term trend in global ISCCP cloud amounts', *Geophysical Research Letters* **34**, L04701.

Flannaghan, T. J., Fueglistaler, S., Held, I. M., Po-Chedley, S., Wyman, B. and Zhao, M. (2014), 'Tropical Temperature Trends in AMIP Simulations and the Impact of SST Uncertainties', *In prep.* .

Fu, Q., Manabe, S. and Johanson, C. M. (2011), 'On the warming in the tropical upper troposphere: Models versus observations', *Geophysical Research Letters* **38**, L15704.

GFDL GAMDT (2004), 'The new GFDL global atmosphere and land model AM2LM2: Evaluation with prescribed SST simulations', *Journal of Climate* **17**, 4641–4673.

Hansen, J., Sato, M. and Ruedy, R. (2006), 'Global temperature change', *Proceedings of the National Academy of Sciences of the United States of America* **106**, 14288–14293.

Harrison, E., Minnis, P. and Barkstrom, B. (1990), 'Seasonal variation of cloud radiative forcing derived from the Earth Radiation Budget Experiment', *Journal of Geophysical Research* **95**, 18687–18703.

Hartmann, D. and Larson, K. (2002), 'An important constraint on tropical cloud-Climate feedback', *Geophysical Research Letters* **29**(20).

Hartmann, D. and Michelsen, M. (1993), 'Large-scale effects on the regulation of tropical sea surface temperatures', *Journal of Climate* **6**, 2049–2062.

Held, I. M. and Soden, B. J. (2006), 'Robust Responses of the Hydrological Cycle to Global Warming', *Journal of Climate* **19**, 5686–5699.

Hurrell, J. W., Hack, J. J., Shea, D., Caron, J. M. and Rosinski, J. (2008), 'A New Sea Surface Temperature and Sea Ice Boundary Dataset for the Community Atmosphere Model', *Journal of Climate* **21**(19), 5145–5153.

Kato, S., Rose, F. G., Sun-Mack, S., Miller, W. F., Chen, Y., Rutan, D. a., Stephens, G. L., Loeb, N. G., Minnis, P., Wielicki, B. a., Winker, D. M., Charlock, T. P., Stackhouse, P. W., Xu, K.-M. and Collins, W. D. (2011), 'Improvements of top-of-atmosphere and surface irradiance computations with CALIPSO-, CloudSat-, and MODIS-derived cloud and aerosol properties', *Journal of Geophysical Research* **116**, D19209.

Kiehl, J. (1994), 'On the observed near cancellation between longwave and shortwave cloud forcing in tropical regions', *Journal of Climate* **7**, 559–565.

Klein, S. A., Zhang, Y., Zelinka, M. D., Pincus, R., Boyle, J. and Gleckler, P. J. (2013), 'Are climate model simulations of clouds improving? An evaluation using the ISCCP simulator', *Journal of Geophysical Research: Atmospheres* **118**, 1329–1342.

Knapp, K. R. (2008), 'Calibration Assessment of ISCCP Geostationary Infrared Observations Using HIRS', *Journal of Atmospheric and Oceanic Technology* **25**, 183–195.

Knutson, T. R. and Manabe, S. (1995), 'Time-mean response over the tropical Pacific to increased C02 in a coupled ocean-atmosphere model', *Journal of Climate* **8**, 2181–2199.

Lanzante, J., Klein, S. and Seidel, D. (2003), 'Temporal homogenization of monthly radiosonde temperature data. Part II: Trends, sensitivities, and MSU comparison', *Journal of Climate* **16**, 241–262.

Larson, K. and Hartmann, D. (2003), 'Interactions among cloud, water vapor, radiation, and large-scale circulation in the tropical climate. Part II: Sensitivity to spatial gradients of sea surface temperature.', *Journal of Climate* **16**, 1441–1455.

Loeb, N. G., Kato, S., Su, W., Wong, T., Rose, F. G., Doelling, D. R., Norris, J. R. and Huang, X. (2012), 'Advances in Understanding Top-of-Atmosphere Radiation Variability from Satellite Observations', *Surveys in Geophysics* **33**(3-4), 359–385.

Loeb, N. G., Wielicki, B. a., Doelling, D. R., Smith, G. L., Keyes, D. F., Kato, S., Manalo-Smith, N. and Wong, T. (2009), 'Toward Optimal Closure of the Earth's Top-of-Atmosphere Radiation Budget', *Journal of Climate* **22**, 748–766.

Neelin, J. D. (2003), 'Tropical drought regions in global warming and El Niño teleconnections', *Geophysical Research Letters* **30**(24), 2275.

Po-Chedley, S. and Fu, Q. (2012), 'Discrepancies in tropical upper tropospheric warming between atmospheric circulation models and satellites', *Environmental Research Letters* **7**(4), 044018.

Radley, C. and Fueglistaler, S. (2014), 'The role of large scale convective organization for tropical high cloud amount', *Geophysical Research Letters* **41**(14), 5259–5263.

Radley, C., Fueglistaler, S. and Donner, L. (2014), 'Cloud and Radiative Balance Changes in Response to ENSO in Observations and Models', *Journal of Climate* **27**(9), 3100–3113.

Ramanathan, V. and Collins, W. (1991), 'Thermodynamic regulation of ocean warming by cirrus clouds deduced from observations of the 1987 El Nino', *Nature* **351**, 27–32.

Raschke, E., Kinne, S. and Stackhouse, P. (2012), WCRP Report: GEWEX Radiative Flux Assessment, Technical report.

Rayner, N. A., Parker, D. E., Horton, E. B., Folland, C. K., Alexander, L. V. and Rowell, D. P. (2003), 'Global analyses of sea surface temperature, sea ice, and night marine air temperature since the late nineteenth century', *Journal of Geophysical Research* **108**(D14), 4407.

Rossow, W. and Schiffer, R. (1991), 'ISCCP cloud data products.', *Bulletin of the American Meteorological Society* **72**, 2–20.

Santer, B. D., Wigley, T. M. L., Mears, C., Wentz, F. J., Klein, S. A., Seidel, D. J., Taylor, K. E., Thorne, P. W., Wehner, M. F., Gleckler, P. J., Boyle, J. S., Collins, W. D., Dixon, K. W., Doutriaux, C., Free, M., Fu, Q., Hansen, J. E., Jones, G. S., Ruedy, R., Karl, T. R., Lanzante, J. R., Meehl, G. A., Ramaswamy, V., Russell, G. and Schmidt, G. A. (2005), 'Amplification of surface temperature trends and variability in the tropical atmosphere.', *Science* **309**, 1551–6.

Scheider, E. (1977), 'Axially Symmetric Steady-State Models of the Basic State for Instability and Climate Studies. Part II. Nonlinear Calculations', *Journal of the Atmospheric Sciences* **34**, 280–296.

Seidel, D. J., Free, M. and Wang, J. S. (2012), 'Reexamining the warming in the tropical upper troposphere: Models versus radiosonde observations', *Geophysical Research Letters* **39**, L22701.

Sherwood, S. C., Ingram, W., Tsushima, Y., Satoh, M., Roberts, M., Vidale, P. L. and O'Gorman, P. a. (2010), 'Relative humidity changes in a warmer climate', *Journal of Geophysical Research* **115**, D09104.

Sobel, A. H. and Bretherton, C. S. (2000), 'Modeling tropical precipitation in a single column', *Journal of Climate* **13**, 4378–4392.

Sobel, A., Held, I. and Bretherton, C. (2002), 'The ENSO signal in tropical tropospheric temperature.', *Journal of Climate* **15**, 2702–2706.

Stephens, G. L. (2005), 'Cloud Feedbacks in the Climate System: A Critical Review', *Journal of Climate* **18**, 237–273.

Stephens, G. L., Li, J., Wild, M., Clayson, C. A., Loeb, N., Kato, S., L'Ecuyer, T., Stackhouse, P. W., Lebsock, M. and Andrews, T. (2012), 'An update on Earth's energy balance in light of the latest global observations', *Nature Geoscience* **5**, 691–696.

Taylor, K. E., Stouffer, R. J. and Meehl, G. a. (2012), 'An Overview of CMIP5 and the Experiment Design', *Bulletin of the American Meteorological Society* **93**, 485–498.

Taylor, K. E., Williamson, D. and Zwiers, F. (2000), *The sea surface temperature and sea-ice concentration boundary conditions for AMIP II simulations*, CMDI report No. 60, Program for Climate Model Diagnosis and Intercomparison Climate and Global Dynamics Division, Lawrence Livermore National Laboratory, Livermore, California.

Thorne, P. W., Parker, D. E., Tett, S. F., Jones, P. D., McCarthy, M., Coleman, H. and Brohan, P. (2005), 'Revisiting radiosonde upper air temperatures from 1958 to 2002', *Journal of Geophysical Research* **110**, D18105.

Tiedtke, M. (1993), 'Representation of clouds in large-scale models', *Monthly Weather Review* **121**, 3040–3061.

Trenberth, K. (1997), 'The definition of El Niño', *Bulletin of the American Meteorological Society* **78**, 2771–2778.

Trenberth, K. E. (2002), 'Changes in tropical clouds and radiation.', *Science* **296**, 2095.

Trenberth, K. E. and Fasullo, J. T. (2009), 'Global warming due to increasing absorbed solar radiation', *Geophysical Research Letters* **36**, L07706.

Webb, M., Senior, C., Bony, S. and Morcrette, J.-J. (2001), 'Combining ERBE and ISCCP data to assess clouds in the Hadley Centre, ECMWF and LMD atmospheric climate models', *Climate Dynamics* **17**, 905–922.

Wetherald, R. and Manabe, S. (1980), 'Cloud cover and climate sensitivity', *Journal of the Atmospheric Sciences* **37**, 1485–1510.

Wielicki, B. A., Wong, T., Allan, R. P., Slingo, A., Kiehl, J. T., Soden, B. J., Gordon, C. T., Miller, A. J., Yang, S.-k., Randall, D. A., Robertson, F., Susskind, J. and Jacobowitz, H. (2002), 'Energy Budget Evidence for Large Decadal Variability in the Tropical Mean Radiative Energy Budget', *Science* **295**, 841–844.

Zelinka, M. D. and Hartmann, D. L. (2010), 'Why is longwave cloud feedback positive?', *Journal of Geophysical Research* **115**(D16), D16117.

Zhao, M., Held, I. M., Lin, S.-J. and Vecchi, G. a. (2009), 'Simulations of Global Hurricane Climatology, Interannual Variability, and Response to Global Warming Using a 50-km Resolution GCM', *Journal of Climate* **22**, 6653–6678.